March 2019

Exploring Geochemical Proxies for Identifying Cryptic Sequence Boundaries in the Geologic Past Using Modern Bahamian Analogues

Evan B. Magette
Louisiana State University at Baton Rouge

EXPLORING GEOCHEMICAL PROXIES FOR IDENTIFYING CRYPTIC SEQUENCE BOUNDARIES IN THE GEOLOGIC PAST USING MODERN BAHAMIAN ANALOGUES

A Thesis

Submitted to the Graduate Faculty of the
Louisiana State University and
Agricultural and Mechanical College
In partial fulfillment of the
Requirements for the degree of
Master of Science

in

The Department of Geology and Geophysics

by
Evan Bernard Magette
B.A. Louisiana State University, 2018
May 2019

TABLE OF CONTENTS

ACKNOWLEDGEMENTS..... iv

ABSTRACT..... v

1. INTRODUCTION..... 1

2. GEOLOGIC SETTING..... 3
2.1. Eleuthera..... 3
2.2. Schooner Cays..... 4
2.3. Darby Island..... 5

3. METHODS..... 6
3.1. Sample Collection..... 6
3.2. XRD Analysis..... 7
3.3. XRF Analysis..... 7
3.4. ICP-MS Elemental Analysis of HCl Leachate..... 8
3.5. Inorganic $\delta^{13}C$ and $\delta^{18}O$..... 9
3.6. Organic $\delta^{13}C$ and $\delta^{15}N$..... 9
3.7. $\delta^{34}S$..... 9

4. RESULTS..... 11
4.1. XRD..... 11
4.2. XRF..... 13
4.3. ICP-MS Elemental Concentrations..... 14
4.4. Inorganic $\delta^{13}C$ and $\delta^{18}O$..... 20
4.5. $\delta^{34}S$ and Organic $\delta^{13}C$ and $\delta^{15}N$ 23
4.6. REY..... 25

5. DISCUSSION..... 29
5.1. Mineralogic Stabilization with Diagenesis..... 29
5.2. Inorganic $\delta^{13}C$ and $\delta^{18}O$ Variations..... 30
5.3. REY Distributions and Changes with Diagenesis..... 38
5.4. Trace element Changes with diagenesis..... 43

6. SUGGESTIONS FOR FUTURE WORK..... 49

7. CONCLUSIONS..... 51

APPENDIX A. REY DATA..... 52

APPENDIX B. ICP-MS DATA..... 54

APPENDIX C. XRF DATA……57

APPENDIX D. INORGANIC $\delta^{13}C$ AND $\delta^{18}O$ DATA……58

APPENDIX E. ORGANIC $\delta^{13}C$ AND $\delta^{15}N$ DATA……59

APPENDIX F. $\delta^{34}S$ DATA……60

REFERENCES……61

VITA……69

ACKNOWLEDGEMENTS

I would like to thank Dr. Achim Herrmann, Dr. Guangsheng Zhuang, and Dr. Yongbo Peng, who provided valued feedback during writing of this thesis document. Dr. Herrmann also assisted with collection of x-ray fluorescence data and Dr. Peng and his lab greatly assisted with collection of isotope data. I would also like to thank Wanda Leblanc who provided use of her lab for some portions of my sample preparations and aided in collection of x-ray diffraction data and production of fused beads for x-ray fluorescence.

ABSTRACT

Previous studies of carbonate diagenesis have suggested that bulk Sr concentrations and inorganic $\delta^{13}C$ values may be a useful proxy for identifying cryptic sequence boundaries in meteorically altered limestones due to geochemical processes associated with carbonate mineral stabilization in cement precipitation in the meteoric diagenetic environment. However, it is possible that natural geochemical variation in sediments may produce geochemical shift which could be misinterpreted as a cryptic sequence boundary. To test this, the Two Pines roadcut containing a previously identified protosol on Eleuthera, Bahamas, which has been affected by vadose meteoric diagenesis was sampled for bulk geochemical analysis. As well, modern sediment from around the island were collected from a variety of environments under the main assumption that these modern sediments represent the sedimentary environments which would have contributed to the formation of the limestone at the roadcut during the Pleistocene and display similar geochemical characteristics to those sediments. If the geochemical values in the meteorically altered limestone were significantly different than modern sediments, then the geochemical parameter was determined to have potential as a proxy for meteoric diagenesis. Viability of proxies for determining cryptic sequence boundaries were also determined from geochemical trends in the roadcut samples. The parameters measured included mineralogy by x-ray diffraction, inorganic $\delta^{13}C$ and $\delta^{18}O$, rare earth elements and yttrium (REY), and trace elemental analysis (Ca, Mg, Sr, S, Al, Fe, Mn, Sc, V, Cr, Co, Ni, Cu, Zn, Ba, Ti, Th, U, Cd, Rb, and Mo). $\delta^{34}S$, organic $\delta^{13}C$, and organic $\delta^{15}N$ and are reported and discussed for sediment samples only. Results show Sr does not appear to significantly record meteoric diagenesis in the roadcut samples, nor does it appear useful for identification of cryptic sequence boundaries. This follows for U concentrations as well. Inorganic $\delta^{13}C$ and $\delta^{18}O$ and mineralogy do indicate meteoric diagenesis but do not appear useful for identification of cryptic sequence boundaries. Sr, U, $\delta^{13}C$, and $\delta^{18}O$ are potentially heavily influenced by the original mineralogy. Other potential proxies which show significant differences between the meteorically altered roadcut and modern unaltered carbonate sediments include REY, Mg, S, Cr, Co, Cu, and Zn.

1. INTRODUCTION

Sequence stratigraphy over time has become a major tool in regional stratigraphic correlations, however, sequence boundaries may sometimes be difficult to decipher based only on lithologic changes in the rock record (Railsback et al., 2003; Van Wagoner et al., 1990). One potential way to combat this is to analyze the geochemical signatures of proposed sequence boundaries, in this case the subaerial exposure surfaces associated with sequence boundaries, to determine if there is a common geochemical signature imparted on the rocks after subaerial exposure from diagenetic alteration. This was done by Railsback et al. (2003, 2013) using Ordovician carbonates from the Nashville Dome, Tennessee, in which previous sequence boundaries were already defined based on facies transitions and lateral relationships (Holland and Patzkowsky, 1998). Railsback et al. (2003, 2013) specifically analyzed bulk Sr concentration, bulk $\delta^{13}C$, and bulk $\delta^{18}O$ from intervals above and below the previously identified exposure surfaces based on two assumptions: (1) Sr concentration would decrease below the proposed exposure surface due to dissolution of aragonite containing Sr; and (2) there would be a decrease in $\delta^{13}C$ values from dissolution and precipitation of isotopically light $CaCO_3$, due to enrichment of ^{12}C in exposed surfaces by photosynthetic organisms, in a zone of supersaturation below the proposed exposure surface. While $\delta^{18}O$ was measured in both studies, it should be noted that it was found to show little relationship to subaerial exposure. From their studies, they infer that bulk Sr concentration and bulk $\delta^{13}C$ can be useful to determine periods of subaerial exposure and has potential to be used to identify exposure surfaces that are not visible purely from changes in lithology.

An issue with Railsback et al. (2003, 2013) regarding the identification of cryptic sequence boundaries is that it is unclear whether the decrease in Sr concentration and $\delta^{13}C$ values are from the diagenetic alteration or rather signals that were already inherent in the sediments themselves before diagenesis occurred. Railsback et al. (2013) comments on the potential for natural geochemical variability within sedimentary horizons to produce signals similar to those seen with meteoric diagenesis and note multiple samples along one horizon are important to deduce actual geochemical shifts characteristic of a horizon. However, the question would still stand if the shifts are actually due to meteoric diagenesis in the case of cryptic sequence boundaries.

To test this idea, mineral and chemical compositions of modern carbonate sediments from Eleuthera, the Schooner Cays, and Darby Island in the Bahamas, are compared to the mineral and chemical compositions of samples collected across a well identified protosol on Eleuthera with the main assumption of this study being that the modern sediments samples in this study are analogous to the sediments that would have been deposited to form the meteorically altered limestone that is measured.

According to the conclusions of Railsback et al. (2003, 2013), a notable depletion of Sr should be detected below the sampled protosol. However, if modern carbonate sediment samples around Eleuthera display similar Sr concentrations to the supposed depleted Sr concentration below the protosol, it would imply that a similar Sr signature across the protosol could be generated by the initial chemistry of the sediments that formed the limestone and produce a signature that could be misinterpreted as meteoric diagenesis. Likewise, if the Sr concentrations from the sediment are significantly different than the supposed depleted Sr

concentrations below the protosol, then it implies that the depleted Sr concentrations characteristically be from the stabilization of aragonite during diagenesis. The use of a protosol instead of a paleosol in this study should yield results most similar to what would be seen in cryptic sequence boundaries, as protosols are exposed for less time and are less well developed than paleosols. Similar comparisons between sediment and protosol are made in this study for a host of other different elements as well. Likewise, rare earth elements and Yttrium (REY) and inorganic $\delta^{13}C$ and $\delta^{18}O$ values are compared between sediment and protosol samples and $\delta^{34}S$, organic $\delta^{13}C$, and organic $\delta^{15}N$ values are presented and discussed for sediment samples.

2. GEOLOGIC SETTING

2.1. Eleuthera

Holocene and Pleistocene sea-level fluctuations are the main influences for the construction of Eleuthera during the Quaternary (Hearty, 1998). According to Hearty, 1998, periods of growth mainly occurred when sediments which accumulated during interglacial periods were transported to the island during glacial periods and lithified. This sedimentary response to Quaternary sea-level fluctuations can be seen in the variety of carbonate deposits forming the island. These deposits include beach, tidal, and eolianites along with *in situ* reefs and well developed paleosols (Hearty, 1998; Kindler and Hearty, 1996; Neumann and Hearty, 1996). Also, with Eleuthera being exposed to the Atlantic on its Easterly side, storms and high winds transport sediments to produce washover lobes on the leeward side (Hearty, 1998). The paleosols across Eleuthera were developed during glacial low stand periods and have additions of African dust and Mississippi river valley loess to the parent soil material (Muhs et al., 2007). Unlike paleosols of Ordovician carbonates, which are described as not being well-suited for recording and retaining early diagenetic affects due to factors such as age, lower diagenetic potential, and lack of vascular plants (Railsback et al., 2003), Eleutheran carbonates are younger (Quaternary) and described as being extremely well preserved due to rapid lithification on exposure with paleosols being well developed due to high levels of vegetation being allowed to form due to reduced sediment input during glacial periods (Hearty, 1998). If the depleted Sr concentration below paleosols suggested by Railsback et al. (2003, 2013) holds true, then the depleted signature should be very well developed in the Eleutheran protosol.

The protosol sampled for this study is in the Two Pines roadcut (figures 1 and 2) and displays a light color with poor cementation. The Two pines roadcut consists of two poorly cemented Marine Isotope Stage (MIS) 5e oolitic eolianite deposits, similar to deposits of the Grotto Beach Formation described on San Salvador (Hearty and Kindler, 1993), with westward dipping cross beds separated by an approximately 0.3 m thick calcarenite protosol developed during a period of slow sedimentation (Kindler and Hearty, 1996; Neumann and Hearty, 1996) thought to be associated with a middle MIS 5e regressive phase (Hearty and Kindler, 1995; Neumann and Hearty, 1996). While the lower eolianite was deposited during the early MIS 5e high stand (Carew and Mylroie, 1995; Hearty and Kindler, 1995; Hearty and Kindler, 1993), the upper eolianite is thought to have been deposited during the late MIs 5e regressive phase after a rapid sea-level rise to approximately +6 m relative to modern sea-level (Hearty and Neumann, 2001; Neumann and Hearty, 1996; Strasser et al., 1997). The upper eolianite is also thought to have accreted rapidly due to the occurrence of in place vegetation, such as palm trunks, rooted in the protosol (Neumann and Hearty, 1996). Petrography of the two eolianites by Kindler and Hearty (1996) indicate that the older eolianite below the protosol has significantly lower bioclast content and higher ooid content than the younger eolianite above the protosol. They determined the petrography of the older eolianite to be 2.9 % bioclasts, 61.8 % ooids, 25.1 % peloids, and 10.2 % misc. The petrography of the younger eolianite was determined to be 26.6 % bioclasts, 38.0 % ooids, 28.3 % peloids, and 7.2 % misc. Rhizomorphs were found in the eolianite deposits as well as in the protosol. Land snail fossils and crab claws were also noted to have been found in the protosol (Hearty, 1998; Swart, 2017).

2.2. Schooner Cays

The Schooner Cays is a 16 km x 60 km ooid shoal complex located off the coast of Cape Eleuthera. Extensive information about the morphology and hydrology of the Schooner Cays is

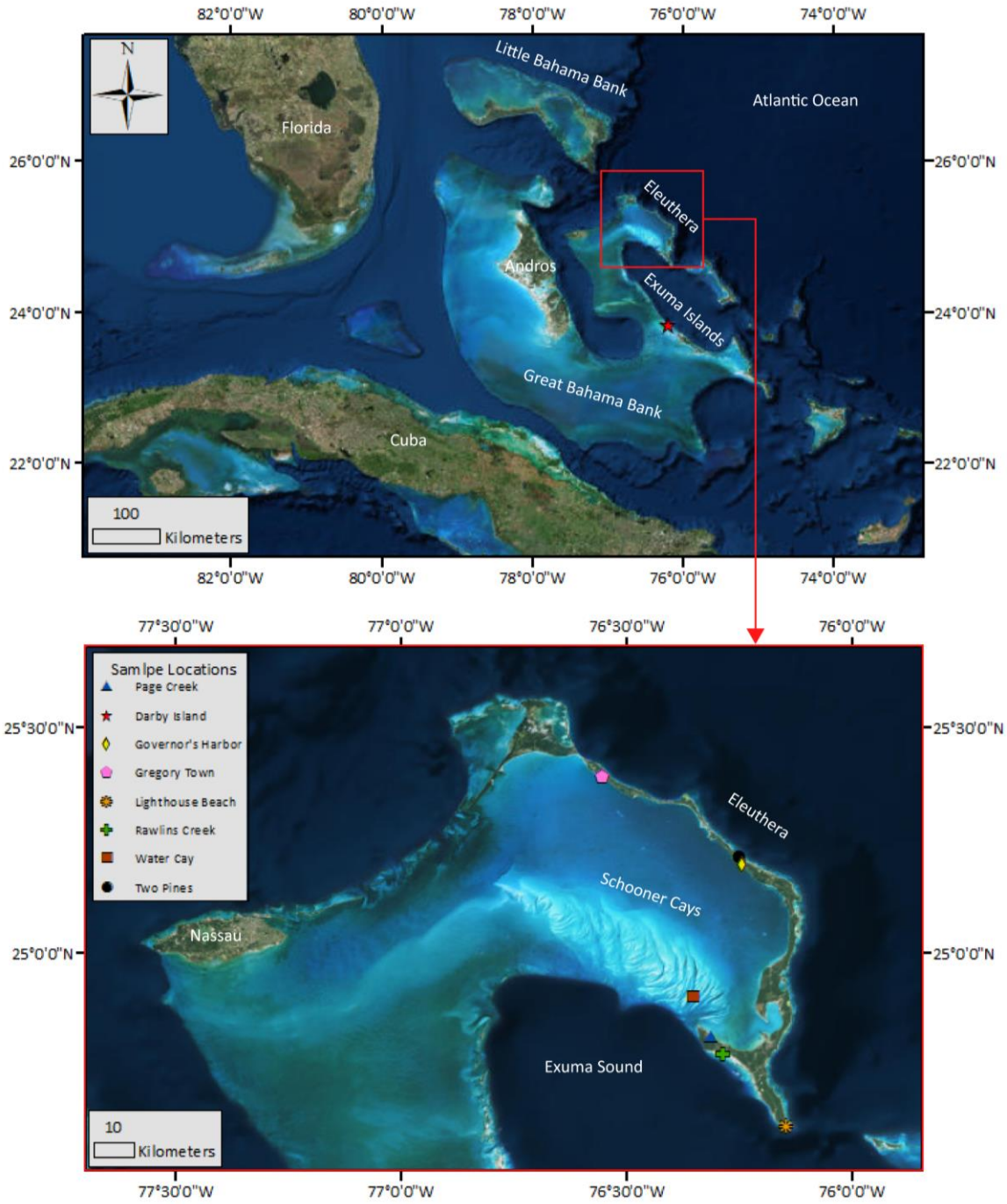

Figure 1. Map of sampling locations on Eleuthera, Bahamas.

lacking, however, Ranker and Reeder (2011) provide a detailed description of the Schooner Cays and is summarized here. The morphology of the ooid shoal complex is mainly influenced

by tidal cycles with flood tides coming in from and ebb tides going out to the Exuma Sound to the south-west. General morphologic features of the Schooner Cays include Symmetric and asymmetric sand ridges, parabolic bars, and flow-oblique shoulder bars along with tidal channels. With the tidal flows being focused though channels in the complex, the flow radiates and loses energy as it migrates across the platform. The initial high energy currents near the margin produce a rocky bottom due to removal of sediments by the current. The loss of energy further inwards allows for deposition of sediments with finer grain sizes towards the interior of the platform. The change in current velocity is also associated with a shift from flow-parallel tidal sand ridges near the platform margin to parabolic bars and lower wave heights further inwards. The inward platform ends of these bars and ridges curve North West, likely due to the increased effect of wind driven currents with the decrease in tide driven current strength. Within the Schooner Cays there are six small vegetated cays, four of which are located approximately 6.5 km to 9.5 km off the northern point of Cape Eleuthera. Of these four, the eastern most cay, Water Cay, is where the Schooner Cays samples for this study were collected. It is located approximately 6.5 km north of Cape Eleuthera with coordinates of 24°54’16.1’’N, 76°21’12.5’’W. Water Cay is roughly 100 m x 200 m to 150 m x 200m, displaying a rough circular shape. The rim of the island is composed of ooid sand with crusts of oolitic limestone, most likely derived from the local ooid sand. The interior of the island is covered by moderate to thick vegetation. Likewise, Corals, along with other carbonate producing taxa, can be found in various locations near the shore line.

2.3. Darby Island

Darby Island is a vegetated cay, similar to Water Cay, located in the island chain known as the Exuma Cays. This island chain is located along the south western margin of the Exuma Sound (figure 1). The main purpose of the sediments from this island were to provide comparison between Eleutheran sediments and an outside sediment source from the Bahamas.

3. METHODS

3.1. Sample Collection

3.1.1. Sediment Samples

Carbonate sediment samples were collected from five locations around Eleuthera, Water Cay in the Schooner Cays, and from Darby Island in the Exuma Cays. The five sampling locations on Eleuthera are Gregory Town, Governors Harbor, Page Creek, Rawlins Creek, and Lighthouse Beach. Gregory Town, Governor's Harbor, and Lighthouse Beach are high energy nearshore beach sand samples. Page Creek and Rawlins Creek are from tide dominated areas in southern Eleuthera containing tidal channels lead way to calm shallow water environments dominated by mangrove vegetation. Sediments at slight depth below the sediment water interface at Page Creek and Rawlins Creek display a dark gray color and produce a strong foul odor indicating a low oxygen environment. Samples were collected by hand sampling at slight depth (approximately 0.1 m or less) with 50 ml centrifuge tubes. Centrifuge tubes were capped and stored for later analysis.

In total, eight samples were collected from Page Creek: Page Creek Fine Mud 1 (PCFM1), Page Creek Mud 2 (PCM2), Page Creek Fine Mud 3 1/2 (PCFM 3 1/2), Page Creek Fine Mud 3 2/2 (PCFM 3 2/2), Page Creek Mud 3 Anoxic (PCM3A), Page Creek Mud 3 (PCM3), Page Creek Mud 4 (PCM4), and Page Creek Black Mud (PCBM). Two samples were collected from Rawlins Creek: Rawlins Creek (RC) and Lower Creek (LC; oolitic tidal channel sample). Three samples were collected from Darby Island: BO1, BD, and PB. One sample each was collected from Gregory Town, Governor's Harbor, and Lighthouse Beach and are labeled GT, GH, and EL respectively. Two samples were collected from Water Cay in the Schooner Cays. One sample was collected near the coastline (Schooner Cays Near Shore; SCNS) and the other (Schooner Cays Off Shore; SCOS) was collected further off shore, but within approximately 50 m of the coastline of Water Cay. Sediments from the Schooner Cays were also hand-picked under a microscope in order to produce pure ooid and non-ooid samples labeled SCPO and SCNO respectively.

3.1.2. Protosol Samples

Samples from the Two pines (TP) roadcut were sampled at 0.1 m intervals. Five samples were collected from below the protosol, three samples were collected within the protosol, and five additional samples were collected above the protosol. Sample names for the roadcut samples are named in the order in which they were taken. For example, TP1 was the first samples taken at 0.9 m above ground level and TP2 was taken at 1 m above ground level. This continues to TP13 which was taken at a position of 2.1 m above ground level. Samples TP6 through TP8 were taken within the protosol.

3.2. XRD Analysis

XRD analysis was completed on TP and modern sediment samples collected from the locations mentioned above. Samples were micronized in ethanol, to ensure uniform grain sizes and mineral distribution during analysis, and then pressed into beads. Measurements were collected on a PANalytical Empyrean X-ray diffractometer using Cu Kα1 radiation. Intensity factors for determining mineral percentages were calculated using a 50:50 with quartz. Using HighScore XRD spectrum analysis software, minerals components were determined by an analyst at Louisiana State University. The Rietveld method, which utilizes the entire XRD spectrum in calculating mineral abundances (Rietveld, 1969), was used by the software to calculate mineral abundances as other methods only utilize the 100 % peaks. A secondary quartz standard was used to ensure machine accuracy.

Figure 2. A) Close view of the Two Pines Protosol. Small increments on the left half of the scale are 0.01 m. B) Two Pines section showing the protosol and two Pleistocene eolianites. C) Page Creek sampling site. D) Rawlins Creek tidal channel sampling site.

3.3. XRF Analysis

XRF analysis was completed on the previously mentioned seventeen samples, as well as on the thirteen samples collected from the Two Pines roadcut. Elemental concentrations of

CaO, MgO, S, and Sr were measured for each sample. Samples were powdered to a uniform size and subjected to high temperatures (approximately 1100 °C) to form fused beads. From this process, a significant portion of carbon and oxygen from the carbonates are lost in the form of CO_2 gas. Calibration curves were constructed by running standards, plotting counts versus concentration, and preforming a linear regression. Standard NISTSRM1d, an argillaceous limestone powder standard, was run as a secondary standard during each run (three total runs) to ensure machine accuracy. Oxides are reported in percent and non-oxides are reported in ppm.

3.4. ICP-MS elemental analysis of HCl leachate

Elemental concentrations of various elements in the Two Pine and sediment samples were measured using solution ICP-MS. Samples for the ICP-MS were prepared by first dissolving ~1 g of each sample in 1 N HCl. The organic material was then removed by filtering the HCl leachate through Whatman GF/C glass microfiber filters (pore size = 1.2 µm). For each sample, 0.05 ml HCl leachate was pipetted into a separate vail and diluted with 9.95 ml of 2% HNO_3. Analysis was run on the diluted HCl leachates.

REY were normalized to the Post Archean Australian Shale (PAAS; Pourmand et al., 2012). Total REY, REY anomalies (written as $[REY]_{SN}/[REY]_{SN}^*$), Y/Ho ratio, and HREE enrichment were calculated using the formulas below. Subscript SN indicates shale normalized values were used. REY anomaly formulas of Lawrence et al. (2006) were used for elements La, Ce, Eu, Gd, and Lu. The anomaly formula for Pr is from Alibo and Nozaki (1999). Anomalies for the remaining elements were calculated using formula (8) after Alibo and Nozaki (1999).

$$\text{Total REY} = \sum [REY] \quad (1)$$

$$La_{SN}/La^*_{SN} = \frac{[La]_{SN}}{[Pr]^3_{SN}/[Nd]^2_{SN}} \quad (2)$$

$$Ce_{SN}/Ce^*_{SN} = \frac{[Ce]_{SN}}{[Pr]^2_{SN}/[Nd]_{SN}} \quad (3)$$

$$Eu_{SN}/Eu^*_{SN} = \frac{[Eu]_{SN}}{([Sm]^2_{SN} * [Tb]_{SN})^{1/3}} \quad (4)$$

$$Gd_{SN}/Gd^*_{SN} = \frac{[Gd]_{SN}}{([Tb]^2_{SN} * [Sm]_{SN})^{1/3}} \quad (5)$$

$$Lu_{SN}/Lu^*_{SN} = \frac{[Lu]_{SN}}{[Yb]^2_{SN}/[Tm]_{SN}} \quad (6)$$

$$Pr_{SN}/Pr^*_{SN} = \frac{2[Pr]_{SN}}{(3[Nd]_{SN} - [Sm]_{SN})} \quad (7)$$

$$[REY]_{SN}/[REY]^*_{SN} = \frac{2[REY]_{SN_n}}{([REY]_{SN_{n-1}} + [REY]_{SN_{n+1}})} \quad (8)$$

$$Y/Ho = {}^{[Y]}\!/_{[Ho]} \quad (9)$$

$$\text{HREE enrichment} = [Yb]_{SN}/[Nd]_{SN} \quad (10)$$

Sediment samples were assigned into two group (SED-G1 and SED-G2) based on differing REY distributions which are discussed in later sections.

3.5. Inorganic $\delta^{13}C$ and $\delta^{18}O$

Analysis of inorganic $\delta^{13}C$ and $\delta^{18}O$ was performed on 200 ± 20 µg of micronized material for each sample at the Oxy-Anion Stable Isotope Consortium (OASIC) at Louisiana State University. Micronized samples were heated in a 75 ^{o}C oven for 12 hours after being loaded in 12 ml borosilicate glass Exetainer vials (Labco Ltd., Lampeter, UK). The vails were then sealed and the atmosphere in the vials was replaced by He by flushing them with 99.999% He for 2 minutes with a flow rate of 80 ml/minute. After flushing, sample vials were loaded into a 96-position Thermo Finigan Gas Bench II kept at 72 ^{o}C. Samples were then reacted for 3 hours with 100 µL phosphoric acid (density = 1.92 g/mL) kept at 75 ^{o}C and added by manual injection. After 3 hours, CO_2 produced from the reaction was passed through a Nafion water trap and GC in Gas Bench. Analysis was done on a Delta V Advantage mass spectrometer. Two working standards, having $\delta^{13}C$ and $\delta^{18}O$ are 2.57 ‰ and -4.31 ‰ respectively (VPDB), were marble calibrated by NBS-19 and LSVEC and were run every 10 samples. For $\delta^{13}C$, the external precision (1σ) is better than 0.04 % for sample sizes >200 µg. For $\delta^{18}O$, the external precision (1σ) is better than 0.1 % for sample sizes >200 µg.

3.6. Organic $\delta^{13}C$ and $\delta^{15}N$

Analysis of organic $\delta^{13}C$ and $\delta^{15}N$ was performed on residual organic material from dissolved carbonate samples. Organic material was acquired by dissolving samples in 1 N HCl to remove the $CaCO_3$ material. The residual organic material was centrifuged down and the HCl leachate was decanted. The organic material was then washed three times with Milli-Q water (18.2 MΩ) to remove any residual HCl leachate. The organic material was then dried overnight and weighed in tin capsules for analysis.

CO_2 and N_2 gas produced from the samples by flash combusting the tin capsules at 950 ^{o} C in a furnace with an elemental analyzer (Micro Vario Cube, Isoprime Ltd., Cheadle, Uk) was analyzed by continuous flow with an Isoprime100 (Isoprime 100, Cheadle, UK) gas source mass spectrometer.

Data are reported relative to the VPDB and AIR standard for organic carbon and nitrogen respectively. One working standard, acetanilide ($\delta^{13}C$ = -27.6 ‰ and $\delta^{15}N$ = 1.61 ‰), was used for calibration with samples having a repeatable value to a standard error of 0.1 ‰and 0.32 ‰ for $\delta^{13}C$ and $\delta^{15}N$ respectively.

3.7. $\delta^{34}S$

Analysis of $\delta^{34}S$ was completed on residual material gathered and prepared in the same manner as organic $\delta^{13}C$ and $\delta^{15}N$ samples, up to and including weighing the samples in tin capsules, at OASIC at Louisiana State University. As pyrite is not completely soluble in HCl (Rickard and Morse, 2005), $\delta^{34}S$ will mainly be a net result of sulfide and organic S fractionation. After weighing in tin capsules, SO_2 gas was produced by flash-combusting samples at 1150 ^{o}C in

a furnace using an elemental analyzer (Micro Vario Cube, Isoprime Ltd., Cheadle, UK) and analyzed by continuous flow in an Isoprime100 (Isoprime 100, Cheadle, Uk) gas source mass spectrometer. Data are reported relative to the VCDT standard with a precision better than ± 0.3 ‰.

4. RESULTS

4.1. XRD

The primary minerals found throughout the sediment samples are calcite, aragonite, and high-magnesium calcite. The mineral abundances vary between and within sampling locations. Other minerals seen in the samples include ankerite, pyrite, gypsum, quartz, dolomite, and halite. The occurrence of halite in samples is assumed to be remnant not completely removed by the washing of samples before powdering

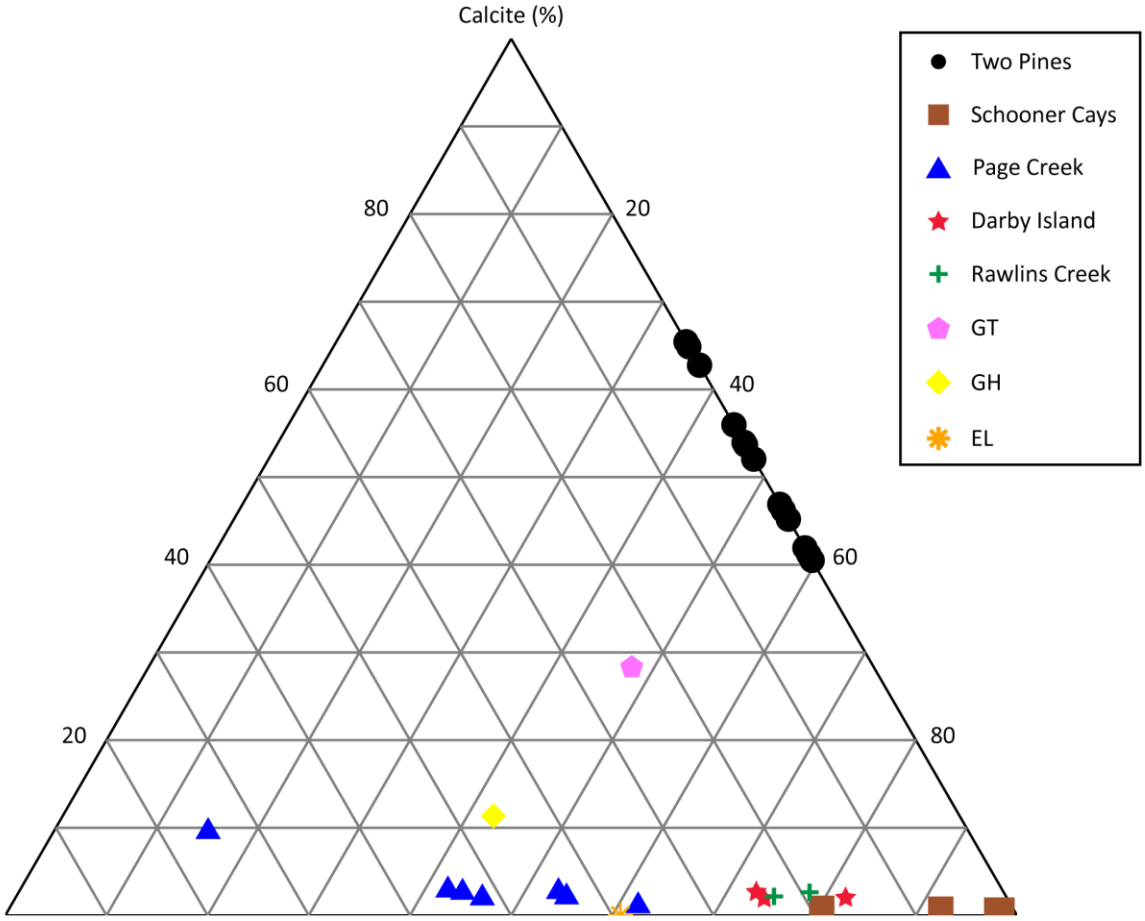

Figure 3. XRD ternary diagram for calcite, high-magnesium calcite, and aragonite for Two Pines and sediment samples from Eleuthera.

The ternary diagram (figure 3) shows the abundance changes between calcite, magnesian calcite, and aragonite between the different sampling locations. Samples from the Two Pines roadcut have an absence of magnesian calcite with calcite and aragonite concentrations varying between approximately 35 % to 60 %. Calcite concentrations from the Two Pines roadcut are the greatest out of all samples. All other samples, except for GT with 28.7 % calcite, have low (< 12 %) amounts of calcite with variable amounts of magnesian calcite

Table 1. XRD data from the Two Pines roadcut and modern sediment samples.

Sample Name	Calcite (%)	Mg Calcite (%)	Aragonite (%)	Dolomite (%)	Ankerite (%)	Pyrite (%)	Quartz (%)	Gypsum (%)	Halite (%)
TP 13	61.9	0	32.7	0	0	0	0	0	5.4
TP 12	64.1	0	34.7	0	0	0	0	0	1.2
TP 11	59.5	0	35.3	0	0	0	0	0	5.2
TP 10	54	0	42.5	0	0	0	0.1	0	3.4
TP 9	48.3	0	44.5	0	0	0	0	0	7.2
TP 8	40.5	0	57.9	0	0	0	0	0	1.6
TP 7	40.5	0	59.5	0	0	0	0	0	0
TP 6	41.8	0	57.9	0	0	0	0	0	0.3
TP 5	53.3	0	46	0	0	0	0	0	0.8
TP 4	53.8	0	45.9	0	0	0	0	0	0.3
TP 3	45.2	0	54.8	0	0	0	0	0	0
TP 2	46.2	0	53.8	0	0	0	0	0	0
TP 1	46.8	0	53	0	0	0	0.1	0	0.1
SCNS	0.6	1.7	97.3	0	0	0	0	0	0.5
SCOS	0.7	7.2	92.2	0	0	0	0	0	0
SCPO	0.6	1.2	98.2	0	0	0	0	0	0
SCNO	0.8	18.9	80.3	0	0	0	0	0	0
BO1	2.2	24.3	73.5	0	0	0	0	0	0
EL	0	39.2	60.8	0	0	0	0	0	0
BD	1.3	17	81.8	0	0	0	0	0	0
PB	1.6	23.6	74.7	0	0	0	0	0	0
GT	28.7	23.2	48	0	0	0	0	0	0
GH	11.3	45.9	42.4	0	0.4	0	0	0	0
RC	1.5	22.6	75.9	0	0	0	0	0	0
LC	2	19.3	78.7	0	0	0	0	0	0
PCFM 1	8.4	63.2	12.7	0	11.5	0.3	0.5	1	2.4
PCFM 3 1/2	3.1	43.5	52.8	0.6	0	0	0	0	0
PCFM 3 2/2	2.5	43.1	54	0	0.5	0	0	0	0
PCM3A	3.3	54.6	42.1	0	0	0	0	0	0
PCM3	3	52.7	43.2	0	0	0	0	0	1.1
PCM4	2.4	51.6	45.9	0	0	0	0	0	0.2
PCBM	1.5	36.7	61.8	0	0	0	0	0	0

and aragonite. Samples from the Schooner Cays show low concentrations of calcite and magnesian calcite with high amounts of aragonite. All Schooner cays samples have > 95 % aragonite except for the non-ooid fraction of sediments (SCNO) which has a higher amount of magnesian calcite (table 1). Samples from Rawlins Creek and Darby Island are similar having low

amounts of calcite with aragonite ranging between 73.5 % and 81.8 %. Most samples form Page Creek have low amounts of calcite and similar concentrations of magnesian calcite and aragonite. The exception to this is PCFM1 which has slightly higher amounts of calcite and a majority of magnesian calcite. Samples GT, GH, and EL are grouped together based on similar high energy beach localities. These samples have roughly similar magnesian calcite and aragonite concentrations but vary in their calcite concentrations. EL has the lowest amount of calcite (0.0 %), GH has the second highest (11.3 %) and GT has the highest (28.7 %) out of the three. Table 1 shows information on the amounts of the remaining mineral phases. While many of these show 0 %, this does not mean they do not exist in the sample, but rather may have been too low in amount to be detected by XRD.

4.2. XRF

XRF data is reported for major carbonate elements: CaO, MgO, Sr, and S (figure 4). Elemental concentrations of standard NISTSRM1d were measured during each run of the XRF machine. Standard elemental concentrations had the following values, where % represents percent deviation from average: (1) CaO, 51.51 ± 0.36 %; (2) MgO, 1.50 ± 0.10 %; (3) S, 1106.45 ± 1.21 ppm; and (4) Sr, 224.1 ± 2.65 ppm. Percent errors when compared to accepted NISTSRM1d values are the following: (1) CaO, 2.54 %; (2) MgO, 4.30 %; (3) S, 7.63 %; and (4) Sr, 17.90 %.

Sr (ppm) in the TP samples range from 3705.08 ppm to 6148.73 ppm (average = 4945.78 ± 828.84 ppm, 1σ). Concentrations show an increasing trend from 2.1 m down into the protosol, decrease below the protosol, and then experience a slight increase then continual decrease. The peak concentration of 6148.73 ppm occurs near the center of the protosol. When compared to sediment samples, TP Sr concentrations are lower than Schooner Cays samples (~ 7000 ppm) and all samples, excluding PCFM1, PCM3A, PCBM, GH, SCOS, SCNS, and BD, have Sr concentrations which fall within the range of Sr concentrations given by TP samples. These sediment samples display a variety of concentrations which range between 3709.50 ppm and 6061.06 ppm (average = 4813.60 ± 983.93 ppm, 1σ).

S (ppm) concentrations in the TP samples range from 564.12 ppm to 1235.89 ppm (average = 718.90 ± 179.09 ppm, 1σ) and display a decreasing trend from 2.1 m to 0.9 m. When compared to sediment samples, S concentrations in the TP samples are all lower than concentrations in the sediment samples and are most similar to all sediment samples excluding those from Page Creek. These samples have S concentrations ranging from 1610.79 ppm to 2104.80 ppm (average = 1730.02 ± 147.05 ppm, 1σ).

MgO (%) concentrations in the TP samples are fairly stable and range from 1.34 % to 1.65 % (average = 1.48 ± 0.08 %, 1σ). These concentrations are lower than all sediment samples except for those from the Schooner cays which have concentrations of 1.46 % and 1.65 % for SCNS and SCOS respectively (average = 1.56 ± 0.13 %, 1σ).

CaO (%) concentrations in the TP samples range from 48.21 % to 53.19 % (average = 51.00 ± 1.51 %, 1σ). Concentrations show a low point just above the protosol at 1.7 m with concentrations increasing within the protosol and remaining fairly stable until the decrease at 0.9 m. When comparing the TP samples to sediment samples, most CaO concentrations in the TP samples are less than the Schooner Cays samples which have values of 52.3 % and 52.53 %

for SCNS and SCOS respectively. All sediment samples, excluding PCFM1, PCFM 3 1/2, PCM3A, and PCM3, have CaO concentrations which fall within the range of CaO concentrations given by TP samples. These sediment samples have CaO concentrations ranging from 48.46 % to 52.53 % (average = 50.82 ± 1.32 %, 1σ).

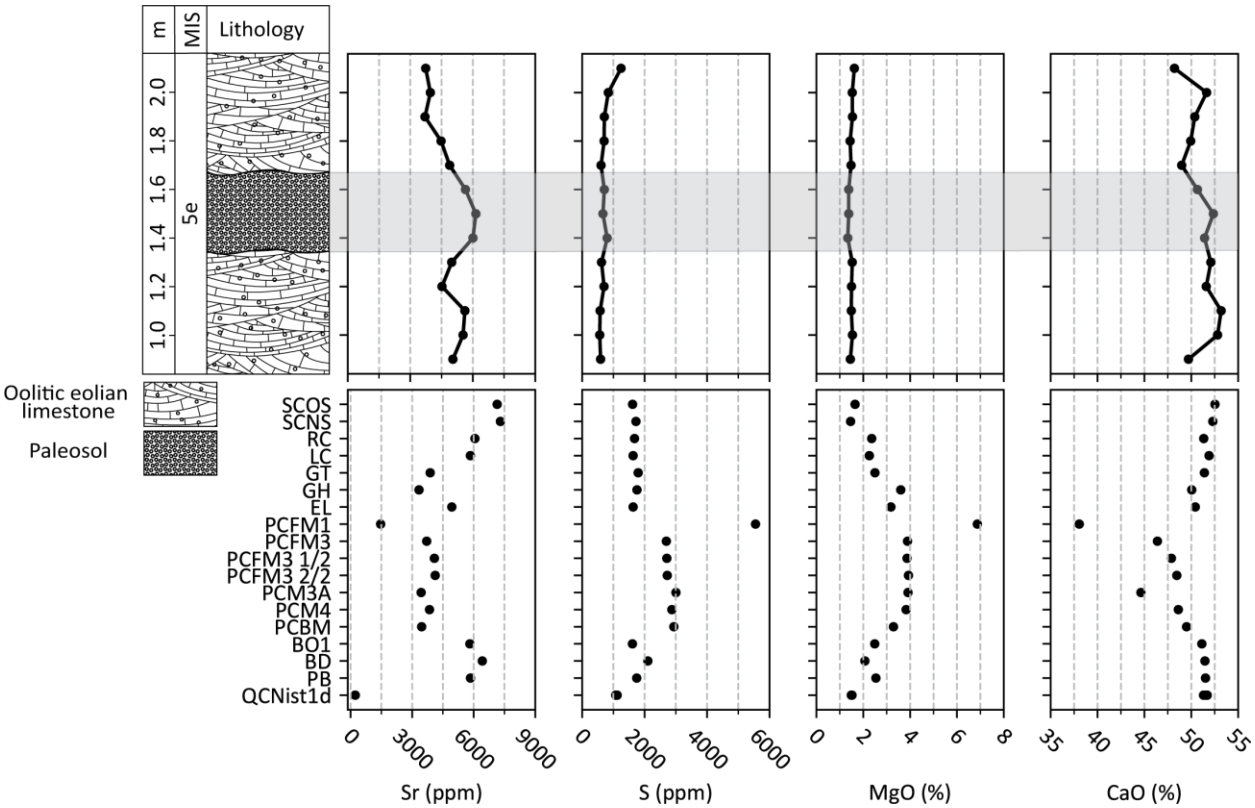

Figure 4. XRF data for the Two Pines roadcut (top) and modern sediment samples (bottom). Stratigraphic column is for the Two Pines roadcut. The abbreviation "m" indicates meters above ground level at the roadcut and "MIS" indicates marine isotope stage. The light grey bar in the upper four graphs indicates the extent of the protosol in the Two Pines roadcut. QCNist1d is a standard and has three measurements plotted for each element above.

4.3. ICP-MS Elemental Concentrations

Al (ppm) (figure 5) concentrations in the TP samples display variable concentrations ranging from 44.08 ppm to 335.35 ppm (average = 141.75 ± 89.33 ppm) with peaks at 1.9 m and 1.2 m. All sediment samples, excluding those from Page Creek and GH, have Al concentrations which fall within the range given by TP samples. These sediment samples have Al concentrations ranging from 78.31 ppm to 309.98 ppm (average = 142.81 ± 79.48 ppm, 1σ).

Fe (ppm) (figure 5) concentrations in the TP samples are fairly stable with a peak at 1.2 m and values ranging from 87.71 ppm to 144.35 ppm (average = 120.12 ± 24.92 ppm, 1σ). Sediment samples SCOS, SCNS, EL, BO1, BD, and PB have Fe concentrations which fall within the range given by TP samples. These sediment samples have Fe concentrations ranging from 88.17 ppm to 132.11 ppm (average = 102.53 ± 14.50 ppm, 1σ).

Mn (ppm) (figure 5) concentrations in the TP samples range from 0.26 ppm to 3.98 ppm (average = 1.39 ± 1.16 ppm). Mn concentrations are low above the protosol, increase and peak

inside the protosol, then decrease below the protosol. Sediment samples SCOS, SCNS, LC, BO1, BD, and PB have Mn concentrations which fall within the range given by TP samples. These sediment samples have Mn concentrations ranging from 0.41 ppm to 3.06 ppm (average = 1.87 ± 1.17 ppm, 1σ).

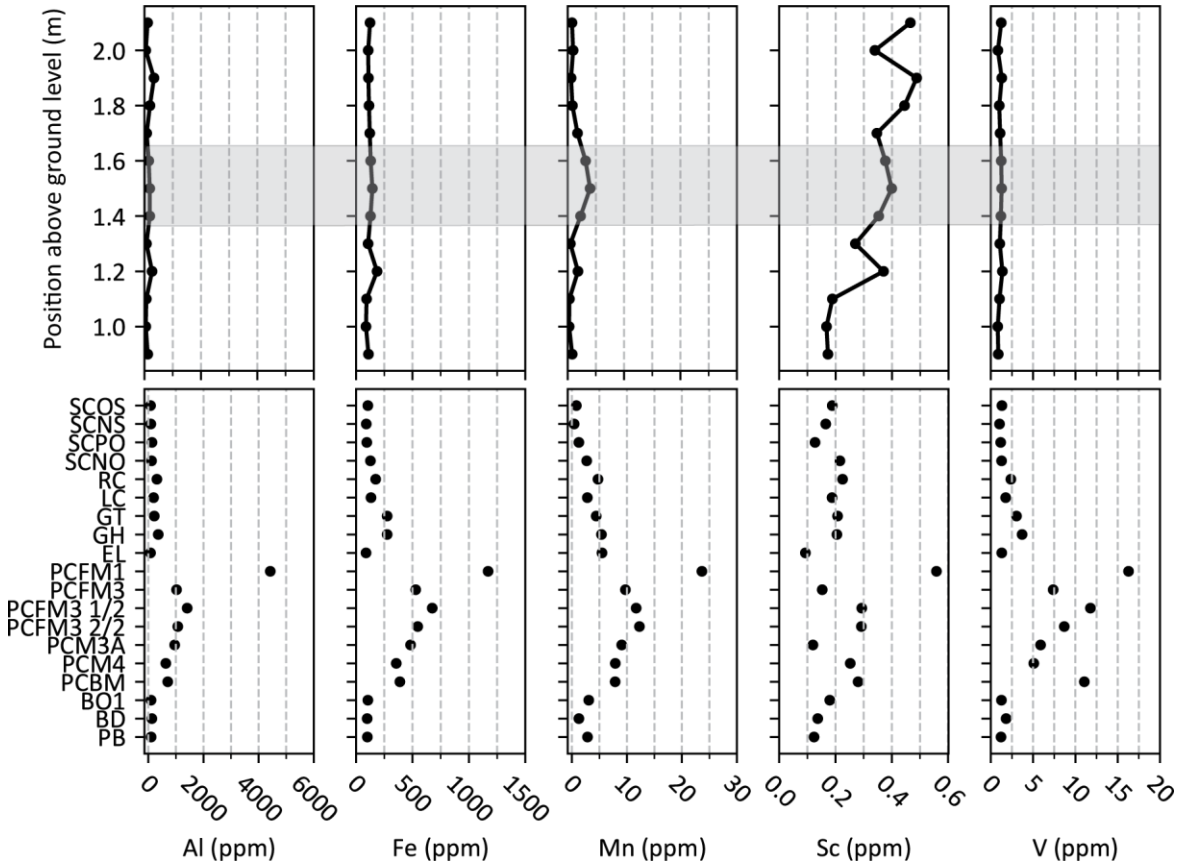

Figure 5. IPC-MS data for the Two Pines roadcut (top) and modern sediment samples (bottom). The light grey bar in the upper five graphs indicates the extent of the protosol in the Two Pines roadcut. Refer to figure 4. for the stratigraphic column.

Sc (ppm) (figure 5) concentrations in the TP samples range from 0.17 ppm to 0.49 ppm (average = 0.33 ± 0.11 ppm, 1σ) and display a general decreasing trend from 2.1 m to 0.9 m. Sediment samples, excluding PCFM1 due to its much greater Sc concentration to the remaining sediment and TP samples, range from 0.09 ppm to 0.29 ppm (average = 0.19 ± 0.06 ppm, 1σ). TP Sc concentrations, excluding samples TP1, TP2, TP3, and TP5, fall outside of this range with values ranging from 0.34 ppm to 0.49 ppm (average = 0.40 ± 0.05 ppm, 1σ). Samples TP1, TP2, TP3, and TP5 range from 0.17 ppm to 0.27 ppm (average = 0.20 ± 0.05 ppm, 1σ). Sediment samples SCOS, SCNS, RC, LC, GT, GH, PCM4, and BO1 have Sc concentrations which fall within the range of concentrations formed by samples TP1, TP2, TP3, and TP5. These sediment samples have Sc concentrations ranging from 0.17 ppm to 0.25 ppm (average = 0.20 ± 0.03 ppm, 1σ).

V (ppm) (figure 5) concentrations in the TP samples are fairly stable and range from 0.84 ppm to 1.37 ppm (average = 1.11 ± 0.18 ppm, 1σ). Sediment samples SCOS, SCNS, EL, BO1, and

PB have V concentrations which fall within the range given by TP samples. These sediment samples have V concentrations ranging from 1.04 ppm to 1.32 ppm (average = 1.22 ± 0.11 ppm, 1σ).

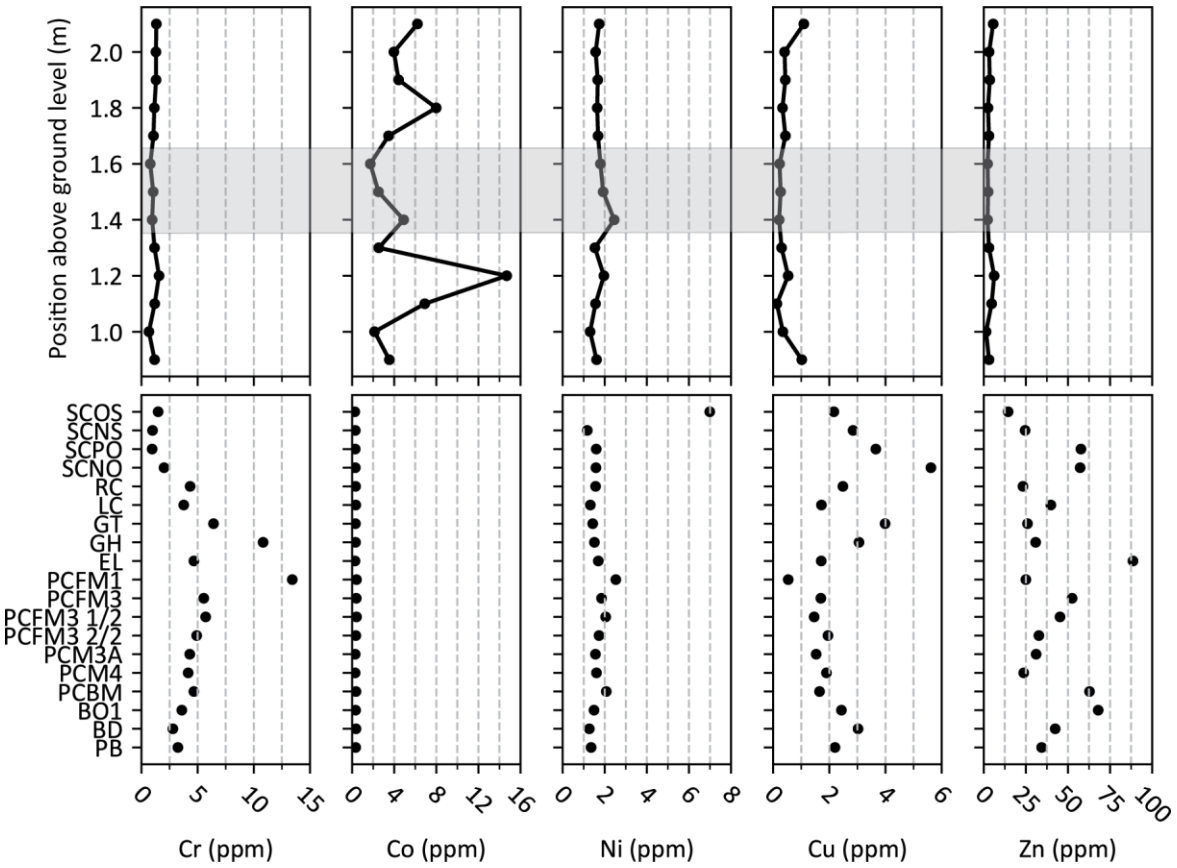

Figure 6. IPC-MS data for the Two Pines roadcut (top) and modern sediment samples (bottom). The light grey bar in the upper five graphs indicates the extent of the protosol in the Two Pines roadcut. Refer to figure 4. for the stratigraphic column.

Cr (ppm) (figure 6) concentrations in the TP samples are fairly stable and range from 0.66 ppm to 1.32 ppm (average = 1.12 ± 0.24 ppm, 1σ). TP Cr concentrations are lower than all sediment samples excluding SCNS with a concentration of 0.98 ppm. The next highest concentration in the sediments is SCOS at 1.48 ppm followed by BD at 2.79 ppm. SCNS and SCOS have an average Cr concentration of 1.23 ± 0.35 ppm (1σ).

Co (ppm) (figure 6) concentrations in the TP samples vary heavily with a range of values from 1.73 ppm to 14.69 ppm (average = 5.00 ± 3.48 ppm, 1σ). Sediment Co concentrations are similar between samples and are ubiquitously lower than TP Co concentrations with values ranging from 0.26 ppm to 0.42 ppm (average = 0.34 ± 0.05 ppm, 1σ).

Ni (ppm) (figure 6) concentrations in the TP samples range from 1.30 ppm to 2.45 ppm (average = 1.72 ± 0.28 ppm, 1σ). Concentrations in the TP samples show a gradual increase from 2.1 m to a peak at 1.4 m and then a general decrease in values to 0.9 m. All sediment samples, excluding SCOS, SCNS, PCFM1, and BD, have Ni concentrations which fall within the

range of concentrations given by TP samples. These sediment samples range from 1.31 ppm to 2.07 ppm (average = 1.63 ± 0.24 ppm, 1σ).

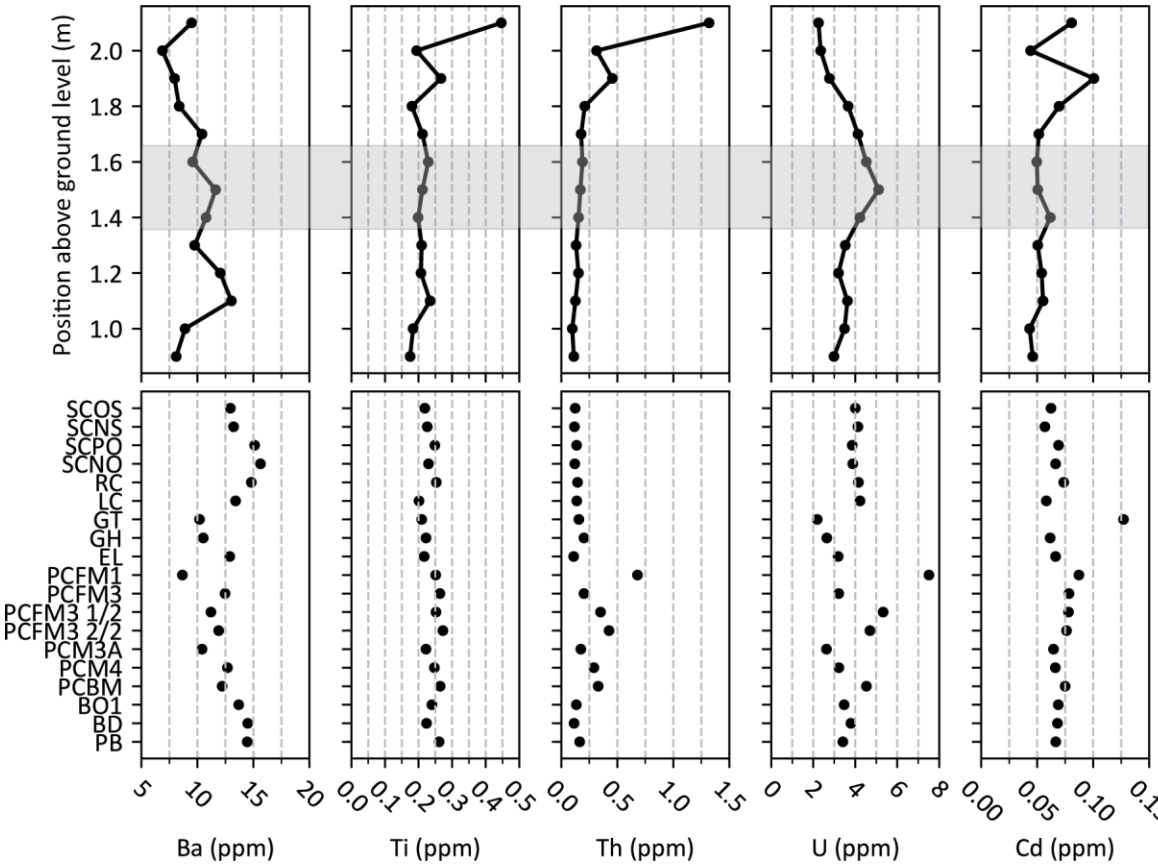

Figure 7. IPC-MS data for the Two Pines roadcut (top) and modern sediment samples (bottom). The light grey bar in the upper five graphs indicates the extent of the protosol in the Two Pines roadcut. Refer to figure 4 for the stratigraphic column.

Cu (ppm) (figure 6) concentration in the TP samples range from 0.13 ppm to 1.09 ppm (average = 0.44 ± 0.29 ppm, 1σ) and are fairly stable between 2.0 m to 1.0 m. All sediment samples, excluding PCFM1 with a Cu concentration of 0.54 ppm, have Cu concentrations higher than what is measured in the TP samples. These samples range from 1.46 ppm to 3.99 ppm (average = 2.24 ± 0.70 ppm, 1σ).

Zn (ppm) (figure 6) concentrations in the TP samples range from 1.39 ppm to 6.19 ppm (average = 3.37 ± 1.37 ppm, 1σ). Zn concentrations in the TP samples are ubiquitously lower than Zn concentrations in all sediment samples, with the most similar concentration being SCOS at 14.48 ppm. Zn concentrations in the sediment samples range from 14.18 ppm to 88.60 ppm (average = 39.15 ± 19.27 ppm, 1σ).

Cd (ppm) (figure 7) concentrations in the TP samples range from 0.04 ppm to 0.10 ppm (average = 0.06 ± 0.02 ppm, 1σ). Cd concentrations in the TP samples vary heavily from 2.1 m to 1.8 m and then are fairly stable from 1.7 m to 0.9 m. All sediment samples, excluding GT, have Cd concentrations which fall within the range of Cd concentrations given by TP samples. These

sediment samples have Cd concentrations ranging from 0.06 ppm to 0.09 ppm (average = 0.07 ± 0.01 ppm, 1σ).

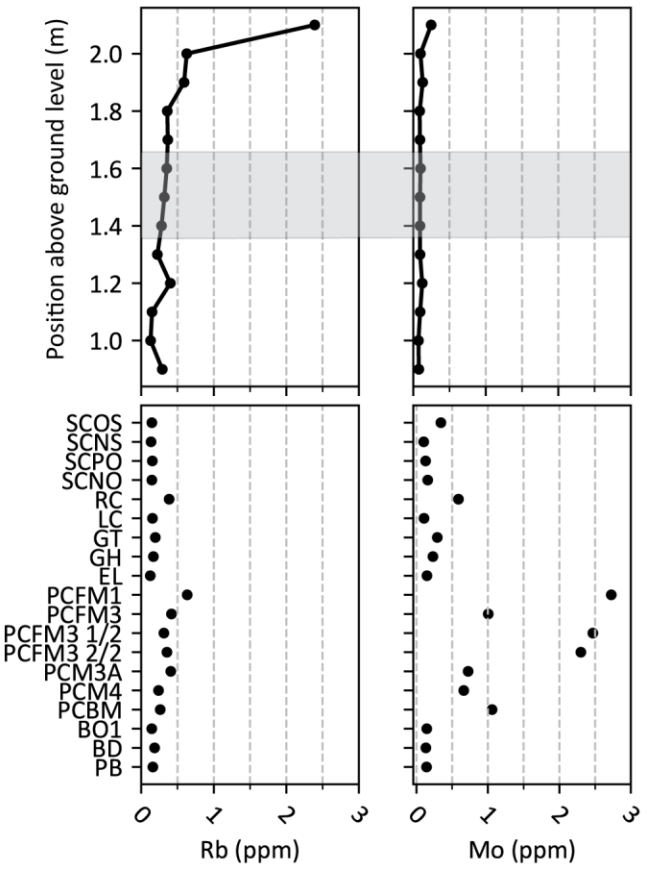

Figure 8. IPC-MS data for the Two Pines roadcut (top) and modern sediment samples (bottom). The light grey bar in the upper two graphs indicates the extent of the protosol in the Two Pines roadcut. Refer to figure 4 for the stratigraphic column.

Ba (ppm) (figure 7) concentrations in the TP samples range from 6.88 ppm to 13.03 ppm (average = 9.76 ± 1.78 ppm, 1σ). TP samples show a general increase in Ba concentrations form 2.0 m to 1.5 m followed by a decrease in concentration to 0.9 m with a peak at 1.1 m. All sediment samples, excluding SCNS, RC, LC, BO1, BD, and PB, have Ba concentrations which fall within the range of concentrations given by TP samples. These sediment samples have Ba concentrations ranging from 8.66 ppm to 12.94 ppm (average = 11.46 ± 1.38 ppm, 1σ).

Ti (ppm) (figure 7) concentrations in the TP samples range from 0.45 ppm to 0.17 ppm (average = 0.23 ± 0.07 ppm, 1σ). TP samples show a sharp decrease in Ti concentrations from 2.1 to 2.0 m and fairly stable concentrations from 1.8 m to 0.9 m. All sediment samples have Ti concentrations which fall within the range of values given by TP samples. These sediment samples have Ti concentrations ranging from 0.2 ppm to 0.27 ppm (average = 0.24 ± 0.02 ppm, 1σ).

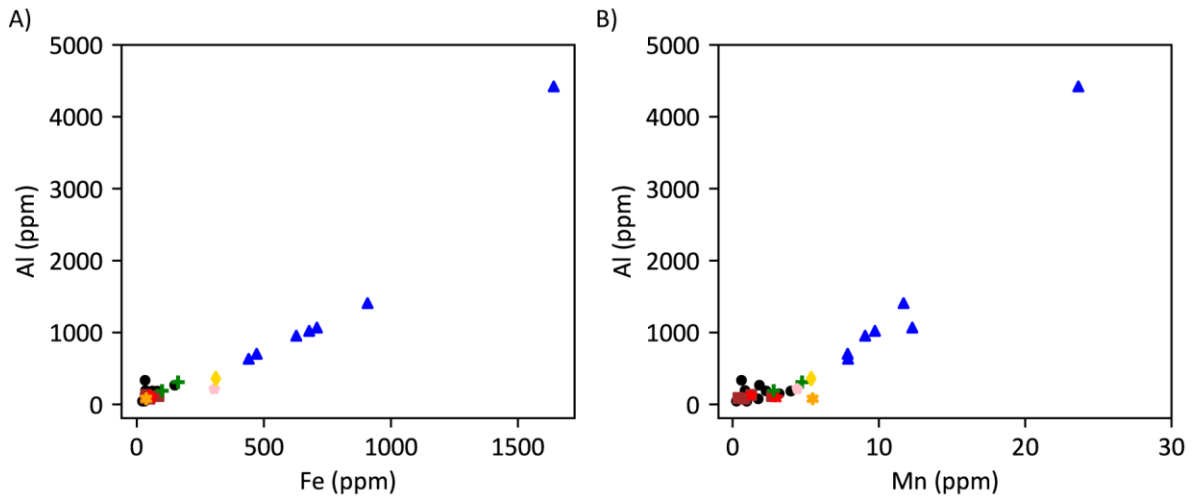

Figure 9. Fe-Al and Mn-Al cross plots using ICP-MS data for Two Pines roadcut and sediment samples. Data point symbols follow the scheme of figure 1.

Th (ppm) (figure 7) concentrations in the TP samples range from 0.10 ppm to 1.32 ppm (average = 0.28 ± 0.33 ppm, 1σ). TP samples show a sharp decrease in Th concentrations 2.1 m to 2.0 m and a gradual decline in Th concentrations from 1.9 m to 0.9 m. All sediment samples have Th concentrations which fall within the range of values given by TP samples. These sediment samples have Th concentrations ranging from 0.11 ppm to 0.68 ppm (average = 0.23 ± 0.15 ppm, 1σ).

U (ppm) (figure 7) concentrations in the TP samples range from 2.25 ppm to 5.11 ppm (average = 3.53 ± 0.84 ppm, 1σ). TP samples show a gradual increase in U concentrations from 2.1 to 1.5 m and a gradual decline in U concentrations from 1.5 m to 0.9 m. All sediment samples, excluding GT, PCFM1, and PCFM3 1/2, have U concentrations which fall within the range of concentrations given by TP samples. These sediment samples have U concentrations ranging from 2.62 ppm to 4.70 ppm (average = 3.66 ± 0.65 ppm, 1σ).

Rb (ppm) (figure 8) concentrations in the TP samples range from 0.13 ppm to 2.39 ppm (average = 0.50 ± 0.59, 1σ). The TP samples show a drastic decrease in Rb concentrations from 2.1 m to 2.0 m and then a gradual decrease with small peaks at 1.2 m and 0.9 m. All sediment samples have Rb concentrations which fall within the range of concentrations given by TP samples and range from 0.14 ppm to 0.63 ppm (average = 0.26 ± 0.14 ppm, 1σ).

Mo (ppm) (figure 8) concentrations in the TP samples range from 0.07 ppm to 0.25 ppm (average = 0.11 ± 0.04 ppm, 1σ). Sediment samples SCNS, LC, GH, EL, BO1, BD, and PB have Mo concentrations which fall within the range of Mo concentrations given by TP samples with concentrations ranging from 0.1 ppm to 0.23 ppm (average = 0.14 ± 0.04 ppm, 1σ).

4.3.1. Fe, Al, and Mn

Comparing Fe and Mn concentration with Al concentrations by a linear regression model for each sample group (figure 9) reveals three significant correlations (table 8). These are between the following: (1) Fe and Al for SED-G1, $R^2 = 0.956$; (2) Fe and Al for SED-G2, $R^2 = 0.852$; and (3) Mn and Al for SED-G1, $R^2 = 0.955$.

4.3.2. Sulfur Correlations

When comparing S concentrations with the elements which showed the most significant difference between TP and sediment samples (Zn, Co, and Cu) and Fe with a linear regression model (figure 10), a few significant correlations appear (table 8). These are between the following: (1) Sulfur and Fe for SED-G1, $R^2 = 0.844$ and (2) Sulfur and Cu for SED-G1, $R^2 = 0.670$. A weaker correlation ($R^2 = 0.466$) occurs between the S and Cu concentrations of SED-G2.

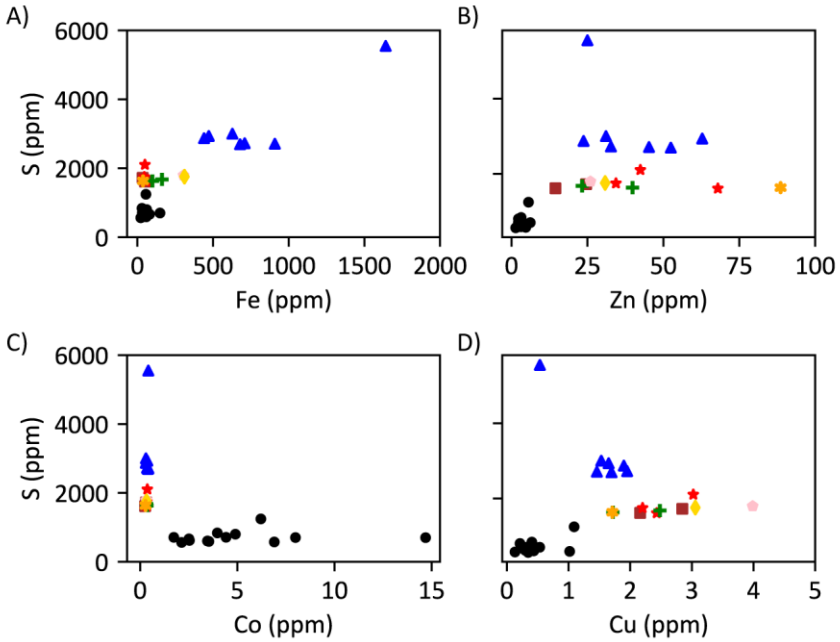

Figure 10. Cross plots of S and A) Fe, B) Zn, C) Co, and D) Cu for Two Pines roadcut and sediment samples. Data point symbols follow the scheme of figure 1.

4.4. Inorganic $\delta^{13}C$ and $\delta^{18}O$

4.4.1. Two Pines Versus Sediment Samples

$\delta^{13}C$ and $\delta^{18}O$ values for both TP and sediment samples are plotted in figure 11. Average values, R^2 values, and two-tailed t-test results are available in table 3. On average, $\delta^{13}C$ and $\delta^{18}O$ values for TP samples are lower than both sediment sample groups with a two-tailed t-test showing $\delta^{13}C$ and $\delta^{18}O$ values from TP are also statistically different from both sediment sample groups. The t-test also indicates $\delta^{18}O$ values between SED-G1 and SED-G2 are not significantly

different. R^2 values from each samples group display varying degrees of linear correlation between $\delta^{13}C$ and $\delta^{18}O$. The most significant R^2 values is for the TP samples (R^2 = 0.495) followed by SED-G2 samples (R^2 = 0.283) and then SED-G1 samples (R^2 = 2.0x10^{-5}).

Plots of calcite and aragonite versus $\delta^{18}O$ (figure 12) for both TP and sediment samples indicate two significant linear correlations (table 5). These being a positive linear correlation between calcite and $\delta^{18}O$ for TP samples and a negative linear correlation between aragonite and $\delta^{18}O$ for TP samples. SED-G1 data show a slight negative linear correlation between calcite and $\delta^{18}O$, however this value appears to be driven by two datapoints (GH and GT) and not representative of PC samples.

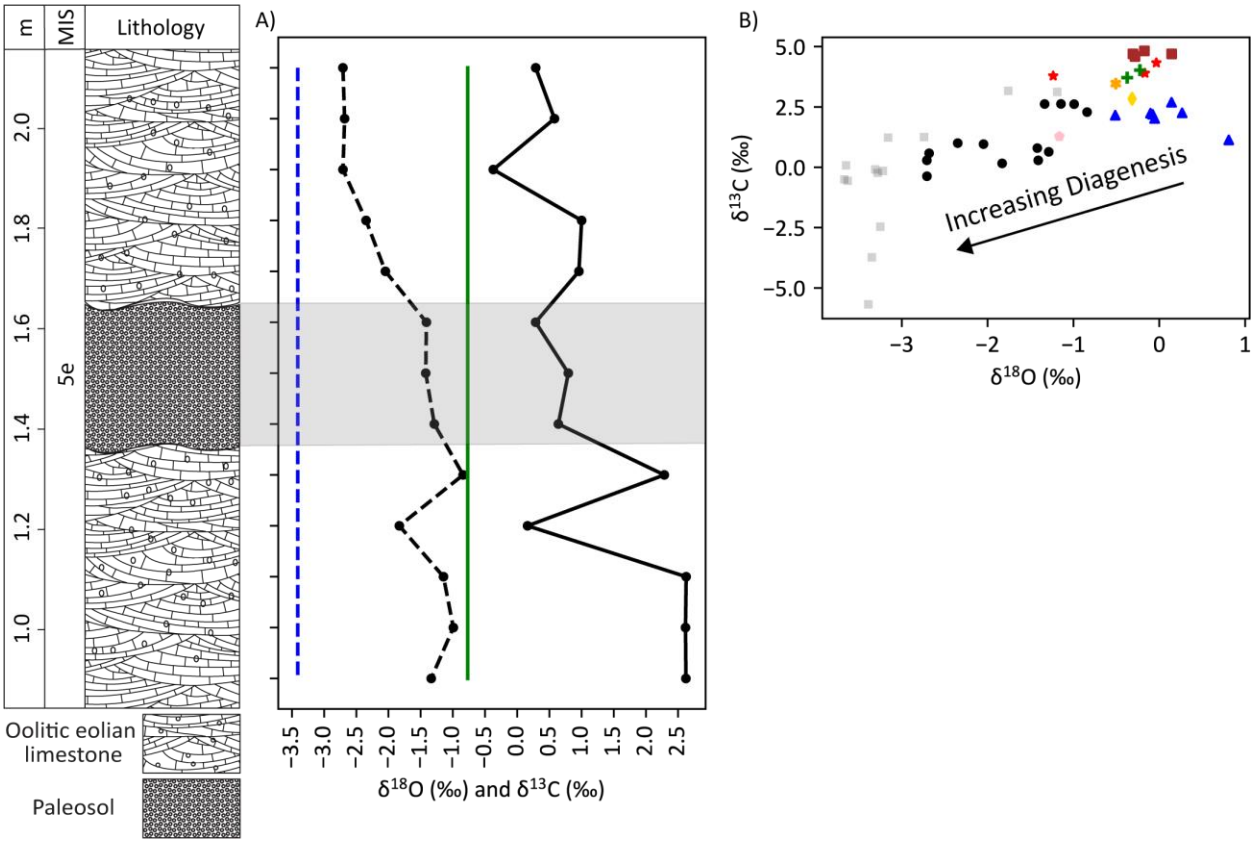

Figure 11. A) Inorganic $\delta^{13}C$ and $\delta^{18}O$ values plotted for Two Pines roadcut samples relative to position above ground level (m). Light grey bar indicates the extent of the protosol. The data points connected by the dashed line are $\delta^{18}O$ and the data points connected by the solid line are $\delta^{13}C$. The vertical blue dashed line is average $\delta^{18}O_{LMC}$ and the vertical solid green line is average $\delta^{13}C_{LMC}$. B) Cross plot of $\delta^{13}C$ and $\delta^{18}O$ for Two Pines and sediment samples. Data point symbols follow the scheme of figure 1. Light grey squares are data from meteorically altered limestone measured by Melim et al. (2001).

4.4.2. Two Pines Variations

$\delta^{18}O$ values for the TP roadcut (figure 11.A.) show gradually increasing values from 2.1 m ($\delta^{18}O$ = -2.71 ‰) to 1.3 m ($\delta^{18}O$ = -0.84 ‰). There is then a decrease in values to 1.2 m ($\delta^{18}O$ = -1.83 ‰), an increase to 1.0 m ($\delta^{18}O$ = -0.99 ‰) and then a final decrease to 0.9 m ($\delta^{18}O$ = -1.34 ‰).

$\delta^{13}C$ values for the TP roadcut increase from 2.1m ($\delta^{13}C$ = 0.29 ‰) to 1.8 m ($\delta^{13}C$ = 1.00 ‰) with a low point at 1.9 m ($\delta^{13}C$ = -0.37 ‰). Values then decrease across the upper boundary of the protosol from 1.8 m ($\delta^{13}C$ = 1.00 ‰) to 1.6 m ($\delta^{13}C$ = 0.29 ‰). There is a spike in $\delta^{13}C$ across the base of the protosol from 1.4 m ($\delta^{13}C$ = 0.64 ‰) to 1.3m ($\delta^{13}C$ = 2.29 ‰). This is followed by a low point at 1.2 m ($\delta^{13}C$ = 0.16 ‰) and increase to 1.1 m ($\delta^{13}C$ = 2.62 ‰) where the values then remain stable.

4.4.3. Inorganic $\delta^{13}C$ and $\delta^{18}O$ modeling

Using XRD and inorganic $\delta^{13}C$ and $\delta^{18}O$ data, a model is used to calculate the $\delta^{13}C$ and $\delta^{18}O$ of the diagenetic low-magnesium calcite ($\delta^{13}C_{LMC}$; $\delta^{18}O_{LCM}$). Assuming pre-meteorically altered aragonite and high-magnesium calcite had $\delta^{18}O$ values of 0 ‰, as modern sediment samples have an average $\delta^{18}O$ of -0.22 ± 0.49 ‰, all calcite in the TP roadcut is diagenetic low-magnesium calcite, and the two main mineral components influencing $\delta^{18}O$ of the TP roadcut to be aragonite and low-magnesium calcite (where aragonite + low-magnesium calcite = 100 %), the model for $\delta^{18}O_{LCM}$ follows the following equation:

Table 2. $\delta^{18}O_{LCM}$ and $\delta^{13}C_{LMC}$ results from model equations (11) and (12).

Sample Name	Low-magnesium calcite (%)	$\delta^{18}O_{LCM}$	$\delta^{13}C_{LMC}$
TP 13	61.9	-4.37	-1.40
TP 12	64.1	-4.18	-0.79
TP 11	59.5	-4.55	-2.68
TP 10	54	-4.35	-0.72
TP 9	48.3	-4.24	-1.25
TP 8	40.5	-3.48	-3.74
TP 7	40.5	-3.51	-2.48
TP 6	41.8	-3.08	-2.68
TP 5	53.3	-1.58	1.64
TP 4	53.8	-3.40	-2.30
TP 3	45.2	-2.53	2.14
TP 2	46.2	-2.15	2.14
TP 1	46.8	-2.85	2.16

$$\delta^{18}O_{LMC} = \frac{\delta^{18}O_{BULK}}{C} \quad (11)$$

where C = percent low-magnesium calcite ($0 \leq C \leq 1$; where 1 = 100 %). Assuming pre-meteorically altered aragonite and high-magnesium calcite had $\delta^{13}C$ of the average value for modern sediments ($\delta^{13}C_{MODERN}$ = 3.02 ‰) and keeping the previous assumptions the same, the model for $\delta^{13}C_{LMC}$ follows the following equation:

$$\delta^{13}C_{LMC} = \frac{\delta^{13}C_{BULK} - (A)\left(\delta^{13}C_{MODERN}\right)}{C} \quad (12)$$

where C = percent low-magnesium calcite (0 ≤ C ≤ 1; where 1 = 100 %) and A = percent aragonite (0 ≤ A ≤ 1; where 1 = 100 %). Results from the models are reported in table 2 and average values plotted in figure 11.

4.5. $\delta^{34}S$ and Organic $\delta^{13}C$ and $\delta^{15}N$

Organic $\delta^{13}C$ and $\delta^{15}N$ of sediment samples have a wide range of values for both $\delta^{13}C$ and $\delta^{15}N$. Using average values for sediment samples PCBM, PCFM 3 1/2, and PCFM 3 2/2, $\delta^{13}C$ values range from -23.2 ‰ to -11.9 ‰ (average = -17.0 ± 2.58 ‰, 1σ). Using average values for

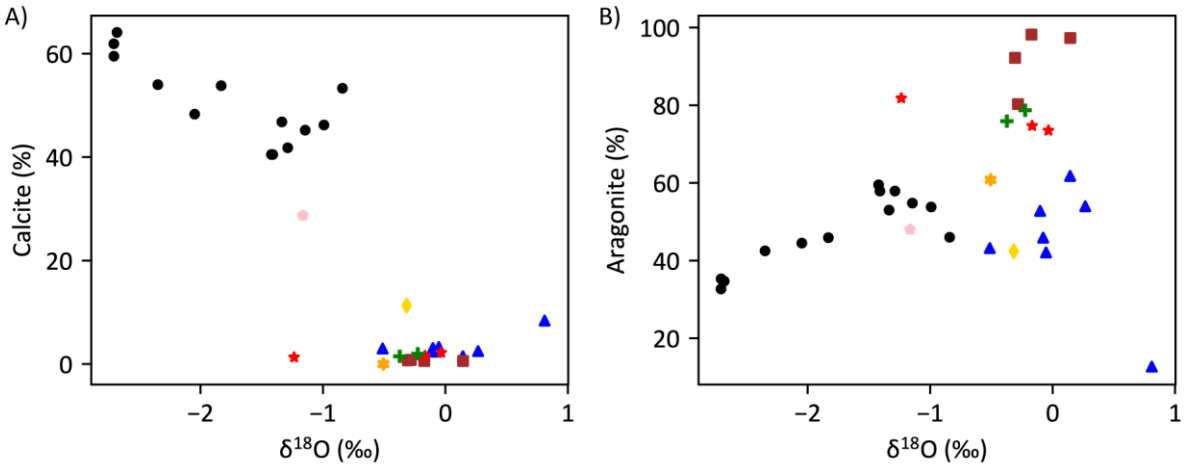

Figure 12. Cross plots of A) calcite and B) aragonite versus $\delta^{18}O$ for Two pines and sediment samples. Data point symbols follow the scheme of figure 1.

Table 3. Average $\delta^{13}C$ and $\delta^{18}O$ values and t-test results for TP, SED-G1, and SED-G2 samples groups.

Sample Group	Average $\delta^{13}C$ (‰)	Average $\delta^{18}O$ (‰)	R^2
TP	1.11 ± 1.05	-1.75 ± 0.68	0.495
SED-G1	2.09 ± 0.57	–0.11 ± 0.54	$2.0x10^{-5}$
SED-G2	4.20 ± 0.49	–0.32 ± 0.37	0.283
T-test (two-tailed)	$\delta^{13}C$	$\delta^{18}O$	-
TP; SED-G1	0.011	$4.6x10^{-6}$	-
TP; SED-G2	$2.8x10^{-8}$	$3.2x10^{-6}$	-
SED-G1; SED-G2	$2.0x10^{-7}$	0.361	-

sediment samples PCBM, PCFM 3 1/2, and PCFM 3 2/2, $\delta^{15}N$ values range from -0.23 ‰ to 4.17 ‰ (average = 1.63 ± 0.98 ‰, 1σ).

$\delta^{34}S$ of sediment samples range from -30.3 ‰ to 10.6 ‰ (average = -5.4 ± 14.19 ‰, 1σ). R^2 values are reported in table 8 with significant R^2 values between organic $\delta^{13}C$ and $\delta^{34}S$ for SED-G1 (R^2 = 0.949), inorganic $\delta^{13}C$ and $\delta^{34}S$ for the total sediment dataset (R^2 = 0.705), and for $\delta^{34}S$ and organic $\delta^{13}C$ for the total sediment dataset (R^2 = 0.692). While the total

sediment dataset provides a significant correlation between inorganic $\delta^{13}C$ and $\delta^{34}S$, significant R^2 values are not calculated individually for SED-G1 or SED-G2.

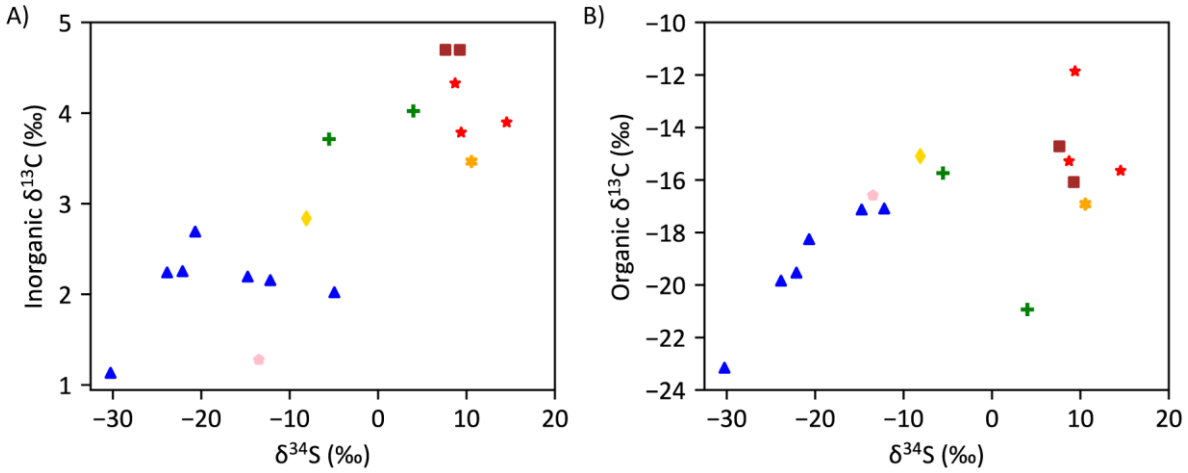

Figure 13. Cross plots of A) inorganic $\delta^{13}C$ versus $\delta^{34}S$ for sediment samples and B) organic $\delta^{13}C$ versus $\delta^{34}S$ for sediment samples. Data point symbols follow the scheme for figure 1.

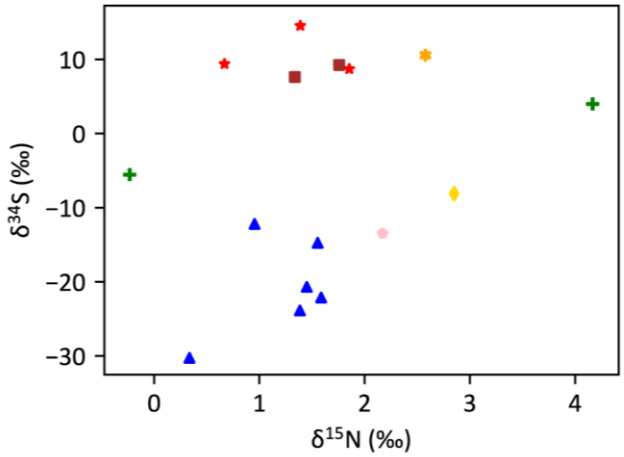

Figure 14. Cross plot of $\delta^{34}S$ versus organic $\delta^{15}N$ for sediment samples. Data point symbols follow the scheme for figure 1.

$\delta^{34}S$ and organic $\delta^{15}N$ for sediment samples are plotted together (figure 14) and correlations between the two for each sediment sample group are in table 8. The data show a negative linear correlation between $\delta^{34}S$ and organic $\delta^{15}N$ for SED-G1 and no correlation for SED-G2. There is no statistical difference in between organic $\delta^{15}N$ values for SED-G1 and SED-G2 (two-tailed T-test gives 0.45).

4.5.1 $\delta^{34}S$ model

A linear model may be used for calculating the relative proportions of organic S and pyrite S in modern sediment samples using a few assumptions: (1) a fractionation of -30 ‰ for

pure pyrite S ($\delta^{34}S_{PYR}$) based on sample PCFM1, the only sample with pyrite in XRD, having $\delta^{34}S$ of ~ -30 ‰; (2) a fractionation of 10 ‰ for pure organic S ($\delta^{34}S_{ORG}$) as sample in an oxic environment with little to no microbial sulfate reduction is expected (SCNS, SCOS, BO1, BD, PB, and EL) have an average $\delta^{34}S$ of 10.01 ‰; and (3) net fractionation is dependent mainly on pyrite S and organic S in the residual material from HCl dissolution of the carbonate sediments. With these assumptions the amount of organic S (S_{ORG}) and pyrite S (S_{PYR}) may be calculated by the following equations:

$$S_{ORG}=\left(\frac{\delta^{34}S_{BULK}+30\text{ ‰}}{0.4\text{ ‰}}\right)/100 \quad (13)$$

$$S_{PYR}=1-S_{ORG} \quad (14)$$

where $0\leq S_{ORG}\leq 1$ and $0\leq S_{PYR}\leq 1$, and 1 = 100 %. Results from the model calculations are reported in table 4.

Table 4. S_{ORG} and S_{PYR} calculated from model equations (13) and (14). Asterisks indicate values rounded up to 0.00 or down to 1.00 as they were calculated to be negative or above 1.00.

Sample Name	S_{ORG}	S_{PYR}
PCFM1	0.00*	1.00*
PCFM 3 1/2	0.15	0.85
PCM3A	0.63	0.37
PCM3	0.45	0.55
PCM4	0.38	0.62
PCBM	0.23	0.77
PCFM 3 2/2	0.20	0.80
SCOS	0.94	0.06
SCNS	0.98	0.02
BO1	0.97	0.03
BD	0.98	0.02
PB	1.00*	0.00*
RC	0.61	0.39
LC	0.85	0.15
GT	0.41	0.59
GH	0.55	0.45
EL	1.00*	0.00*

4.6. REY

4.6.1. REY Distributions

Due to low measured counts of MREE during ICP-MS analysis, concentrations of the MREE were calculated on the low end of the calibration curve. This led to poor quantification of MREE concentrations and a spikey nature of MREEs when normalized against PAAS. LREE and

HREE measurements were not as affected and therefore major trends and features of the data are still visible and readily interpretable.

Table 5. R^2 values for cross plots of calcite and aragonite versus $\delta^{18}O$ see in figure 12.

Sample group	Calcite vs $\delta^{18}O$ (R^2)	Aragonite vs $\delta^{18}O$ (R^2)
TP	0.591	0.701
SED-G1	0.411	0.163
SED-G2	0.004	0.069

REY distributions are plotted in (figure 15) and anomalies in (figure 16). Sediment REY distributions (figure 15B and C) show two distinct groups between SED-G1 and SED-G2. SED-G1 contains samples PCFM1, PCM3, PCM3 1/2, PCM3 2/2, PCM3A, PCM4, PCBM, GT, and GH. SED-G2 contains samples SCOS, SCNS, SCPO, SCNO, RC, LC, BO1, EL, BD, and PB. SED-G1 is most easily distinguished from SED-G2 and TP samples by its flatter REY distribution, significantly lower HREE enrichment, and more positive Ce anomaly than SED-G2. While TP samples and SED-G2 samples have visually similar REY patterns, TP samples can be most easily distinguished from SED-G2 by a greater HREE enrichment, lower total REY, and more negative Ce anomalies in TP samples.

REY anomaly values are available in (table 6) with t-tests between each group for each anomaly. Average Y/Ho ratios, total REY, and HREE enrichment are available in (table 7) with t-tests for these parameters between each group.

4.6.2. Clay Leaching and Ba Interference

Fe and Al display significantly increased concentrations for Y/Ho values below ~ 45 for SED-G1 (figure 17A and B) with significant R^2 values (table 8). R^2 values are insignificant for TP and SED-G2 for these plots. Ba/Sm show a clear positive linear correlation to Eu anomaly strength in both sediment and TP samples with significant R^2 values (figure 17C; table 8).

4.6.3. REY and Major Carbonate Phases

Several significant linear correlations occur between the three major carbonate mineral phases (calcite, magnesium calcite, and aragonite) for both TP and sediment samples and the parameters HREE enrichment, Total REY, Y anomalies, and Ce anomalies and are available in table 8. As well, between each sample group for each carbonate mineral phase, various R^2 values are produced from the linear regression model. For example, $R^2 = 0.612$ when comparing TP calcite concentrations versus TP sample Ce anomalies via a linear regression model while $R^2 = 0.02$ for the same comparison for SED-G2 samples. The most significant correlations ($R^2 \geq$ ~ 0.6) occur between the following: (1) Calcite and Ce_{SN}/Ce_{SN}^* for TP samples, $R^2 = 0.612$; (2) Calcite and HREE enrichment for SED-G1, $R^2 = 0.812$; (3) Magnesium calcite and total REY for SED-G2, $R^2 = 0.597$; (4) Magnesium calcite and Y/Ho for SED-G2, $R^2 = 0.684$; (5) Aragonite and Ce_{SN}/Ce_{SN}^* for TP samples, $R^2 = 0.595$; (6) Aragonite and total REY for SED-G1, R^2 0.681; (7) Aragonite and total REY for SED-G2, $R^2 = 0.638$; and (8) Aragonite and Y/Ho for SED-G2, $R^2 = 0.718$. A few weaker correlations occur as well between the following: (1) Calcite and HREE

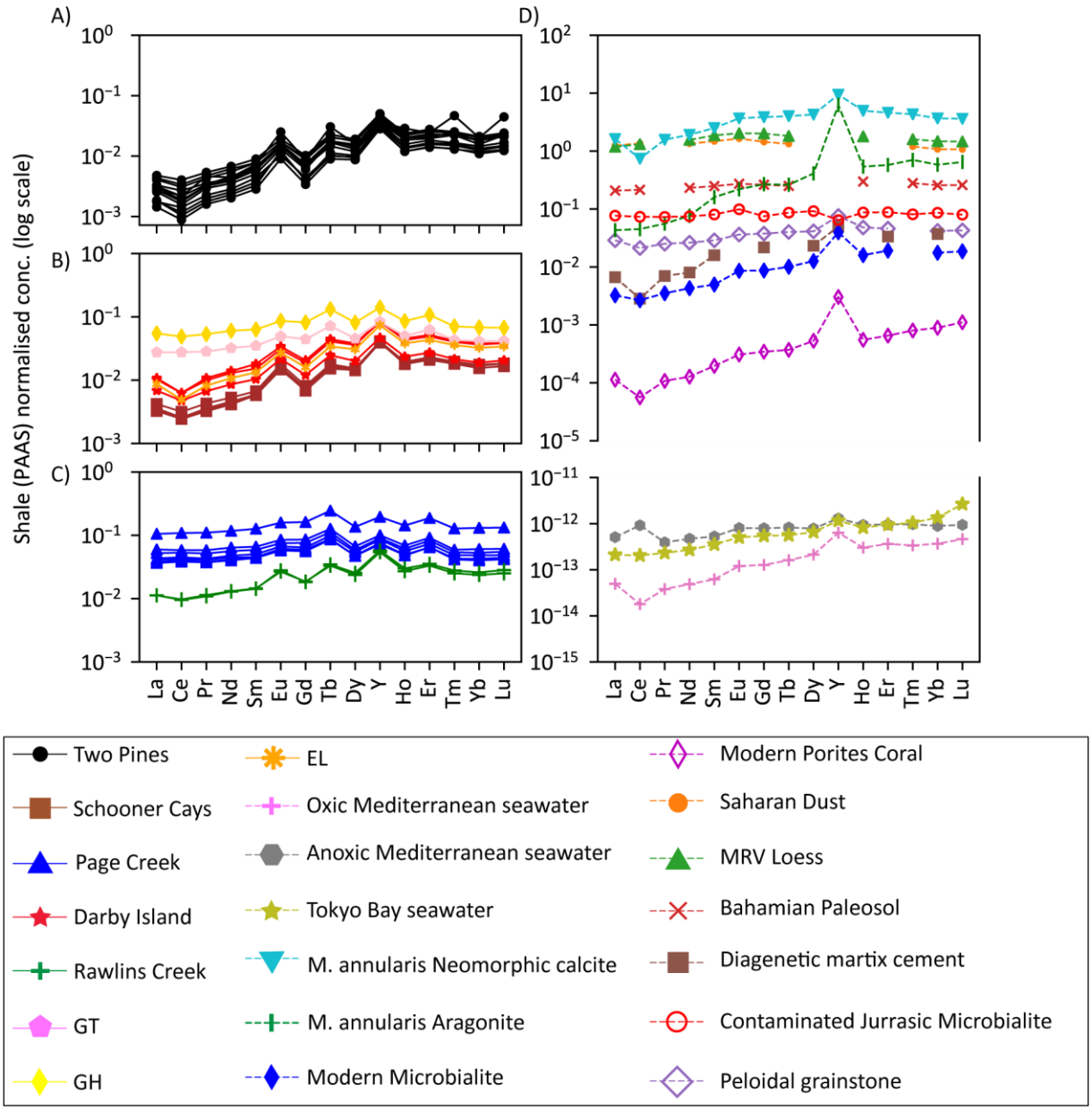

Figure 15. A) REY data from Two Pines roadcut samples. B) REY data from Schooner Cays, Gregory Town, Governors Harbor, Lighthouse beach, and Darby island samples. C) REY data from Page Creek and Rawlins Creek Samples. D) Previously published REY data. Saharan dust, Mississippi River Valley (MRV) loess, and Bahamian paleosol data from Muhs et al. (2007). Peloidal grainstone from Nothdurft et al. (2004). Diagenetic matrix cement from Li and Jones (2014).Oxic and Anoxic Mediterranean seawater from Bau et al. (1997). Tokyo Bay seawater from Nozaki and Zhang (1995). *M. annularis* neomorphic calcite and aragonite from Webb et al. (2009). Modern microbialite from Webb and Kamber (2000). Contaminated Jurrasic microbialite from Olivier and Boyet (2006). Modern *Porities* coral from Jupiter (2008).

enrichment for SED-G1, $R^2 = 0.449$; (2) Magnesium calcite and Y/Ho for SED-G1, $R^2 = 0.507$; and (3) Aragonite-TP and Y/Ho, $R^2 = 0.426$.

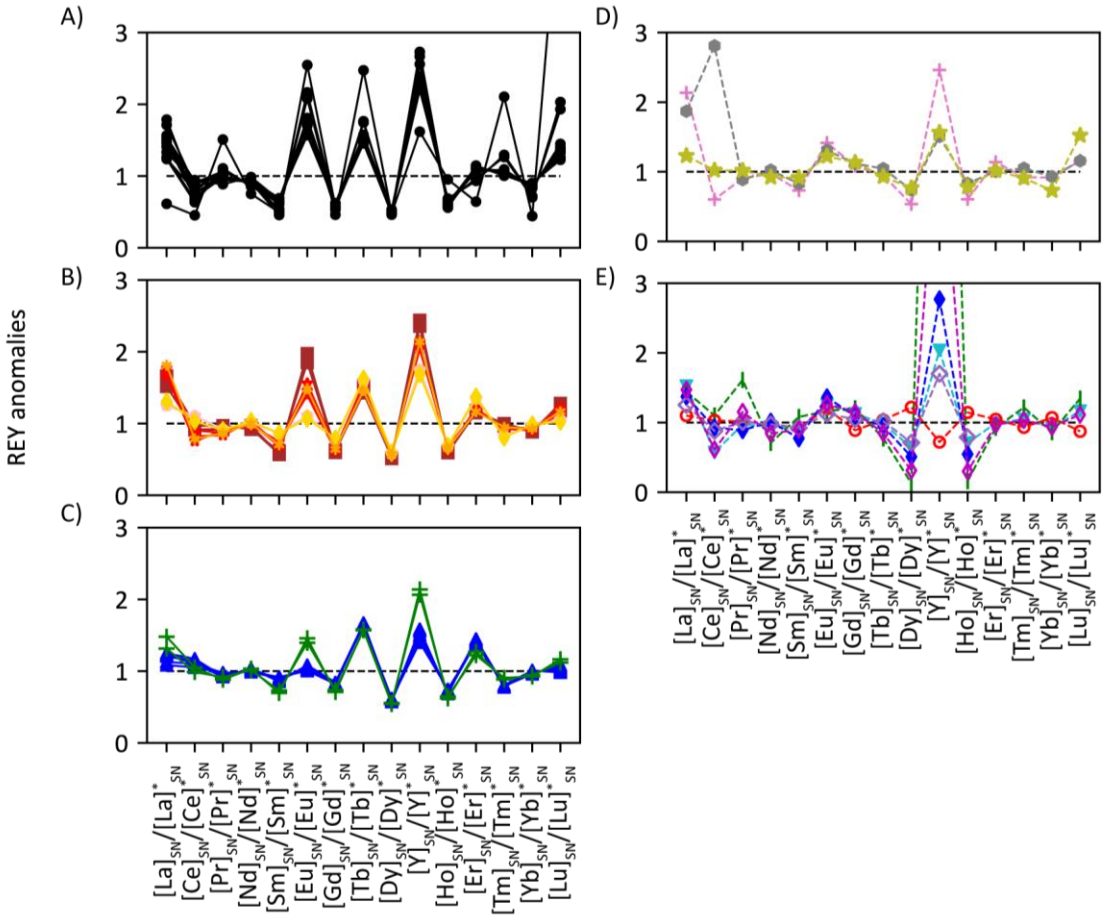

Figure 16. A) REY anomaly data from Two Pines roadcut samples. B) REY anomaly data from Schooner Cays, Gregory Town, Governors Harbor, Lighthouse beach, and Darby island samples. C) REY anomaly data from Page Creek and Rawlins Creek Samples. D) Anomalies calculated from previously published REY data. See figure 12 for legend and previously published data sources.

5. DISCUSSION

5.1. Mineralogic Stabilization with Diagenesis

It is well known that metastable aragonite and low-magnesium, which are more soluble than low-magnesium calcite (Chave et al., 1962), stabilize to diagenetic low-magnesium calcite when exposed to fresh water (e.g. Land, 1967; Matthews, 1968, Jian et al., 1997).

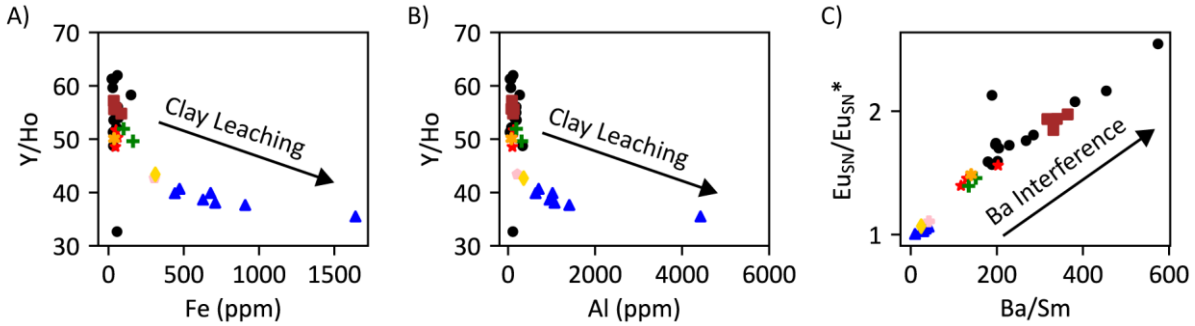

Figure 17. Cross plots of the Y/Ho ratio versus A) Fe and B) Al for Two Pines roadcut and sediment samples. C) Cross plot of Eu anomaly and Ba/Sm ratio for Two Pines roadcut and sediment samples. Data point symbols follow the scheme for figure 1.

This stabilization is evident in the XRD data of this study (figure 3; table 1). Most notably, TP samples have a total absence of high-magnesium calcite while SED-G1 and SED-G2 samples have an average high-magnesium calcite of 46.05 ± 11.55 % (1σ) and 17.5 ± 11.58 % (1σ) respectively. Likewise, TP samples have an abundance of low-magnesium calcite (average = 50.45 ± 8.00 %, 1σ) while SED-G1 and SED-G2 have significantly less with an average content of 7.13 ± 8.72 % (1σ) and 1.13 ± 0.70 % (1σ) respectively. It should be noted while some stabilization of aragonite certainly did occur in TP samples (average aragonite = 47.58 ± 9.37 %, 1σ), the aragonite content is greater than that of SED-G1 (average = 44.77 ± 13.67 %, 1σ) but significantly lower than SED-G2 (average = 81.34 ± 11.65 %, 1σ). This indicates that TP samples initially had a greater aragonite content prior to diagenesis than SED-G1 samples and that TP samples have not been exposed for a significant enough amount of time, or to enough meteoric water, to completely stabilize all aragonite in the section. This likely also led to the poor cementation seen in the section. Similar results have been noted by Matthews (1968) in a study of a Pleistocene coral cap in Barbados. They noted that older lithologies contained a greater amount of stable minerals, and that localities that receive less rainfall retained more unstable minerals to a greater age. Likewise, Li et al. (2018) in their study of meteorically altered Pleistocene eolianites at Shidao, Xisha Islands, have attributed poor lithification and less mineralogic stabilization of the eolianite to low water/rock ratios during alteration. This is relevant to this study as some cryptic carbonate sequence boundaries may have experienced less interaction with meteoric water due to short exposure times.

The XRD data indicate that diagenetic stabilization has occurred in all TP samples and likely the entire section as seen by the absence of high-magnesium calcite and significant amounts of low-magnesium calcite in all samples compared to SED-G1 and SED-G2. As well, all

TP samples have likely been exposed to similar amounts of meteoric water as they have most likely been exposed for similar amounts of time. This is because both eolianites below and

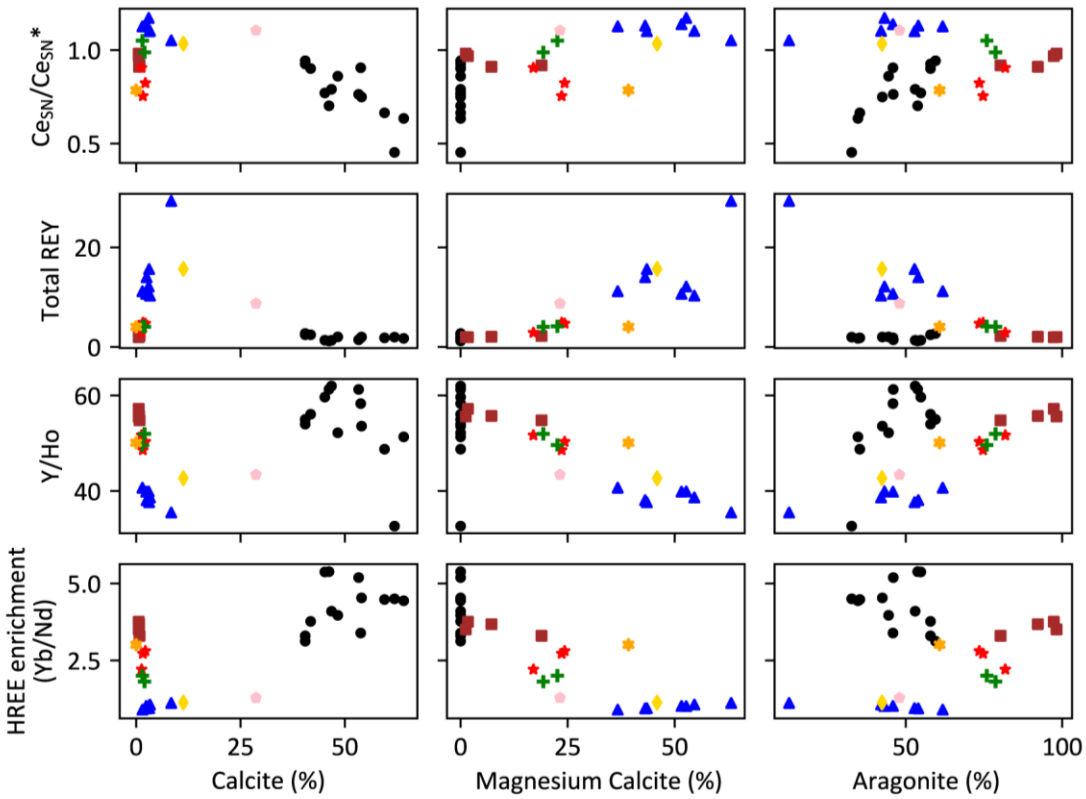

Figure 18. Cross plots of Ce anomalies, total REY, Y/Ho ratios, and HREE enrichment versus carbonate mineral fractions for Two Pines roadcut and sediment samples. Data point symbols follow the scheme of figure 1.

above the protosol were deposited during MIS 5e (Hearty and Kindler, 1993) with sea-level records indicating the sea-level has not risen to similar high stand levels on Eleuthera since MIS 5e (Hearty and Kindler, 1995; Hearty, 2000) and data indicating minimal to zero subsidence has occurred since MIS 5e (Carew and Mylroie, 1995; Strasser et al., 1997). This implies that all TP samples should have been chemically affected similarly and this is supported when considering the REY, trace-element, and isotope data presented in this study. For example, similarly low Zn concentrations for all TP samples when compared to SED-G1 and SED-G2 (figure 6).

5.2. Inorganic $\delta^{13}C$ and $\delta^{18}O$ Variations

A Previous study by Allan and Matthews (1982) sought to show how inorganic $\delta^{13}C$ and $\delta^{18}O$ values of limestones were altered during vadose and phreatic freshwater diagenesis. They postulated that the $\delta^{13}C$ value of precipitating diagenetic calcite is a function of the number of moles of carbon input from dissolving aragonite and high-magnesium calcite (C_L) and the number of moles of carbon input from soil-gas CO_2 (C_{SG}), or C_L/C_{SG}. As C_L would typically have the same $\delta^{13}C$ as the dissolving minerals and C_{SG} would have a $\delta^{13}C$ similar to the organic material (Cerling et al., 1991), more input of soil-gas CO_2 after subaerial exposure and soil

formation would lead to decreased $\delta^{13}C$ near the paleosol and increase farther away from the paleosol. This would also impart high variability in the $\delta^{13}C$ data of meteorically altered sections. On the other hand, $\delta^{18}O$ was noted to be controlled by O_L/O_W where O_L is the number of moles of oxygen derived from the dissolving carbonate minerals and O_W is the number of moles of oxygen derived from meteoric water. The $\delta^{18}O$ data of a meteorically altered section was noted to be less variable than $\delta^{13}C$ due to the ubiquity of meteoric water in meteoric diagenesis. Since soil-gas CO_2 should be similar to the organic material being respired (Cerling et al., 1991) with organic material having very negative $\delta^{13}C$ values (O'leary, 1988), meteorically altered limestone should have a more negative $\delta^{13}C$ value than the original sediments. Allan and Matthews (1982) found that altered limestone near soil zones should be approximately 2-4 ‰ lighter than the original sediments. Likewise, the $\delta^{18}O$ of meteorically altered limestones should be lighter than the original sediments, as meteoric water is enriched in ^{16}O. The exception to this is when evaporation is high enough, generally near the surface, to evaporate ^{16}O and cause an enrichment in ^{18}O. This evaporation process is thought to have led to inversely correlated $\delta^{13}C$ and $\delta^{18}O$ at exposure surfaces in a study by Swart and Oehlert (2018).

Table 6. Average REY anomalies and T-test results for each sample group

Anomaly	Sample group average anomaly (±1 σ)			T-test (two-tailed)		
	TP	SED-G1	SED-G2	TP; SED-G1	TP; SED-G2	SED-G1; SED-G2
$\frac{[La]_{SN}}{[La]^*_{SN}}$	1.40 ± 0.29	1.21 ± 0.07	1.62 ± 0.15	0.045	0.027	2.6×10^{-6}
$\frac{[Ce]_{SN}}{[Ce]^*_{SN}}$	0.77 ± 0.14	1.11 ± 0.04	0.91 ± 0.10	7.5×10^{-7}	0.012	5.2×10^{-5}
$\frac{[Pr]_{SN}}{[Pr]^*_{SN}}$	1.04 ± 0.15	0.94 ± 0.02	0.90 ± 0.04	0.029	6.7×10^{-3}	0.040
$\frac{[Nd]_{SN}}{[Nd]^*_{SN}}$	0.89 ± 0.05	1.02 ± 0.02	0.98 ± 0.04	1.5×10^{-6}	1.3×10^{-4}	0.038
$\frac{[Sm]_{SN}}{[Sm]^*_{SN}}$	0.61 ± 0.08	0.88 ± 0.02	0.66 ± 0.07	6.7×10^{-9}	0.102	1.2×10^{-6}
$\frac{[Eu]_{SN}}{[Eu]^*_{SN}}$	1.86 ± 0.29	1.06 ± 0.03	1.64 ± 0.25	2.9×10^{-7}	0.072	3.1×10^{-5}
$\frac{[Gd]_{SN}}{[Gd]^*_{SN}}$	0.57 ± 0.04	0.82 ± 0.02	0.65 ± 0.04	6.6×10^{-13}	2.7×10^{-4}	3.3×10^{-8}
$\frac{[Tb]_{SN}}{[Tb]^*_{SN}}$	1.64 ± 0.27	1.65 ± 0.02	1.51 ± 0.05	0.864	0.131	1.5×10^{-6}

(table cont'd.)

Anomaly	Sample group average anomaly (±1 σ)			T-test (two-tailed)		
	TP	SED-G1	SED-G2	TP; SED-G1	TP; SED-G2	SED-G1; SED-G2
$\frac{[Dy]_{SN}}{[Dy]^*_{SN}}$	0.50 ± 0.02	0.59 ± 0.01	0.55 ± 0.03	5.5×10^{-10}	1.5×10^{-4}	3.6×10^{-4}
$\frac{[Y]_{SN}}{[Y]^*_{SN}}$	2.40 ± 0.30	1.56 ± 0.01	2.23 ± 0.16	7.0×10^{-8}	0.089	8.4×10^{-9}
$\frac{[Ho]_{SN}}{[Ho]^*_{SN}}$	0.63 ± 0.10	0.71 ± 0.02	0.63 ± 0.02	0.029	0.851	8.3×10^{-7}
$\frac{[Er]_{SN}}{[Er]^*_{SN}}$	1.05 ± 0.14	1.40 ± 0.03	1.19 ± 0.04	4.3×10^{-7}	3.7×10^{-3}	1.3×10^{-10}
$\frac{[Tm]_{SN}}{[Tm]^*_{SN}}$	1.17 ± 0.30	0.80 ± 0.01	0.95 ± 0.04	7.8×10^{-4}	0.022	1.0×10^{-7}
$\frac{[Yb]_{SN}}{[Yb]^*_{SN}}$	0.81 ± 0.12	0.99 ± 0.02	0.92 ± 0.02	2.3×10^{-4}	7.8×10^{-3}	4.3×10^{-7}
$\frac{[Lu]_{SN}}{[Lu]^*_{SN}}$	1.73 ± 1.05	1.03 ± 0.03	1.19 ± 0.05	0.033	0.085	1.1×10^{-6}

In cases of positively covariance of inorganic $\delta^{13}C$ and $\delta^{18}O$ in limestones, Allan and Matthews (1982) suggested that this is due to alteration in the mixing zone below the phreatic lens as the influence of marine water enriched in ^{18}O would increase with depth and the amount of ^{12}C would decrease with depth from decreased influence of organically derived CO_2. Future studies (e.g. Fike et al., 2006; Li et al., 2018) have used such presence or absence of covariance to make inferences about alteration of their carbonate samples. Recently, however, Swart and Oehlert (2018) have revised interpretations on this and instead suggest that covariation may be a product of meteoric diagenesis in the phreatic lens as opposed to the mixing zone. They propose build up and oxidation of organic material near the surface of the water table would to input of ^{12}C which decreases with depth and a decreasing degree of meteoric alteration (there by increasing $\delta^{18}O$) with depth would be the cause for the covariation. As well, they found no overall correlation between $\delta^{13}C$ and $\delta^{18}O$ in limestones altered by vadose meteoric diagenesis, indicating that a lack of correlation does not imply limestones were not affected by meteoric diagenesis. Positive covariation also may not be completely indicative of meteoric diagenesis as such covariation could also be attained by a mixing of different carbonate sources (Allan and Matthews, 1982).

The inorganic $\delta^{13}C$ and $\delta^{18}O$ data presented in this study for TP samples show evidence for meteoric diagenesis when compared to modern sediment samples collected in this study as well as other previously published data. TP samples have significantly lighter $\delta^{13}C$ (average = 1.11 ± 1.05 ‰, 1σ) and $\delta^{18}O$ (average = -1.75 ± 0.68 ‰, 1σ) on average (table 3, figure 11B) than SED-G1 and SED-G2 samples. The lighter $\delta^{13}C$ and $\delta^{18}O$ values with respect to sediment

samples are most likely due to input of soil-gas CO_2 and meteoric water respectively as discussed above. The $\delta^{13}C$ and $\delta^{18}O$ values measured in TP samples are likewise lighter than inorganic $\delta^{13}C$ and $\delta^{18}O$ values measured by Swart et al. (2009) from modern sediment west of Andros on the GBB. These sediments had an average bulk inorganic $\delta^{13}C$ of 4.8 ± 0.3 ‰ and an average bulk inorganic $\delta^{18}O$ of 0.4 ± 0.4 ‰, both of which are similar to modern sediment values presented in this study (table 3). The values measured for TP samples, however, appear generally more enriched in heavier isotopes than other meteorically altered limestones. For example, meteorically altered Pleistocene limestones from the Clino and Unda core taken on the GBB have an average $\delta^{13}C$ of -2.5 ‰ and an average $\delta^{18}O$ of -3.5 ‰ (Melim et al., 1995; Melim et al., 2001). Likewise, Jian et al. (1997) measured more highly negative $\delta^{13}C$ and $\delta^{18}O$ in Pleistocene reef limestone on the Xisha Islands. The more relative enriched $\delta^{13}C$ and $\delta^{18}O$ of meteorically altered limestones in this study are likely a result of lower amount of meteoric stabilization which, as mentioned previously, is evident from the poorly cemented nature of the TP section. This is because lower amounts of stabilization would yield a higher proportion of ^{13}C and ^{18}O enriched carbonates in the bulk rock compared to low $\delta^{13}C$ and $\delta^{18}O$ values in the diagenetic low-magnesium calcite.

Table 7. Average REY parameters for TP and sediment sample groups as well as t-test comparisons between groups.

Sample Group	Y/Ho (± 1σ)	Total REY (± 1σ)	HREE Enrichment (± 1σ)
TP	54.30 ± 7.73	1.88 ± 0.47	4.27 ± 0.76
SED-G1	39.61 ± 2.48	14.19 ± 6.16	1.05 ± 0.12
SED-G2	52.55 ± 3.02	3.29 ± 1.19	2.88 ± 0.70
T-test (Two-tailed)			
TP; SED-G1	$1.1x10^{-5}$	$3.2x10^{-4}$	$1.5x10^{-9}$
TP; SED-G2	0.466	$4.4x10^{-3}$	$1.8x10^{-4}$
SED-G1; SED-G2	$1.2x10^{-8}$	$6.5x10^{-4}$	$1.3x10^{-5}$

Although TP samples do show light $\delta^{13}C$ and $\delta^{18}O$ values expected with meteoric diagenesis, they show an atypical trend to what has been traditionally described (Allan and Matthews, 1982; Swart and Oehlert, 2018). These samples show relatively more enriched $\delta^{13}C$ and $\delta^{18}O$ within and below the protosol as opposed to above the protosol. The possibility that these more enriched values are from phreatic meteoric diagenesis is low, despite the slight covariation between $\delta^{13}C$ and $\delta^{18}O$ seen in the data (figure 11B; table 3). This is because sea-level curves indicate sea-level remaining well below MIS 5e levels until the Holocene (Hearty and Kindler, 1995; Hearty 2000). Instead the covariation and increase in $\delta^{13}C$ and $\delta^{18}O$ across the protosol must be due to a different process.

One possibility is differential cementation such that the protosol and lower eolianite were stabilized less than the upper eolianite. Evidence for this can be seen in the linear correlation between calcite and $\delta^{18}O$ in the TP section (figure 12, table 5). This correlation suggests that as more aragonite and high-magnesium calcite stabilizes to low-magnesium

calcite, the bulk $\delta^{18}O$ decreases due to the greater relative abundance of diagenetically precipitated low-magnesium calcite cement with low $\delta^{18}O$. If this is true, the upper eolianite should have a greater low-magnesium calcite content than the lower eolianite. Looking at the XRD data (table 1), the upper eolianite (samples TP13 – TP9) has an average low-magnesium calcite content of 57.56 ± 6.40 %. The lower eolianite (samples TP5 – TP1) has an average low-magnesium calcite content of 49.06 ± 4.14 %. While there is some overlap, the XRD data appear to coincide with inorganic $\delta^{13}C$ and $\delta^{18}O$ data, suggesting that the $\delta^{13}C$ and $\delta^{18}O$ variations in the TP section are influenced by differing amounts of diagenetic stabilization such that the upper eolianite may have experienced greater diagenetic stabilization. This assumes that the original (pre-diagenesis) low-magnesium calcite content of the TP samples were similar. This is valid as, the eolianites being mainly oolitic, likely had a main sedimentary source similar to the Schooner Cays where all XRD samples (including the non-ooid fraction) show similarly low low-magnesium calcite concentrations.

For this explanation, a question can be asked as to why the upper eolianite would be more cemented when the other was deposited first. A reason could lie in original mineralogical differences between the two eolianites. Kindler and Hearty (1996) provide petrographic data from thin sections describing the content on the eolianite deposits on various Bahamian islands in terms of ooid, bioclast, peloid, and miscellaneous materials content. While caution is advised

Table 8. R^2 values for plots in figures 9, 10, 13, 17, and 18.

Figure number		Parameters		
Figure 9	Al (ppm) (R^2)	-	-	-
Fe (ppm)-TP	0.224	-	-	-
Fe (ppm)-SED-G1	0.956	-	-	-
Fe (ppm)-SED-G2	0.852	-	-	-
Mn (ppm)-TP	0.081	-	-	-
Mn (ppm)-SED-G1	0.955	-	-	-
Mn (ppm)-SED-G2	0.151	-	-	-
Figure 10	Fe (ppm) (R^2)	Zn (ppm) (R^2)	Co (ppm) (R^2)	Cu (ppm) (R^2)
S (ppm)-TP	0.008	0.187	0.027	0.274
S (ppm)-SED-G1	0.844	0.017	0.235	0.670
S (ppm)-SED-G2	0.037	0.012	0.316	0.466
Figure 13	Inorganic $\delta^{13}C$ (R^2)	Organic $\delta^{13}C$ (R^2)	-	-
$\delta^{34}S$-SED-G1	0.108	0.949		
$\delta^{34}S$-SED-G2	0.020	0.003		
$\delta^{34}S$-SED-G1 & -G2	0.705	0.692		

(table cont'd.)

Figure number	Parameters			
Figure 17	Fe (ppm) (R^2)	Al (ppm) (R^2)	(Ba/Sm) (R^2)	-
Y/Ho-TP	0.001	0.021	-	-
Y/Ho-SED-G1	0.785	0.654	-	-
Y/Ho-SED-G2	0.111	0.102	-	-
Eu_{SN}/Eu_{SN}*-TP	-	-	0.544	-
Eu_{SN}/Eu_{SN}*-SED-G1	-	-	0.451	-
Eu_{SN}/Eu_{SN}*-SED-G2	-	-	0.949	-
Figure 18	Ce_{SN}/Ce_{SN}* (R^2)	Total REY (R^2)	Y/Ho (R^2)	HREE enrichment (R^2)
Calcite (%) - TP	0.612	0.002	0.303	0.105
Calcite (%) – SED-G1	0.115	0.002	0.332	0.812
Calcite (%) – SED-G2	0.002	0.285	0.243	0.449
Magnesium Calcite (%) - TP	-	-	-	-
Magnesium Calcite (%) - SED - G1	0.021	0.343	0.507	0.052
Magnesium Calcite (%) - SED - G2	0.302	0.597	0.684	0.251
Aragonite (%) - TP	0.595	0.025	0.426	0.075
Aragonite (%) – SED-G1	0.262	0.681	0.222	0.211
Aragonite (%) – SED-G2	0.295	0.638	0.718	0.285

in using this data to describe entire units on each island (1 thin section was used in some cases), the upper eolianite for all islands had more bioclastic content than the lower eolianite. It can then be inferred that the upper eolianite may have originally had more high-magnesium calcite than the lower based on the non-ooid fraction of the Schooner Cays (SCNO, large amounts of fossil carbonate) sample in this study had 17.7 % more high-magnesium calcite than the pure ooid fraction (SCPO, table 1). This is significant as the solubility of high-magnesium calcite is much greater than that of aragonite in fresh water (Chave et al., 1962) and is therefore more likely completely stabilize at a faster rate. Matthews (1974) also states in a review of carbonate diagenesis that rapid precipitation of low-magnesium calcite can occur with the presence of high-magnesium calcite, while aragonite does not provide enough saturation for rapid precipitation. An example of this rapid stabilization of high magnesium calcite can be seen in Bermuda Pleistocene limestones (Land, 1970) in which vadose altered limestones retain most primary aragonite but most high-magnesium calcite has been stabilized. It should be noted that Kindler and Hearty (1996) also provide cement abundance data for both eolianites, but this seems variable between units as the lower eolianite samples show more cement than the upper eolianite on the island of Bimini, while on Eleuthera the opposite is true. The amount of cement appears highly variable and not enough data is provided to accurately assess each unit on Eleuthera in terms of cement amount.

While the amount of cement precipitated appears to be influencing inorganic $\delta^{13}C$ and $\delta^{18}O$ isotope values, model data (table 2) also indicates differences in the isotopic composition of the precipitating low-magnesium calcite between units. For $\delta^{18}O$, the isotopic composition of the low-magnesium calcite decreases linearly from the top to the bottom of the measured section ($R^2 = 0.67$) with the upper eolianite having an average $\delta^{18}O_{LMC}$ of -4.34 ± 0.14 ‰ (1σ), the protosol having an average $\delta^{18}O_{LMC}$ of -3.36 ± 0.24 ‰ (1σ), and the lower eolianite having an average $\delta^{18}O_{LMC}$ of -2.50 ± 0.69 ‰ (1σ). While the reason for this is unknown, as the $\delta^{18}O_{LMC}$ is related to the ratio O_L/O_W (Allan and Matthews, 1982) discussed earlier, the differences may be associated with increases in this ratio down section, although, marine water should not have influenced the isotopic composition of the precipitating low-magnesium calcite. This is inconsistent with $\delta^{18}O$ traditionally seen as being invariable with depth (Allan and Matthews, 1982). The sample TP5, which is closest to the sequence boundary in the lower eolianite, shows the least negative $\delta^{18}O_{LMC}$ values. While this may be related to fractionation by evaporation at the sequence boundary, it is then curious that the sample below (TP4) shows the most negative $\delta^{18}O_{LMC}$ in the lower eolianite. Likewise, based on Allan and Matthews (1982), fractionation by evaporation (if present) should be present over a wider range (e.g. 1-2 m). More work would be needed to identify a more probable cause for these differences between units for $\delta^{18}O_{LMC}$ calculations. Interpretation may be influenced by original low-magnesium calcite in the samples.

$\delta^{13}C_{LMC}$ model data may be more easily explainable than $\delta^{18}O_{LMC}$, as $\delta^{13}C_{LMC}$ is heavily influenced by the presence of organic matter degradation and soil-gas CO_2 input. $\delta^{13}C_{LMC}$ values are highly variable, with the most negative values generally being calculated for protosol samples. This is expected as significant amounts of organic matter is expected in protosol samples with vegetative growth during its formation. The values in the upper eolianite are less negative than what is calculated for protosol samples (exception of TP11) as expected with less soil-gas CO_2 input to this unit. Interestingly, $\delta^{13}C_{LMC}$ values calculated for the lower eolianite (exception of TP4) are similar to what is measured for PC and GT samples in which authigenic carbonate precipitation, initiated from anaerobic respiration and sulfide formation (Higgins et al., 2009; Schrag et al., 2013; Moore et al., 2004; Ben-Yaakov, 1973), is expected to be producing lower bulk inorganic $\delta^{13}C$ through incorporation of isotopically light CO_2 from organic matter degradation and potentially anaerobic methane oxidation (Barker and Fritz, 1981; Moore et al., 2004; Drake et al., 2015; Cerling et al., 1991). Anaerobic respiration in the form of sulfate reduction by sulfate reducing bacteria produces negative $\delta^{34}S$ isotope fractionation (Habicht and Canfield, 1997; Detmers et al., 2001; Brunner and Bernasconi, 2005) and can be seen in PC and GT samples, among others. While input of authigenic carbonate to the lower eolianite cannot be ruled out, modern sediment samples with positive $\delta^{34}S$ fractionation have inorganic $\delta^{13}C$ closer to ~4 ‰ such that soil-gas CO_2 input into the lower eolianite may only have been able to fractionate $\delta^{13}C$ ~2 ‰ in the diagenetic low-magnesium calcite in this unit. The more negative $\delta^{13}C_{LMC}$ in the upper eolianite compared to the lower eolianite may be influenced by organic growth at the top of the unit seen in figure 2B, assuming this growth has been present for a significant period.

Another possibility that should not be discounted could be natural geochemical variability. Railsback et al. (2013) noted this phenomenon has potential to produce meteoric diagenetic signals in limestones, and as such, could be producing the more enriched signal at

the base of the TP section. However, this was directed toward lateral variability among horizons (e.g. variability in cement in the eolianites mentioned above). Being that the $\delta^{13}C$ and $\delta^{18}O$ isotope data and XRD data presented in the present study were collected along the same vertical line and are from powdered bulk rock samples, the data should accurately represent what has geologically occurred across the paleosol horizon on the vertical line. Whether or not the $\delta^{13}C$ and $\delta^{18}O$ data in this study produce similar results horizontally from our sampled location in the TP section is currently undeterminable and would require further study, however, the data do show that an isotope signature that is uncharacteristic of what has been traditionally described across an exposure surface is possible to produce with short term exposure surfaces. As well, it shows the production of at least some covariance between $\delta^{13}C$ and $\delta^{18}O$ data that most likely did not occur in the phreatic zone.

In terms of using inorganic $\delta^{13}C$ and $\delta^{18}O$ to identify cryptic sequence boundaries, the Two Pines section shows that the method may not preferable due to high variability in $\delta^{13}C$ and $\delta^{18}O$ related to either differences in cement precipitation or $\delta^{13}C$ and $\delta^{18}O$ of precipitating low-magnesium calcite. The lower eolianite and protosol were not exposed significantly long enough relative to the upper eolianite to produce geochemical signatures expected to be associated with a sequence boundary. Recognition of this signature in inorganic $\delta^{13}C$ data may potentially be inhibited by soil-gas CO_2 input from vegetation at the top of the upper eolianite as, although the samples from the upper eolianite should be less influenced by soil-gas CO_2, greater precipitation of cements appears to have been able to incorporate enough soil-gas CO_2 to produce similar bulk values to what is seen in the protosol. If the protosol had been exposed for a significantly longer amount of time before deposition resumed, a more traditional isotope signature may have been produced with lower inorganic $\delta^{13}C$ values recorded below the protosol. Although, this could also lead towards more pronounced soil development and therefore less similarity to a cryptic sequence boundary.

One may argue that the low $\delta^{13}C$ values in sample TP4 is the signature associated with the protosol, but this is difficult to say for certain given the current data from the roadcut. While sample TP4 does show lower $\delta^{13}C$ and $\delta^{13}C_{LMC}$ relative to surrounding samples, sample TP5 (closer to the protosol and sequence boundary), as well as TP1-TP3 do not show these low values which would be expected from soil-gas CO_2 input near the protosol. Sample TP11 shows a depletion in $\delta^{13}C$ and $\delta^{13}C_{LMC}$ relative to neighboring samples similar to TP4. As TP11 is not associated with the sequence boundary, this depletion could be related to more local differences in organic matter CO_2 input and a similar process may be affecting TP4.

Despite difficulties in interpreting the sequence boundary at the TP roadcut, the data do show that $\delta^{13}C$ and $\delta^{18}O$ produce distinctly different isotope signatures from unaltered sediments such that $\delta^{13}C$ and $\delta^{18}O$ can be used to identify zones in which meteoric diagenesis has occurred given enough time for the meteoric water to significantly stabilize the original minerals. Caution is advised for younger Pleistocene samples, especially those in environments prone to slow stabilization, as some data points (TP1, 2, 3, and 5; figure 11) show $\delta^{13}C$ and $\delta^{18}O$ values similar to some modern sediment samples (e.g. Darby island sample BD). Use of $\delta^{13}C$ and $\delta^{18}O$ to specifically identify cryptic sequence boundaries may be more useful in older limestones, such as the Ordovician limestones of Railsback et al. (2003), where longer subaerial exposure could occur to more greatly alter the exposure surface with less significant soil development due to lack of vascular plants. However, other techniques to identify meteoric

diagenesis should be used in conjunction to $\delta^{13}C$ and $\delta^{18}O$ data in order to be more certain that the chemical changes seen are indeed due to meteoric diagenesis.

5.3. REY Distributions and Changes with Diagenesis

5.3.1. Typical Seawater REY Distributions

Seawater possesses a typical REY distribution influenced by formation of complexes in solution as well as other oceanographic processes (e.g. scavenging). One major feature of oxic seawater REY distributions is HREE enrichment due to increasing affinity for HREEs to form complexes with carbonate ions, as opposed to LREEs which don't form as many carbonate complexes, and tend to be scavenged onto particulate matter (Byrne and Kim, 1990; Luo and Byrne, 2004; Muecke and Möller, 1988; Cantrell and Byrne, 1987, Elderfield, 1988; Alibo and Nozaki, 1999). However, in anoxic seawater, distribution typically exhibit less HREE enrichment (Bau et al., 1999; Byrne and Kim, 1990). Other major features of oxic seawater REY distributions is a positive La anomaly, negative Ce anomaly, positive Y anomaly, and positive Lu anomaly. Minor positive Gd and negative Tb anomalies may be seen as well. Anomalies in La, Gd, and Lu have been thought to either be associated to no, half, and full filling respectively of the 4f electron shell (e.g. De Baar et al., 1985) or by oceanographic processes (e.g. Alibo and Nozaki, 1999; Nozaki, 1997). In either case, positive La, Gd, and Lu are predicted by differences between scavenging and complexation (Bryne and Kim, 1990) and the La and Lu anomalies are readily visible in seawater and carbonate REE distributions (e.g. Bau et al., 1997; Nothdurft et al., 2004). Negative Ce anomalies are related to the tendency for Ce to exist as either as reduced Ce^{3+} or oxidized Ce^{4+}. In oxic waters, the negative Ce anomaly forms from oxidation and precipitation in Fe- and Mn- oxyhydroxides (Bau et al., 1997; Tostevin et al., 2016; Bau et al., 1996; Bau and Koschinsky, 2009; Palmer, 1985; Bau et al., 1999; Alibo and Nozaki, 1999) which can be released by dissolution in anoxic waters to form positive Ce anomalies (Tosetvin et al., 2016; Bau et al., 1997). The positive Y anomaly results from preferential scavenging of Ho compared to Y (Bau and Dulski, 1994). The positive anomaly may be decreased by release of Ho through dissolution of Fe- and Mn- oxyhydroxides in anoxic or acidic waters (Bau et al., 1997). Carbonates generally produce a seawater-like REY pattern from incorporation of REEs into the mineral structures (Zhong and Mucci, 1995; Nothdurft et al., 2004) but contamination may occur. Such contamination may arise from terrigenous siliciclastic input which can produce a flatter REY pattern and reduce Ce and La anomalies (Tostevin et al., 2016; Nothdurft et al., 2004). Likewise, input from Fe- and Mn- crusts may alter the distribution by inclusion of REEs associated with such crusts (e.g. Ce; Bau et al., 1996; Palmer, 1985).

Interference of BaO with Eu peaks in the ICP-MS measurements can create elevated Eu anomalies in REY distributions (Jarvis et al., 1989; Tostevin et al., 2016). This interference can be recognized as a linear correlation in a plot between Ba and Eu.

5.3.2. Contamination in TP and Sediment Samples

Sediment samples from SED-G1 display more flat REY distributions, atypical of carbonate sediments, which may be described by a couple process described in the previous

section. Specifically, Page Creek samples may be affected by terrigenous input or dissolution of Fe- and Mn- oxyhydroxides and desorption of REEs in a more anoxic environment. Samples GT and GH are likely not heavily affected by the effects of an anoxic environment, due to their depositional environment being one of a high energy beach environment. However, they may still be greatly affected by terrigenous input.

Plots of Y/Ho versus prevalent terrigenous elements (e.g. Fe, Al, etc.) have been used in the past (Tosetvin et al., 2016) to identify contamination from terrigenous input. These plots for TP and sediment samples (figures 17A and B) reveal SED-G1 to contain significant terrigenous input containing high amounts of Fe, Mn, and Al as seen by the linear correlation between Fe and Al as well as Mn and Al (figure 9A and B). As the Great Bahama Bank is an isolated carbonate platform, terrigenous input is low. The main source of this input has been determined to be Saharan dust and Mississippi River Valley Loess (Muhs et al., 2007; Swart et al., 2014) which is able to fertilize soils and aide in the production of terra rossa paleosols identified throughout Eleuthera (Hearty, 1998; Muhs et al., 2007). This dust input produces a flat REY distribution (figure 15) and would reduce the HREE enrichment seen in a typical seawater distribution preserved in carbonate sediments (as seen in the contaminated SED-G1 samples). Because the terrigenous contamination is not ubiquitous in the sediment samples, the source is not likely direct input of dust into the sediments. Another possible option is erosion of terra rossa paleosols into the SED-G2 sample localities which would provide a concentrated input of the terrigenous material.

$\delta^{34}S$ values in addition to positive linear correlations between $\delta^{34}S$ and organic $\delta^{13}C$ as well as $\delta^{34}S$ and inorganic $\delta^{13}C$ indicate anaerobic microbial processes, and in turn an anoxic environment, in SED-G1 samples which would alter the expected typical seawater REY distribution towards a flatter distribution. The sulfur isotope data themselves suggest an anoxic environment as seen by the negative $\delta^{34}S$ values in PC samples, GT, GH, and LC. This is because negative $\delta^{34}S$ values are associated with anaerobic sulfate reducing bacteria which fractionate sulfur in favor of light ^{33}S as opposed to ^{34}S (Habicht and Canfield, 1997; Detmers et al., 2001; Brunner and Bernasconi, 2005). This fractionation can theoretically produce a minimum $\delta^{34}S$ value of ~70 ‰ (Habicht and Canfield, 1997) and lower the $\delta^{34}S$ of the sedimentary organic material through sulfurization (Raven et al., 2016). The H_2S produced form sulfate reducing bacteria can also react with iron to produce highly negatively fractionated authigenic pyrite (Rickard and Morse, 2005; Drake et al., 2015) with model data (table 4) showing pyrite S dominating in PC, GT, and GH samples. The linear correlation between $\delta^{34}S$ and inorganic $\delta^{13}C$ is most likely related authigenic carbonate precipitation, especially in sample PCFM1 which has the lowest $\delta^{34}S$ and inorganic $\delta^{13}C$. Authigenic carbonate precipitation may be initiated in reducing porewaters in association with alkalinity increases resulting from anaerobic respiration (such as by sulfate reducing bacteria) and anaerobic methane oxidation (Higgins et al., 2009; Schrag et al., 2013; Moore et al., 2004) as well as pH increases associated with formation of sulfide minerals (Ben-Yaakov, 1973). Authigenic carbonates precipitated in this environment tend to have a depleted $\delta^{13}C$ related to input of light CO_2 via carbon isotope fractionation during anaerobic methane oxidation (Barker and Fritz, 1981; Moore et al., 2004; Drake et al., 2015) and respiration of organic material that may occur in the sediments (Cerling et al., 1991). This interplay between $\delta^{34}S$ and inorganic $\delta^{13}C$ can be seen by the more negative $\delta^{34}S$ and inorganic $\delta^{13}C$ of PC, GT, and GH samples (greatest pyrite S from model calculations in table 4)

compared to non-reducing sediment samples such as those form the Schooner Cays. However, the lack of a significant correlation between the two variables in SED-G1 appears to show that authigenic carbonate precipitation is may not prevalent enough heavily to dominate the inorganic $\delta^{13}C$ in the reducing sediments. It is important to note though that the sample with the most negative $\delta^{34}S$ and inorganic $\delta^{13}C$ (PFCM1) is the only sample to contain detectable pyrite in XRD (table 1) indicating pyrite precipitation likely significantly aided in authigenic carbonate precipitation in this sample.

The strong linear correlation between $\delta^{34}S$ and organic $\delta^{13}C$ in the SED-G1 samples (figure 13, table 8) appears to indicate changes in the abundance and type of organic matter input into the sediment locations. Previous work by Oehlert et al. (2012) measured $\delta^{13}C$ for platform and periplatform sedimentary organic matter (SOM) west of Andros on the Great Bahama Bank and found the average $\delta^{13}C$ value to be -12.2 ‰ for platform SOM and -15.4 ‰ for periplatform SOM. This difference was attributed to greater abundance of pelagic organic matter input into the periplatform sediments as opposed to platform derived organic matter. Oehlert et al. (2012) also directly measured $\delta^{13}C$ of Great Bahama Bank platform seagrasses and green algae and found green algae to have and average $\delta^{13}C$ value of -13.5 ‰ (range of -8.0 to -16.0 ‰) and sea grasses to have an average $\delta^{13}C$ of -6.4 ‰ (range of -4.2 ‰ to -8.7 ‰). The difference in platform SOM $\delta^{13}C$ values measured between the western Great Bahama Bank and this study may arise from a few sources: (1) greater input of pelagic organic matter as suggested for periplatform sediments on the western Great Bahama Bank (Oehlert et al., 2012); (2) greater abundance of isotopically lighter platform organic material; or (3) input of C_3 plant derived organic material from vegetation on Eleuthera, as C_3 plants are isotopically depleted ($\delta^{13}C \approx$ -28 ‰) as opposed to C_4 plants ($\delta^{13}C \approx$ -14 ‰; O'leary, 1988). In either case, the much more heavily depleted $\delta^{13}C$ values in many of the PC samples (up to -23.2 ‰) appear to indicate input of additional isotopically depleted organic matter in these samples. The most obvious source is mangrove leaf detritus, as mangrove vegetation is abundant in Page Creek (figure 2C) and produce $\delta^{13}C$ values of approximately -28.1 ‰ (Bouillon et al., 2008). If the organic $\delta^{13}C$ values in PC samples are taken as a proxy for mangrove detritus input in Page Creek, then the linear correlation between $\delta^{34}S$ and $\delta^{13}C$ indicates and greater prevalence of sulfate reduction in samples with greater mangrove detritus input. This appears to also indicate organic matter input, not sulfate availability, is the limiting factor in the abundance of sulfate reducing bacteria in PC samples as fractionation of $\delta^{34}S$ would not occur if sulfate was heavily limited. This could extend to samples GT, GH, and RC as all exhibit negative $\delta^{34}S$ values as well (indicating sulfate reducing bacteria) and also appear to strongly correlate to organic $\delta^{13}C$ (R^2 of SED-G1 + RC = 0.921). Sample RC was collected from a location with abundance mangrove vegetation similar to PC samples. However, the sample was taken in a location not immediately surrounded by mangrove vegetation, which appears to be shown in the organic $\delta^{13}C$ data by a more ^{13}C enriched value when compared to PC samples. Like in the PC samples, the lower amount of mangrove detritus input correlates to less sulfate reducing bacteria. While samples GT and GH were not taken near abundant mangrove vegetation like PC samples and RC, they still display a linear correlation indicated organic matter input is likely limiting sulfate reduction. Degradation of organic matter may also lead to reduced organic $\delta^{13}C$ values in sediments possibly due to selective degradation of proteins and carbohydrates enriched in $\delta^{13}C$ (Lehmann et al., 2002). While this process is likely happening in PC samples, this process has also likely

occurred in the other sediment samples and would not produce a great difference in values between the sediment samples.

Organic $\delta^{15}N$ data (figure 14) are also theoretically able to indicate an oxic or anoxic environment. This is because, in an oxic environment, ^{15}N enrichment or organic material often occurs due to preferential degradation of ^{14}N in the transformation of organic N to inorganic N (Craine et al., 2015; Lehmann et al., 2002). However, the released ^{15}N depleted inorganic nitrogen may be incorporated into bacterial biomass in anoxic sediments thereby creating a negative organic $\delta^{15}N$ fractionation in the organic matter preserved in the sediments (Lehmann et al., 2002). In figure 14, no significant difference between SED-G1 and SED-G2 are seen in terms of organic $\delta^{15}N$ values. It seems more appropriate to look at individual sample locations separately as the original $\delta^{15}N$ values of the organic matter before degradation may have been different, and fractionation from the oxic and anoxic processes mentioned above may not have been strong enough to produce a significant difference between locations. For example, while the correlation between $\delta^{34}S$ and organic $\delta^{15}N$ is weak for PC samples, the most reducing sample (PCFM1) has the most negative $\delta^{15}N$ and $\delta^{34}S$ values indicating some fractionation towards negative values is occurring likely from incorporation of light inorganic N into bacterial biomass.

U and Mo concentrations also indicate a reducing environment, specifically in Page Creek samples, which would alter the REY concentrations in these sediments. U and Mo concentrations are generally elevated in these samples relative to other samples. These elements may display increased concentrations in reducing and sulfidic sediments by sequestration into authigenic U and Mo phases as discussed and measured previously in modern Bahamian sediments by Romaniello et al. (2013, 2016). Therefore, the increased U and Mo concentrations in the Page Creek sediments, which are highly reducing and sulfidic given the highly negative $\delta^{34}S$ fractionation, are most likely due to authigenic U and Mo input in a reducing and sulfidic environment.

5.3.3. Effect of Diagenesis on REY Distributions in TP Samples

Because SED-G1 has been shown to contain terrigenous material and be a more reducing environment, which affected the REY distribution of this sample group, discussion of REY changes with diagenesis will mainly occur between TP and SED-G2 samples. As there are mineralogical changes in carbonates from unstable high magnesium calcite and aragonite to low magnesium calcite, it stands to reason that there might be distinguishable differences in REY distributions between meteorically altered carbonates and modern non-altered sediments due to this stabilization. Previous studies of carbonate diagenesis have found that original seawater REY distributions tend to be preserved in meteorically altered carbonates (Webb et al., 2009; Li and Jones, 2014, Liu et al., 2019). However, Webb et al. (2009) have also noted higher total REE concentrations, greater LREE depletion, and more negative Ce anomalies in diagenetic low-magnesium calcites. They attributed the higher total REE concentrations to additions from dissolution of overlying limestone, the more negative Ce anomalies to preferential oxidation of Ce released from dissolving aragonite over being incorporated into precipitating calcite, and preferential scavenging of LREEs released from dissolving aragonite onto organic matter. While the data presented in this study do not show greater total REY in TP

samples compared to sediment samples, they do show significantly greater HREE enrichment (table 6) and significantly more negative Ce anomalies (table 5). As well, the Ce anomalies become more negative with increasing calcite in TP samples (R^2 = 0.612, figure 18), a trend which is not seen in sediment samples (figure 18, table 8). When plotting aragonite versus Ce anomaly values (figure 18), a similar but positive correlation can be seen (R^2 = 0.595) can be seen with a much less significant correlation between the two parameters for sediment samples (table 7). This appears to indicate similar conclusions as formed by Webb et al. (2009) such that Ce which is leached during aragonite dissolution is not being re-incorporated into precipitating calcite. Interestingly, there is no similar significant correlation between HREE enrichment and calcite or aragonite for TP samples despite the greater HREE enrichment in the samples compared to sediment samples. One may also expect a difference in the Y/Ho ratio between TP and SED-G2 due to preferential scavenging of Ho on release from aragonite, however, this does not appear to be the case as Y/Ho ratios are not significantly different between the two groups.

As the average total REY (table 7) is lower and statistically different from SED-G1 samples, and total REY values for each TP sample is lower than what is seen in all modern sediment samples excluding those from the Schooner Cays, leaching of these REY may be associated with meteoric diagenesis. While Webb et al. (2009) showed enrichment in diagenetic calcite relative to parent aragonite, it is apparent that with bulk rock measurements the net effect of meteoric diagenesis may be leaching.

Table 9. REY data from the upper 200 m of the Clino core (n = 48; Liu et al., 2019) and TP samples. Raw REY data from Liu et al. (2019) was normalized by PAAS values of Pourmand et al. (2012) before calculation of Ce anomalies and HREE enrichment.

Sample group	Ce_{SN}/Ce_{SN}^* (± 1σ)	HREE enrichment (± 1σ)	Y/Ho (± 1σ)	Total REY (± 1σ)
TP	0.77 ± 0.14	4.27 ± 0.76	54.30 ± 7.73	1.88 ± 0.47
Clino (< 200 m)	0.64 ± 0.17	2.48 ± 0.77	40.02 ± 12.01	2.93 ± 1.79

The linear correlation between Ce anomalies and calcite appears to have potential for use as a geochemical proxy for identifying meteoric diagenesis, as the trend is distinct only to the TP samples and carbonates of great age (e.g. Devonian; Nothdurft et al., 2004) have been shown to retain typical seawater REY distributions. Although this trend may not as useful for identifying cryptic sequence boundaries, it presents usefulness as a starting point of identifying zones of meteoric diagenesis due to its distinctness to TP samples. Other possible geochemical proxies, such as greater HREE enrichment mentioned above, could then be used in conjunction with this to provide further evidence of meteoric diagenesis. Further studies would likely be necessary in order to fully assess the usefulness of this REY trend as a proxy for identifying meteoric diagenesis. For example, data from the meteorically altered zone of the Clino core taken from the Great Bahama Bank (upper 200 m; Liu et al., 2019; Hardisty et al., 2017) show much different values and trends than what is seen in the meteorically altered TP samples (table 9) with a significantly lower HREE enrichment and Y/Ho ratio in the Clino core as well as significantly lower total REY in the TP samples. Likewise, no linear correlation is present between Ce anomalies and low-magnesium calcite in the Clino core (R^2 = 0.03). Accurately

identifying the reason for these differences may require a more in-depth geochemical analysis of TP samples but may be related to influence of the marine environment in the Clino core as it is currently below sea-level.

5.4. Trace Element Changes with Diagenesis

5.4.1. Strontium

The use of Sr concentrations to help infer cryptic sequence boundaries in ancient limestone was suggested by Railsback et al. (2003) on the basis that Sr is leached from aragonite upon dissolution and is not reincorporated into the precipitating calcite cement. While this process is supported by the low (<< 1) distribution coefficient of Sr into calcite (Rimstidt et al., 1998) and other past studies have discussed Sr loss with meteoric diagenesis of limestones (e.g. Schroeder, 1969; Land, 1970; Budd and Land, 1990), the data presented in this study (figure 4) do not show a discernable difference in Sr concentrations between TP samples and sediment samples indicating that shifts in sediment sources to depositional centers could produce bulk Sr concentrations in unaltered limestones similar to what is seen in meteorically altered limestones. Likewise, the Sr concentrations in the protosol are the highest of all TP samples, which is unexpected based on the reasoning by Railsback et al. (2003).

One reason for the poor leaching of Sr at the TP section could lie in the openness of the system. Pingitore (1976; 1982) suggests that Sr can be more enriched in calcite cements precipitated in closed systems relative to open systems due to the inability of Sr to diffuse away from the reaction site in closed systems. This enrichment is noted to be possible in vadose environments which are more open due to what they call the “two-water system” (Pingitore, 1976). In the system, closed and open environments can exist in a vadose environment though the adhesion of water in small pore spaces and mass flow of water during rainfall respectively. Because rainfall is intermittent, a portion of the diagenesis will occur in the closed pore space micro-environments and lead to Sr enrichment in calcites precipitated there. Otherwise, poor Sr leaching may just be associated with poor aragonite stabilization.

Given that the TP section is so poorly cemented, it stands to reason that the original mineralogy of the sediments is playing a large role in the geochemical signature such that poor stabilization at the TP sampling location would not be enough to significantly alter the original Sr trend. As in the discussion of inorganic C and O isotopes, an assumption can be made that the upper eolianite originally had a greater high-magnesium calcite content than the lower eolianite based on the petrography of Kindler and Hearty (1996). Based on this, it can also be assumed that the original aragonite content of the upper eolianite was lower than that of the lower eolianite. This is because the main three mineral fractions of the carbonate sediments would have been aragonite, high-magnesium calcite, and low-magnesium calcite with aragonite and high-magnesium calcite being the main precipitated phases as low-magnesium calcite content is generally low for all sediment samples (figure 3). It could then be expected that the upper eolianite would have a lower average Sr content than the lower eolianite, given similar amounts of stabilization. This is the case as the upper eolianite has an average Sr content of 4155.50 ± 513.84 % while the lower eolianite has an average Sr content of 5142.07 ± 447.05 5

%. The protosol itself is the least stabilized (can be seen weathering out in figure 2A and B) with a Sr content of 5935.75 ± 257.63 % and the greatest aragonite content (table 1).

One could argue that the decrease in aragonite, and therefore Sr, below the protosol (samples TP5 and TP4) could be the effect of increased stabilization near the exposure surface as in Railsback et al. (2003). While this may be the case, I would argue this diagnostic to the sequence boundary at the TP roadcut. One can already see how the original mineralogy may be affecting the Sr concentrations as the younger (upper) eolianite has lower average Sr than the protosol below it which began forming at least ~5,000 years before the upper eolianite (Neumann and Hearty, 1996). Such a shift is possible from sediment source shifts based on the large aragonite content differences between sediment samples in XRD (figure 3). Likewise, a similar magnitude shift can be seen between samples TP11 and TP10 (figure 4). This shows a relatively large increase across a small interval indicating the decrease between TP6 and TP5 may be due to a similar reason which is not associated with the exposure surface. Other evidence for such rapid changes in Sr can be seen in the data from Railsback et al. (2003). In their paper, their data shows large decreases in Sr concentrations not associated with either an actual sequence boundary or an inferred sequence boundary. In some cases, their data shows Sr decreases not associated with an actual or inferred sequence boundary that are even greater than what is seen associated with actual or inferred sequence boundaries. Therefore, vadose meteoric stabilization does not appear to produce a diagnostic magnitude shift in Sr that could *confidently* be associated with a cryptic sequence boundary.

5.4.2. Uranium

Uranium behaves like strontium in that it is preferentially incorporated into aragonite over calcite (Reeder et al., 2000) and is depleted in diagenetic calcite relative to the parent aragonite (Chen et al., 2018). The lack of depletion of U in TP samples relative to modern sediment samples (figure 7) is also like what is seen in Sr concentrations, likely related to their similar behaviour in carbonate mineral incorporation. Similar to Sr concentrations, U concentrations in TP samples experience a peak in the protosol and decrease below it, although the trend in U concentrations is much more gradual. Given that U concentrations have been noted to be lower in diagenetic calcite compared to parent aragonite (Chen et al., 2018), the lack of depletion relative to sediment samples is attributed to the poor stabilization at the TP section easily seen by the poor cementation at the TP section. It appears, therefore, that elements preferentially associated with aragonite will not experience significant leaching in bulk rock geochemistry values upon meteoric stabilization in carbonate lithologies dominated by aragonite which is poorly stabilized. U concentrations also do not appear suitable for identification of a cryptic sequence boundary given that the gradual U concentration changes appear to be more associated with original mineralogy as opposed to diagenetic stabilization, similar to Sr.

5.4.2. Sulfur

Sulfur concentrations in the TP samples has been shown to be significantly depleted relative to S concentrations in the sediment analogue samples. This shows vadose meteoric

diagenesis has a significant role in the leaching of sulfur. In modern marine carbonate sediments, carbonate associated sulfate (CAS) will dominantly contribute to the S concentrations of these sediments (Staudt and Schoonen, 1995) with seawater sulfate replacing CO_3^{2-} in the carbonate mineral structure (Pingitore et al., 1995). With meteoric diagenesis, carbonates have been shown to contain depleted CAS after stabilization has occurred (Gill et al., 2008). As such, leaching of CAS upon meteoric diagenetic stabilization may be the main source of S loss in the TP samples.

Another source of S leaching may be from rapid oxidation of sulfides, such as pyrite, upon subaerial exposure (Johnson and Hallberg, 2005; Baars and Horak, 2018; Howie, 1979; Hecht and Kölling, 2002), and significant amounts of sulfide associated S are expected in the sedimentary environments showing negative $\delta^{34}S$ fractionation. However, this would not be a dominant process as S concentrations in the least reducing samples (e.g. from the Schooner Cays) are higher than S concentrations in the TP samples. In other words, the samples in this study from the Schooner Cays are not conducive to sulfide precipitation due to a lack of available organic material (no overlying seagrass), a probable lack of Fe (due to being on an isolated carbonate platform), and a lack of sulfate reduction as supported by the positive fractionation of sulfur isotopes (figure 13), all which are needed for sulfide mineral precipitation (Berner, 1970; Morse, 1999; Du Laing et al., 2008; Kraal et al., 2013). As the Schooner Cays likely have insignificant amounts of sulfide precipitates and have greater S concentrations than TP samples, sulfide precipitation which would impart higher S concentrations in the sediments (e.g. sample PCFM1) is not necessary to record S leaching in meteorically altered limestones. However, presence of significant amounts of sulfides in the original sediment is not hypothesized to impact the recording of S leaching, as these sulfides should degrade much faster than aragonite and high-magnesium calcite can stabilize to incorporate the leached S. Organic S will also be affecting S concentrations in TP samples, and while this is quantifiable for sediment samples in this study with the provided model (table 4), the lack of $\delta^{34}S$ data for TP samples inhibits calculations for these samples. More work would be needed to quantify this and further discuss the influence of organic S in TP samples.

While bulk S concentrations may prove useful as a proxy for identifying meteoric diagenesis in limestones, especially in the case of poorly stabilized limestones such as the TP section, care should be taken to identify the loss of S is indeed due to meteoric diagenesis. For example, loss of CAS has also been associated with burial and low-grade metamorphism (Fichtner et al., 2017) with greater CAS loss at higher temperatures. Other examples include lower CAS which may be associated with carbonate precipitation in reducing environments with low sulfate and deep-sea carbonates have been noted to have lower CAS (Staudt and Schoonen, 1995).

In terms of Identifying cryptic sequence boundaries, S does not appear to be useful based on TP samples. While there is a decrease in S of ~180 ppm across the base of the protosol, similar shifts of ~125 ppm occur in the two eolianites (between samples TP12 and TP11 as well as TP4 and TP3) and the greatest negative shift of ~405 ppm occurs well above the protosol between samples TP13 and TP12. This indicates that short term exposure did not cause a distinctive S shift in the TP samples that can be attributed to such exposure.

5.4.3 Magnesium

The distribution coefficient of Mg in calcite is < 1 (Rimstidt et al., 1998) and therefore is expected to not be preferentially incorporated into precipitated meteoric low-magnesium calcite cement. While Mg enrichment has been noted in meteorically altered aragonite corals (e.g. Pingitore, 1976; Pingitore 1978), it should be noted that this Mg enrichment, where the Mg is sourced from surrounding high-magnesium calcite sediments, is discussed in terms of altered and unaltered coral samples and not bulk sediments as in in this study.

Lower Mg concentrations were measured in TP samples relative to all sediment samples except for Schooner Cays samples. While the Schooner Cays is likely a close approximation to the TP eolianites, as the eolianites have a large ooid component, the likelihood is that sediments which compose the eolianites have additional sources of sediments which would have higher Mg concentrations as indicated by the higher Mg concentrations in the sediment samples outside of the Schooner Cays. Therefore, it can be assumed that the Mg concentrations of the TP eolianites before stabilization were greater than that of the Schooner Cays samples, although it may not have been much greater based on the small range of Mg concentrations for most sediment samples. While Mg certainly was lost during the transition from high-magnesium calcite to low-magnesium calcite, the depletion was not great enough to lower the Mg concentration of the TP samples below that of the Schooner Cays samples. This shows that, within a specific environment, shifts of sediment source have the potential to produce Mg concentrations like what is produced from meteoric diagenesis.

The reason that Mg is not distinctively depleted relative to all modern sediment samples likely stems from Mg incorporation into diagenetic calcite precipitated from stabilizing aragonite. Like how Pingitore (1976) and Pingitore (1978) found stabilized corals to have greater Mg relative to parent aragonite corals from incorporation of Mg sourced from surrounding dissolving high-magnesium calcite sediments, calcite cements from stabilized aragonite grains may be enriched in Mg relative to their parent grains. Therefore, while Mg concentrations do appear to record meteoric diagenesis in the TP samples, it would likely be less reliable than elemental concentrations which show more distinctive depletion in TP samples relative to sediment samples.

In terms of identifying cryptic sequence boundaries, Mg does not appear to be useful based on Mg concentrations in the TP section. Instead, Mg concentrations may more indicative of original mineralogy in these samples. One may argue that the large increase in Mg concentration across the base of the protosol (~0.2 %) is due to greater stabilization within the protosol leading to more Mg leaching. However, the protosol is the least cemented portion of the TP roadcut (seen weathering out, figure 2A and B) and therefore may have had a lower high-magnesium calcite content before diagenesis relative to the surrounding eolianites, similar to the reasoning given for the $\delta^{18}O$ differences between the two eolianites in which greater high-magnesium calcite in the upper eolianite may have allowed for more cement precipitation and a lower average $\delta^{18}O$. This is because high-magnesium calcite is more soluble than aragonite in freshwater (Chave et al., 1962) and therefore a limestone with greater amounts of parent high-magnesium calcite may be expected to be more heavily cemented than a limestone with lower amounts after meteoric diagenesis (Husseini and Matthews, 1972).

5.4.4. Zinc, Copper, and Chromium

Zn shows distinctive depletion in the TP samples relative to all modern sediment samples while Cu and Cr are depleted relative to the majority of modern sediment samples (exception of PCFM1 and Schooner Cays samples for Cu and Cr respectively) which yields the possibility of the use of these elements for identifying meteoric diagenesis. Distribution coefficients for Cu and Zn in calcite have been determined to be greater than 1 (Rimstidt et al., 1998) and previous studies have suggested enrichment or no change in Zn concentrations between aragonite and diagenetic calcite (Pingitore, 1978; Pingitore, 1982). However, these studies mainly discuss changes between aragonitic corals and the daughter low-magnesium calcite and not bulk rock changes such as what is measured at the TP section in this study. Therefore, on a bulk rock scale, these elements may be expected to be leached in a meteoric diagenetic environment. Similar to how sulfide formation in original sediments was suggested not to affect the record of meteoric diagenesis in S concentrations due to relatively rapid oxidation of sulfide minerals upon exposure (Johnson and Hallberg, 2005; Baars and Horak, 2018; Howie, 1979; Hecht and Kölling, 2002), the same may be expected for Zn and Cu which are commonly incorporated into sulfide minerals in a reducing environment (Cavalazzi et al., 2014).

In terms of using these elemental concentrations for identification of a cryptic sequence boundary, these elements do not appear applicable based on the data from the TP section. In other words, there are no geochemical changes within or near the protosol for these elements which are not seen in similar magnitudes between other TP samples in the eolianites above and below the protosol.

5.4.5. Cobalt

Co is the only element which shows distinctive enrichment in the TP samples relative to modern sediment samples, leading to potential use of this element of identifying meteoric diagenesis. As this element is enriched by a minimum of ~4 times what is seen in the sediment sample with the most Co (PFCM1), an outside source of chromium is suggested for the enrichment in the TP samples. The most obvious source of this enrichment would be atmospheric dust (Swart et al., 2014; Muhs et al., 2007), but mineral phase determination of Co in these samples, either by a sequential extraction or some other method, would be needed to accurately determine the source of the enrichment.

Based on the data presented for Co in the TP section, Co appears highly variable and may not be useful for identifying cryptic sequence boundaries. Co values and trends within the protosol are not distinctive to the protosol itself. Likewise, the large Co peak in sample TP4 is suggested not to be associated with the sequence boundary as no such peak occurs in sample TP5 which is directly below the protosol. If the peak in TP4 was associated with the sequence boundary, then a similar trend would be expected across the boundary between sample TP6 and TP5. As such, the peak in TP4 may be similar (in the method of production of the peak) to the smaller peaks seen in sample TP10.

5.4.6. Remaining elements

The remaining elements not mentioned above do not appear to show significant differences in the TP samples relative to modern sediment samples. As such, they are not suggested to have potential for identifying meteoric diagenesis or cryptic sequence boundaries with bulk geochemistry, as similar elemental concentration values seen in the altered TP samples have the potential to be produced in the variety of measured sedimentary environments in this study. The reason for this is likely that these elements have a majority concentration in stable phases which were not highly altered during meteoric diagenesis. More work would need to be done to confirm this.

6. SUGGESTIONS FOR FUTURE WORK

While bulk rock leaching of S, Zn, Cu, Cr, REY, and enrichment of Co have been identified as potential proxies for meteoric diagenesis, it is important to understand what mineral phases these elements are associated with in the modern carbonate sediments and diagenetic sections to better understand the processes occurring leading to leaching and better evaluate the use of these elements as a proxy. Specifically, sequential leaching procedures have been used in the past to determine mineral phase associations of different elements (e.g. Bau and Koschinsky, 2009) and may be useful to understand the different mineral associations of elements in the modern Bahamian sediments. Another suggestion may be elemental concentration characterization of the main three carbonate phases (i.e. aragonite, high-magnesium calcite, and low-magnesium calcite) in different carbonate environments.

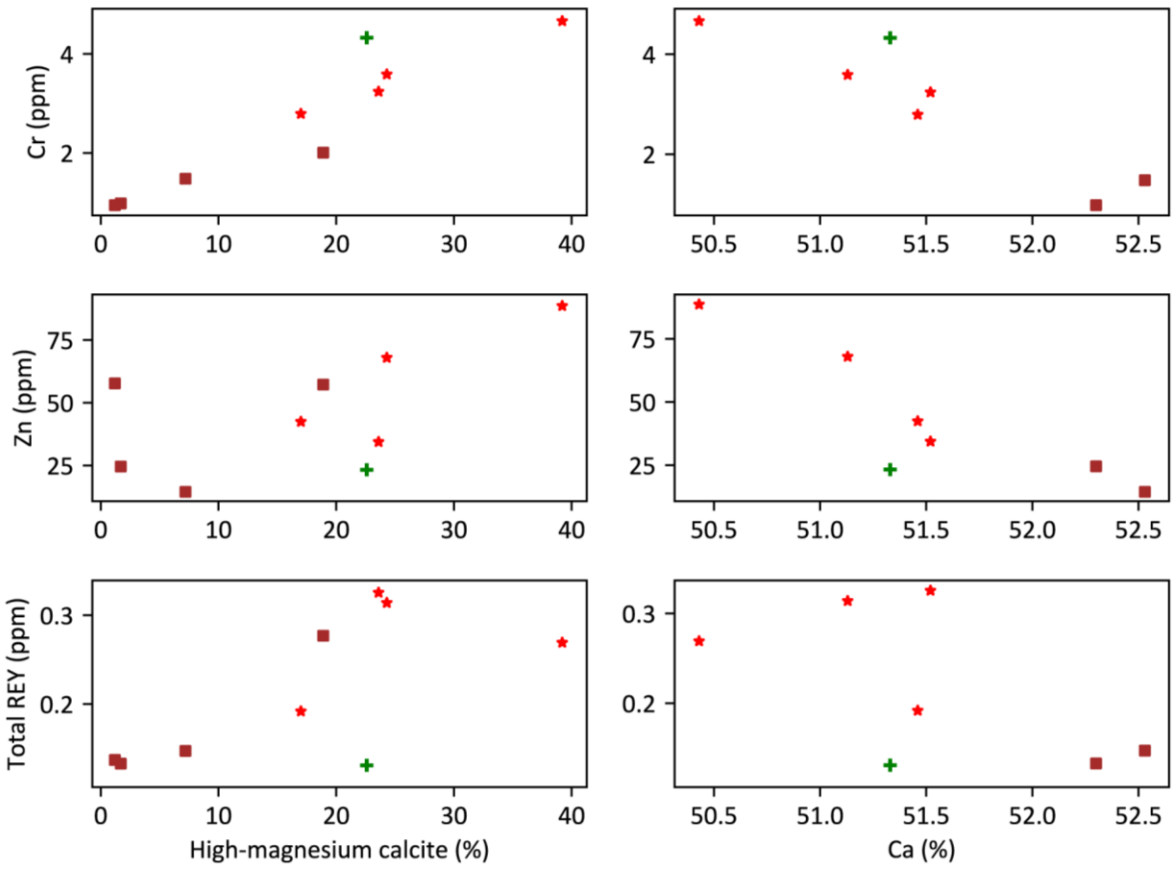

Figure 19. Cross plots of Cr, Zn and total REY versus high-magnesium calcite and Ca for modern sediments with $\delta^{34}S > 0$. Data point symbols follow the scheme for figure 1.

For example, in the least reducing modern sediments sampled in this study (here classified as $\delta^{34}S > 0$), as expected, Mg possess a positive linear correlation with high-magnesium calcite ($R^2 = 0.99$) and a strong negative correlation with Ca ($R^2 = 0.89$) as Mg. Interestingly, Cr, Zn, and REY display a similar trend in the least reducing sediments (figure 19), and this trend is much more weak or absent in the most reducing sediments (here classified as $\delta^{34}S < 0$) for Cr and Zn.

Likewise, the negative correlation between these elements and Ca is absent in the TP samples. These trends are not present for elements which are not leached in the TP section. This suggests that preferential incorporation of the leached elements into high-magnesium carbonate may be leading to preferential leaching in the TP section. However, it is impossible to accurately determine if this is the case without further work. Other possibilities for leaching of these elements include incorporation into labile phases which degrade much more quickly than precipitating diagenetic calcite can incorporate the elements. For example, Cr^{3+} is oxidized to soluble Cr^{6+} in the presence of Mn bearing minerals (Bartlett and James, 1976; Oze et al., 2007) and may also explain leaching in the TP section.

Other options for future work would be to characterize other meteoric diagenetic sections with the proxies discussed in this study to determine if these trends can be observed consistently. Sr and U concentrations may be of interest to study in limestones which experienced greater meteoric diagenetic stabilization than the TP sections, as these elements may show more significant leaching in this case. However, it would be important to identify any potential contamination of the REY signature or other events which may have altered the geochemical signature of the limestones aside from meteoric diagenesis.

7. CONCLUSIONS

Analysis of inorganic $\delta^{13}C$ and $\delta^{18}O$ isotopes, REY, trace elements, and mineralogy on the Pleistocene meteorically altered Two Pines section and surrounding modern sediments showed a variety of previously unused geochemical proxies may be useful for identifying meteoric diagenesis, even in poorly stabilized limestones. While $\delta^{13}C$ and $\delta^{18}O$ has been previously discussed as a useful proxy for meteoric diagenesis, this study re-confirms lowering of $\delta^{13}C$ and $\delta^{18}O$ with meteoric diagenesis. However, similar values in the meteorically altered section were seen in modern Bahamian sediments, therefore some caution may be advised in younger or poorly altered samples. Mineral stabilization from high-magnesium calcite and aragonite to low-magnesium calcite with meteoric diagenesis has also been extensively studied, and this study shows similar results with complete stabilization of high-magnesium calcite and partial stabilization of aragonite to low-magnesium calcite with meteoric diagenesis. The previously relatively unstudied proxies for meteoric diagenesis identified in this study include the following: (1) a negative linear correlation between Ce anomaly and calcite content; (2) enhanced HREE enrichment; (3) enhanced total REY depletion; (4) S, Zn, Cu, and Cr leaching; and (5) Co enrichment. The negative linear correlation between Ce anomalies and calcite content, S concentrations, Zn concentrations, and Co concentrations appear to have the most potential as these are the potential proxies most significantly different from modern sediment samples. Cu and Cr show similarities to only to a miniscule amount of modern sediment samples and, while great potential as a proxy still exists, it may be to a lesser degree than those mentioned above. Mg is like Cu and Cr in that only a few modern sediment samples possess similar Mg values to what is measure in the TP section. Mg loss from the stabilization of high-magnesium calcite has been extensively previously studied, and the Two Pines section re-confirms this through leaching of Mg from the samples.

In contrast to the inferences made by Railsback et al. (2003), Sr does not appear to accurately be able to record short term exposure associated with cryptic sequence boundaries. In fact, it appears significantly less useful than other proxies discussed in this study.

While these proxies appear to have use in identifying meteoric diagenesis, they do not appear to have potential for identifying cryptic sequence boundaries. Instead, geochemical trends within the Two Pines section may be remnant of the original mineralogy such that a short time of formation for the protosol was not enough to significantly alter the sediments relative to the surrounding eolianites. Identification of cryptic sequence boundaries with geochemical proxies may have more potential in locations or time periods (e.g. Ordovician) where visually identifiable soil development may be greatly reduced or take a significantly longer time frame to develop than the sampled protosol in this study.

APPENDIX A. REY DATA

A.1. REY concentrations for TP and sediment samples. Concentrations are in ppm.

Sample	Element Concentration							
	La	Ce	Pr	Nd	Sm	Eu	Gd	Tb
TP 1	0.07835	0.12472	0.02290	0.10620	0.03027	0.01251	0.02680	0.00921
TP 2	0.06425	0.07800	0.01625	0.07598	0.01958	0.01098	0.02060	0.00800
TP 3	0.08233	0.09197	0.01795	0.08627	0.02269	0.01475	0.02398	0.00888
TP 4	0.14690	0.23702	0.03614	0.15949	0.04223	0.01800	0.04108	0.01304
TP 5	0.07918	0.10375	0.02014	0.09541	0.02556	0.01357	0.02500	0.01006
TP 6	0.18110	0.27063	0.04386	0.20474	0.05340	0.02068	0.05289	0.01801
TP 7	0.21274	0.35486	0.05450	0.25224	0.06161	0.02331	0.06164	0.02038
TP 8	0.19324	0.29872	0.04817	0.22978	0.05340	0.02085	0.05649	0.01860
TP 9	0.14181	0.19064	0.03445	0.17117	0.04548	0.01923	0.04456	0.01579
TP 10	0.13540	0.16494	0.03254	0.15372	0.04095	0.01748	0.04151	0.01523
TP 11	0.12359	0.15566	0.03260	0.14493	0.04023	0.01801	0.03975	0.01611
TP 12	0.11410	0.13834	0.02993	0.13130	0.03498	0.01592	0.03665	0.01501
TP 13	0.13361	0.18977	0.04676	0.16678	0.05023	0.03041	0.05264	0.02719
PCFM1	4.687	9.5897	1.1174	4.3771	0.8713	0.1928	0.9774	0.2186
PCFM 3 1/2	2.6608	5.1347	0.5904	2.3883	0.4541	0.103	0.5179	0.1127
PCFM 3 2/2	2.3223	4.7026	0.5226	2.0988	0.4056	0.0911	0.4586	0.0997
PCM3A	1.6264	3.3805	0.3792	1.4987	0.3019	0.07	0.3375	0.0767
PCM3	1.9232	3.9774	0.4344	1.7771	0.3464	0.0811	0.3885	0.0884
PCM4	1.7282	3.4905	0.3846	1.5414	0.3056	0.0716	0.3417	0.0766
PCBM	1.8646	3.718	0.4142	1.6616	0.3113	0.0744	0.3592	0.0786
SCPO	0.1525	0.2312	0.0348	0.1646	0.0414	0.02	0.0416	0.0142
SCOS	0.1603	0.2262	0.0365	0.1716	0.0408	0.0197	0.0446	0.015
SCNO	0.1881	0.2799	0.0435	0.1988	0.0461	0.0219	0.0493	0.0159
SCNS	0.1453	0.2151	0.0328	0.155	0.0399	0.018	0.0413	0.0136
BO1	0.4584	0.5528	0.101	0.4855	0.1051	0.0375	0.1138	0.0365
BD	0.3062	0.4181	0.0681	0.3209	0.0715	0.0263	0.0728	0.0221
PB	0.48	0.5552	0.1096	0.5213	0.1238	0.0412	0.1245	0.0395
RC	0.501	0.841	0.11	0.483	0.098	0.0339	0.1103	0.0309
LC	0.5003	0.8585	0.1153	0.4886	0.0997	0.0323	0.1121	0.0295
GT	1.2302	2.4383	0.288	1.2015	0.2412	0.06	0.2682	0.0642
GH	2.4404	4.3162	0.5423	2.2522	0.4354	0.105	0.4938	0.118
EL	0.3872	0.4348	0.0834	0.4018	0.0918	0.0329	0.0964	0.0304

(table cont'd)

Sample	Element Concentration						
	Dy	Y	Ho	Er	Tm	Yb	Lu
TP 1	0.05032	0.77996	0.01259	0.04399	0.00588	0.03514	0.00562
TP 2	0.04649	0.77101	0.01258	0.04294	0.00602	0.03302	0.00541
TP 3	0.05180	0.84425	0.01416	0.04840	0.00675	0.03743	0.00631
TP 4	0.06301	0.96142	0.01650	0.05616	0.00747	0.04365	0.00735
TP 5	0.05430	0.89990	0.01469	0.05076	0.00707	0.03998	0.00655
TP 6	0.09707	1.32583	0.02365	0.08017	0.01084	0.06227	0.00984
TP 7	0.10142	1.37145	0.02494	0.08489	0.01136	0.06363	0.01058
TP 8	0.09254	1.25981	0.02334	0.07784	0.01094	0.06116	0.01005
TP 9	0.08267	1.10924	0.02126	0.07129	0.00998	0.05479	0.00918
TP 10	0.08149	1.14960	0.02146	0.06989	0.01020	0.05623	0.00978
TP 11	0.07530	1.02624	0.02105	0.06408	0.01115	0.05240	0.01036
TP 12	0.06942	0.99636	0.01941	0.06039	0.01005	0.04705	0.00975
TP 13	0.08501	0.98719	0.03022	0.07443	0.02103	0.06060	0.01954
PCFM1	0.7246	5.3296	0.1501	0.5756	0.0577	0.3942	0.058
PCFM 3 1/2	0.3557	2.7344	0.0726	0.2812	0.0266	0.1825	0.0268
PCFM 3 2/2	0.3118	2.4656	0.0648	0.2539	0.0243	0.1592	0.0242
PCM3A	0.2523	1.9733	0.0511	0.1976	0.0191	0.1289	0.0194
PCM3	0.2895	2.3548	0.059	0.2255	0.0218	0.1453	0.0214
PCM4	0.2547	2.0632	0.0518	0.1985	0.0194	0.1268	0.019
PCBM	0.25	2.0519	0.0504	0.1992	0.0187	0.1206	0.0183
SCPO	0.0764	1.0696	0.0192	0.0644	0.0082	0.0466	0.0074
SCOS	0.0784	1.1065	0.0199	0.067	0.0086	0.0509	0.008
SCNO	0.0819	1.1203	0.0205	0.071	0.0089	0.053	0.0081
SCNS	0.0771	1.0799	0.0189	0.0647	0.0083	0.047	0.0073
BO1	0.1917	2.2865	0.0455	0.151	0.0181	0.11	0.0169
BD	0.1068	1.2793	0.0248	0.0838	0.0097	0.0572	0.009
PB	0.2024	2.3268	0.0479	0.1598	0.019	0.1145	0.0169
RC	0.136	1.5658	0.0316	0.1086	0.0125	0.0782	0.0124
LC	0.126	1.4829	0.0286	0.102	0.0113	0.0714	0.011
GT	0.2427	2.282	0.0526	0.193	0.0194	0.1245	0.0183
GH	0.4326	3.8485	0.0902	0.3307	0.0319	0.2053	0.0295
EL	0.1633	2.0135	0.0402	0.1329	0.0162	0.0976	0.015

APPENDIX B. ICP-MS DATA

B.1. ICP-MS elemental concentrations for TP and sediment samples. Concentrations are in ppm.

Sample	Element Concentration					
	Al	Sc	V	Cr	Mn	^{57}Fe
TP 1	114.90683	0.17273	0.88645	1.16150	0.80527	109.91712
TP 2	45.01571	0.16771	0.82462	0.65904	0.26192	87.71218
TP 3	64.29798	0.18858	1.03404	1.17471	0.31392	93.06250
TP 4	267.04508	0.36980	1.37237	1.56006	1.83057	185.89874
TP 5	69.52112	0.27008	1.06872	1.15799	0.48108	106.48238
TP 6	186.85101	0.35275	1.19973	0.94768	2.29226	127.80354
TP 7	185.44308	0.39890	1.28266	1.04250	3.97859	144.34661
TP 8	149.47150	0.37632	1.23768	0.77669	3.18205	129.52525
TP 9	77.40490	0.34626	1.10286	1.06451	1.74937	121.59038
TP 10	192.97747	0.44423	1.00503	1.14060	0.84723	114.43054
TP 11	335.34734	0.48730	1.29912	1.29552	0.60599	109.56498
TP 12	44.08036	0.33913	0.84256	1.28453	0.96905	107.43670
TP 13	110.36446	0.46493	1.24070	1.32186	0.76880	123.72867
PCFM1	4422.4	0.5586	16.28	13.425	23.635	1170
PCFM 3 1/2	1408.2	0.2933	11.777	5.7109	11.686	674.88
PCFM 3 2/2	1068.3	0.2918	8.6845	4.9129	12.28	546.33
PCM3A	955.16	0.1198	5.8866	4.2974	9.0582	483.02
PCM3	1022.8	0.1528	7.3748	5.543	9.7279	528.35
PCM4	633.73	0.2524	5.0839	4.1534	7.8908	356.13
PCBM	703.61	0.2802	11.056	4.6633	7.8631	388.13
SCPO	131.45	0.1273	1.1706	0.9444	1.2661	94.984
SCOS	79.55	0.1884	1.3164	1.4795	0.8077	104.37
SCNO	115.95	0.2157	1.2769	2.0063	2.6878	127.23
SCNS	89.297	0.1653	1.036	0.9799	0.4051	90.374
BO1	97.165	0.1796	1.2612	3.589	3.064	104.52
BD	126.39	0.1369	1.8134	2.7918	1.2692	98.21
PB	99.942	0.1238	1.2099	3.2398	2.8387	99.983
RC	309.98	0.225	2.375	4.329	4.7426	173.67
LC	190.32	0.1877	1.7638	3.7598	2.8072	132.11
GT	214.35	0.2073	3.0415	6.4129	4.4157	275.27
GH	359.03	0.2049	3.7017	10.826	5.3738	275.14
EL	78.31	0.0931	1.2971	4.6652	5.4705	88.173

(table cont'd)

Sample	Element Concentration					
	Co	Ni	Cu	Zn	Rb	^{95}Mo
TP 1	3.53767	1.61268	1.01885	3.14528	0.29029	0.07677
TP 2	2.13441	1.30463	0.34644	1.39483	0.12895	0.07167
TP 3	6.90350	1.56321	0.13243	4.70012	0.14905	0.09478
TP 4	14.68925	1.95970	0.53315	6.18805	0.40093	0.12404
TP 5	2.53723	1.53301	0.29873	3.11677	0.22238	0.09350
TP 6	4.90092	2.45025	0.21325	2.28350	0.27968	0.09308
TP 7	2.51219	1.92405	0.26490	2.62324	0.31828	0.09271
TP 8	1.73282	1.79539	0.22821	2.28953	0.35177	0.10032
TP 9	3.46434	1.68192	0.43672	3.12073	0.36642	0.09243
TP 10	7.99353	1.64327	0.33194	2.52973	0.35899	0.08872
TP 11	4.42118	1.66808	0.43309	3.58882	0.59068	0.13020
TP 12	3.97190	1.56766	0.40604	3.18013	0.62741	0.09935
TP 13	6.21188	1.73650	1.09109	5.60535	2.39151	0.24689
PCFM1	0.4218	2.5269	0.5359	25.004	0.6338	2.7262
PCFM 3 1/2	0.4245	2.0449	1.4602	45.282	0.3123	2.4683
PCFM 3 2/2	0.3553	1.7292	1.9515	32.737	0.3542	2.3005
PCM3A	0.2978	1.5601	1.5314	31.108	0.407	0.7231
PCM3	0.4011	1.8481	1.6976	52.46	0.4169	1.0049
PCM4	0.2907	1.6082	1.8976	23.736	0.2385	0.6622
PCBM	0.3699	2.0727	1.6511	62.801	0.2617	1.0581
SCPO	0.2993	1.596	3.6563	57.701	0.1528	0.1284
SCOS	0.2573	6.9882	2.1615	14.478	0.1465	0.3424
SCNO	0.3101	1.5828	5.6182	57.23	0.1462	0.1582
SCNS	0.3075	1.1708	2.8456	24.555	0.1354	0.1021
BO1	0.3359	1.4909	2.4304	67.954	0.1452	0.1449
BD	0.3692	1.268	3.0231	42.433	0.1842	0.1322
PB	0.3437	1.3534	2.2012	34.395	0.1603	0.1418
RC	0.3332	1.5658	2.4828	23.28	0.3845	0.5883
LC	0.3519	1.3177	1.7192	39.849	0.1548	0.1063
GT	0.3209	1.4289	3.9858	25.991	0.1942	0.2921
GH	0.3302	1.5104	3.0565	30.834	0.1678	0.2307
EL	0.2788	1.6942	1.7116	88.6	0.1247	0.1473

(table cont'd)

Sample	Element Concentration				
	Cd	Ba	Ti	Th	U
TP 1	0.04597	8.10767	0.17488	0.11177	2.98594
TP 2	0.04321	8.89490	0.18358	0.09764	3.48876
TP 3	0.05521	13.03439	0.23431	0.12573	3.62834
TP 4	0.05398	12.04012	0.20714	0.15318	3.20380
TP 5	0.05049	9.75116	0.20919	0.13176	3.52537
TP 6	0.06174	10.77292	0.19857	0.15373	4.22255
TP 7	0.05050	11.62327	0.21154	0.17003	5.11369
TP 8	0.04961	9.57937	0.22877	0.18904	4.52745
TP 9	0.05147	10.40520	0.21160	0.17674	4.12999
TP 10	0.06954	8.37142	0.18015	0.20928	3.66019
TP 11	0.10062	7.95749	0.26671	0.45586	2.77193
TP 12	0.04410	6.87644	0.19426	0.31466	2.35271
TP 13	0.08074	9.47776	0.44634	1.31960	2.25080
PCFM1	0.0873	8.6561	0.251	0.68	7.5097
PCFM 3 1/2	0.078	11.204	0.2519	0.3502	5.3271
PCFM 3 2/2	0.0762	11.897	0.2724	0.426	4.6985
PCM3A	0.0646	10.406	0.222	0.1742	2.6283
PCM3	0.0784	12.467	0.2636	0.2023	3.2123
PCM4	0.0662	12.68	0.247	0.2906	3.218
PCBM	0.0749	12.21	0.2643	0.329	4.5308
SCPO	0.0691	15.107	0.2485	0.1365	3.8542
SCOS	0.0623	12.943	0.2186	0.1238	4.0034
SCNO	0.0664	15.631	0.2295	0.1202	3.8817
SCNS	0.0569	13.229	0.2258	0.1174	4.1271
BO1	0.0688	13.687	0.2396	0.1339	3.4707
BD	0.1322	0.0681	14.493	0.2237	0.1137
PB	0.0666	14.446	0.2611	0.1639	3.4087
RC	0.0737	14.814	0.2528	0.1449	4.152
LC	0.0582	13.409	0.2013	0.1382	4.2257
GT	0.1271	10.185	0.2093	0.1565	2.1891
GH	0.0616	10.52	0.2222	0.2022	2.6449
EL	0.0664	12.887	0.2167	0.1102	3.1848

APPENXID C. XRF DATA

C.1. XRF elemental concentrations for major elements in TP and sediment samples.

Sample Name	CaO (%)	MgO (%)	S (ppm)	Sr (ppm)
TP 1	49.7	1.45	592.1	5044.86
TP 2	52.81	1.54	564.12	5533.07
TP 3	53.19	1.49	576.6	5621.38
TP 4	51.6	1.5	702.11	4522.59
TP 5	52.09	1.53	621.83	4988.44
TP 6	51.42	1.34	802.6	6009.13
TP 7	52.36	1.38	666.76	6148.73
TP 8	50.66	1.38	710.96	5649.39
TP 9	48.98	1.48	606.29	4890.19
TP 10	49.94	1.44	705.1	4478.26
TP 11	50.38	1.54	712.28	3705.08
TP 12	51.64	1.53	839.09	3963.93
TP 13	48.21	1.62	1245.89	3740.06
PCFM1	38.05	6.87	5551.5	1464.6
PCFM 3 1/2	47.88	3.87	2712.1	4084.5
PCFM 3 2/2	48.46	3.93	2726.1	4124
PCM3A	44.63	3.91	3003.7	3438.9
PCM3	46.39	3.89	2696.7	3709.5
PCM4	48.62	3.83	2873.4	3847.2
PCBM	49.5	3.29	2937.6	3463.8
SCPO	-	-	-	-
SCOS	52.53	1.65	1615.8	7143.3
SCNO	-	-	-	-
SCNS	52.3	1.46	1724.5	7302.3
BO1	51.13	2.49	1610.8	5813.8
BD	51.46	2.07	2104.8	6419.5
PB	51.52	2.54	1748.5	5843.7
RC	51.33	2.36	1678.2	6061.1
LC	51.9	2.26	1632.5	5838.3
GT	51.4	2.5	1795	3880.5
GH	50.05	3.6	1757	3336.1
EL	50.43	3.18	1633.2	4933.6

APPENDIX D. INORGANIC $\delta^{13}C$ and $\delta^{18}O$ DATA

D.1. Inorganic $\delta^{13}C$ and $\delta^{18}O$ data for TP and sediment samples.

Sample Name	$\delta^{13}C$ (‰)	$\delta^{18}O$ (‰)
TP 1	2.62	-1.34
TP 2	2.61	-0.99
TP 3	2.62	-1.15
TP 4	0.16	-1.83
TP 5	2.29	-0.84
TP 6	0.64	-1.29
TP 7	0.79	-1.42
TP 8	0.29	-1.41
TP 9	0.96	-2.05
TP 10	1.00	-2.35
TP 11	-0.37	-2.71
TP 12	0.58	-2.68
TP 13	0.29	-2.71
PCFM1	1.13	0.81
PCFM 3 1/2	2.24	-0.1
PCFM 3 2/2	2.26	0.27
PCM3A	2.02	-0.05
PCM3	2.16	-0.51
PCM4	2.2	-0.08
PCBM	2.69	0.14
SCPO	4.82	-0.17
SCOS	4.7	-0.31
SCNO	4.59	-0.28
SCNS	4.7	0.14
BO1	4.33	-0.03
BD	3.79	-1.24
PB	3.9	-0.17
RC	3.71	-0.37
LC	4.02	-0.22
GT	1.28	-1.16
GH	2.84	-0.32
EL	3.47	-0.51

APPENDIX E. ORGANIC $\delta^{13}C$ and $\delta^{15}N$ DATA

E.1. Organic $\delta^{13}C$ and $\delta^{15}N$ data for modern sediment samples.

Sample Name	$\delta^{13}C$ (‰)	$\delta^{15}N$ (‰)
PCFM1	-23.2	0.34
PCFM 3 1/2	-22.3	1.19
PCFM 3 2/2	-21.5	1.64
PCM3A	-	-
PCM3	-17.1	0.95
PCM4	-17.1	1.55
PCBM	-20	1.1
SC Pure Ooid	-16.5	1.23
SCOS	-14.7	1.34
SC Non-Ooid	-15.9	1.99
SCNS	-16.1	1.76
BO1	-15.3	1.85
BD	-11.9	0.67
PB	-15.6	1.39
RC	-15.7	-0.23
LC	-20.9	4.17
GT	-16.6	2.17
GH	-15.1	2.85
EL	-16.9	2.58
PCBM-2	-16.5	1.81
PCM3-2	-17.1	0.95
PCM2	-16.6	1.81
PCFM3-1/2-2	-17.3	1.58
PCFM3-2/2-2	-17.5	1.54

APPENDIX F. $\delta^{34}S$ DATA FOR MODERN SEDIMENT SAMPLES

F.1. $\delta^{34}S$ values for modern sediment samples.

Sample Name	Run 1 $\delta^{34}S$ (‰)	Run 2 $\delta^{34}S$ (‰)	Run 3 $\delta^{34}S$ (‰)	Average $\delta^{34}S$
PCFM1	-30.2	-30.4	-30.2	-30.2608
PCFM 3 1/2	-24.0	-25.0	-22.6	-23.8644
PCFM 3 2/2	-22.7	-20.3	-23.4	-22.1196
PCM3A	-5.1	-4.8	-5.0	-4.94615
PCM3	-12.5	-12.0	-12.1	-12.1932
PCM4	-15.1	-14.4	-14.8	-14.7462
PCBM	-20.7	-20.6	-20.7	-20.6864
SCPO				
SCOS	7.6	7.6	7.6	7.61898
SCNO				
SCNS	6.5	10.4	10.9	9.24479
BO1	8.5	9.2	8.5	8.71064
BD	9.4	9.5	9.3	9.39099
PB	13.8	14.8	15.0	14.543
RC	-7.5	-2.8	-6.4	-5.54678
LC	3.7	4.3		3.99374
GT	-12.5	-14.0	-13.9	-13.4785
GH	-7.2	-8.9	-8.2	-8.11041
EL	10.4	10.7	10.6	10.5563

REFERENCES

Alibo, D.S., Nozaki, Y., 1999. Rare earth elements in seawater: particle association, shale-normalization, and Ce oxidation. Geochimica et Cosmochimica Acta, 63(3-4): 363-372.

Allan, J., Matthews, R., 1982. Isotope signatures associated with early meteoric diagenesis. Sedimentology, 29(6): 797-817.

Baars, C., Horak, J., 2018. Storage and conservation of geological collections—a research agenda. Journal of the Institute of Conservation, 41(2): 154-168.

Barker, J.F., Fritz, P., 1981. Carbon isotope fractionation during microbial methane oxidation. Nature, 293(5830): 289.

Bartlett, R., James, B., 1979. Behavior of chromium in soils: III. Oxidation 1. Journal of Environmental Quality, 8(1): 31-35.

Bau, M., 1999. Scavenging of dissolved yttrium and rare earths by precipitating iron oxyhydroxide: experimental evidence for Ce oxidation, Y-Ho fractionation, and lanthanide tetrad effect. Geochimica et Cosmochimica Acta, 63(1): 67-77.

Bau, M., Dulski, P., 1994. Evolution of the yttrium–holmium systematics of seawater through time. Mineral. Mag. A, 58: 61-62.

Bau, M., Koschinsky, A., 2009. Oxidative scavenging of cerium on hydrous Fe oxide: evidence from the distribution of rare earth elements and yttrium between Fe oxides and Mn oxides in hydrogenetic ferromanganese crusts. Geochemical Journal, 43(1): 37-47.

Bau, M., Koschinsky, A., Dulski, P., Hein, J.R., 1996. Comparison of the partitioning behaviours of yttrium, rare earth elements, and titanium between hydrogenetic marine ferromanganese crusts and seawater. Geochimica et Cosmochimica Acta, 60(10): 1709-1725.

Bau, M., Möller, P., Dulski, P., 1997. Yttrium and lanthanides in eastern Mediterranean seawater and their fractionation during redox-cycling. Marine Chemistry, 56(1-2): 123-131.

Ben-Yaakov, S., 1973. pH Buffering of pore water of recent anoxic marine sediments 1. Limnology and Oceanography, 18(1): 86-94.

Berner, R.A., 1970. Sedimentary pyrite formation. American journal of science, 268(1): 1-23.

Bouillon, S., Connolly, R., Lee, S., 2008. Organic matter exchange and cycling in mangrove ecosystems: recent insights from stable isotope studies. Journal of sea research, 59(1-2): 44-58.

Brunner, B., Bernasconi, S.M., 2005. A revised isotope fractionation model for dissimilatory sulfate reduction in sulfate reducing bacteria. Geochimica et Cosmochimica Acta, 69(20): 4759-4771.

Budd, D.A., Land, L.S., 1990. Geochemical imprint of meteoric diagenesis in Holocene ooid sands, Schooner Cays, Bahamas; correlation of calcite cement geochemistry with extant groundwaters. Journal of Sedimentary Research, 60(3): 361-378.

Byrne, R.H., Kim, K.-H., 1990. Rare earth element scavenging in seawater. Geochimica et Cosmochimica Acta, 54(10): 2645-2656.

Cantrell, K.J., Byrne, R.H., 1987. Rare earth element complexation by carbonate and oxalate ions. Geochimica et Cosmochimica Acta, 51(3): 597-605.

Carew, J.L., Mylroie, J.E., 1995. Quaternary tectonic stability of the Bahamian Archipelago: Evidence from fossil coral reefs and flank margin caves. Quaternary Science Reviews, 14(2): 145-153.

Cavalazzi, B., Agangi, A., Barbieri, R., Franchi, F., Gasparotto, G., 2014. The formation of low-temperature sedimentary pyrite and its relationship with biologically-induced processes. Geology of Ore Deposits, 56(5): 395-408.

Cerling, T.E., Solomon, D.K., Quade, J., Bowman, J.R., 1991. On the isotopic composition of carbon in soil carbon dioxide. Geochimica et Cosmochimica Acta, 55(11): 3403-3405.

Chave, K., Deffeyes, K., Weyl, P., Garrels, R., Thompson, M., 1962. Observations on the solubility of skeletal carbonates in aqueous solutions. Science, 137(3523): 33-34.

Chen, X. et al., 2018. Diagenetic effects on uranium isotope fractionation in carbonate sediments from the Bahamas. Geochimica et Cosmochimica Acta, 237: 294-311.

Conrad Neumann, A., Hearty, P.J., 1996. Rapid sea-level changes at the close of the last interglacial (substage 5e) recorded in Bahamian island geology. Geology, 24(9): 775-778.

Craine, J.M. et al., 2015. Ecological interpretations of nitrogen isotope ratios of terrestrial plants and soils. Plant and Soil, 396(1-2): 1-26.

De Baar, H.J., Brewer, P.G., Bacon, M.P., 1985. Anomalies in rare earth distributions in seawater: Gd and Tb. Geochimica et Cosmochimica Acta, 49(9): 1961-1969.

Detmers, J., Brüchert, V., Habicht, K.S., Kuever, J., 2001. Diversity of sulfur isotope fractionations by sulfate-reducing prokaryotes. Appl. Environ. Microbiol., 67(2): 888-894.

Drake, H. et al., 2015. Extreme 13 C depletion of carbonates formed during oxidation of biogenic methane in fractured granite. Nature communications, 6: 7020.

Du Laing, G. et al., 2008. Metal accumulation in intertidal marshes: role of sulphide precipitation. Wetlands, 28(3): 735-746.

Elderfield, H., 1988. The oceanic chemistry of the rare-earth elements. Philosophical Transactions of the Royal Society of London. Series A, Mathematical and Physical Sciences, 325(1583): 105-126.

Fichtner, V. et al., 2017. Diagenesis of carbonate associated sulfate. Chemical Geology, 463: 61-75.

Fike, D., Grotzinger, J., Pratt, L., Summons, R., 2006. Oxidation of the Ediacaran ocean. nature, 444(7120): 744.

Gill, B.C., Lyons, T.W., Frank, T.D., 2008. Behavior of carbonate-associated sulfate during meteoric diagenesis and implications for the sulfur isotope paleoproxy. Geochimica et Cosmochimica Acta, 72(19): 4699-4711.

Habicht, K.S., Canfield, D.E., 1997. Sulfur isotope fractionation during bacterial sulfate reduction in organic-rich sediments. Geochimica et Cosmochimica Acta, 61(24): 5351-5361.

Hardisty, D.S. et al., 2017. Perspectives on Proterozoic surface ocean redox from iodine contents in ancient and recent carbonate. Earth and Planetary Science Letters, 463: 159-170.

Hearty, P.J., 1998. The geology of Eleuthera Island, Bahamas: a Rosetta Stone of Quaternary stratigraphy and sea-level history. Quaternary Science Reviews, 17(4-5): 333-355.

Hearty, P.J., Kaufman, D.S., 2000. Whole-rock aminostratigraphy and Quaternary sea-level history of the Bahamas. Quaternary Research, 54(2): 163-173.

Hearty, P.J., Kindler, P., 1993. New perspectives on Bahamian geology: San Salvador Island, Bahamas. Journal of Coastal Research: 577-594.

Hearty, P.J., Kindler, P., 1995. Sea-level highstand chronology from stable carbonate platforms (Bermuda and the Bahamas). Journal of Coastal Research: 675-689.

Hearty, P.J., Neumann, A.C., 2001. Rapid sea level and climate change at the close of the Last Interglaciation (MIS 5e): evidence from the Bahama Islands. Quaternary Science Reviews, 20(18): 1881-1895.

Hecht, H., Kölling, M., 2002. Investigation of pyrite-weathering processes in the vadose zone using optical oxygen sensors. Environmental geology, 42(7): 800-809.

Higgins, J., Fischer, W., Schrag, D., 2009. Oxygenation of the ocean and sediments: consequences for the seafloor carbonate factory. Earth and Planetary Science Letters, 284(1-2): 25-33.

Holland, S., Patzkowsky, M., 1998. Sequence stratigraphy and relative sea-level history of the Middle and Upper Ordovician of the Nashville Dome, Tennessee. Journal of Sedimentary Research, 68(4): 684-699.

Howie, F.M., 1979. Museum climatology and the conservation of palaeontological material. Curation of palaeontological collections(22): 103-127.

Husseini, S., Matthews, R., 1972. Distribution of high-magnesium calcite in lime muds of the Great Bahama Bank; diagenetic implications. Journal of Sedimentary Research, 42(1): 179-182.

Jarvis, K.E., Gray, A.L., McCurdy, E., 1989. Avoidance of spectral interference on europium in inductively coupled plasma mass spectrometry by sensitive measurement of the doubly charged ion. Journal of Analytical Atomic Spectrometry, 4(8): 743-747.

Jian, L., Zhizheng, Y., Chunrui, H., Xinbo, L., Gaosheng, Q., 1997. Meteoric diagenesis in Pleistocene reef limestones of Xisha Islands, China. Journal of Asian Earth Sciences, 15(6): 465-476.

Johnson, D.B., Hallberg, K.B., 2005. Acid mine drainage remediation options: a review. Science of the total environment, 338(1-2): 3-14.

Jupiter, S., 2008. Coral rare earth element tracers of terrestrial exposure in nearshore corals of the Great Barrier Reef, Proceedings of the 11th International Coral Reef Symposium, Ft. Lauderdale, Florida, Session, pp. 105-109.

Kindler, P., Hearty, P.J., 1996. Carbonate petrography as an indicator of climate and sea-level changes: new data from Bahamian Quaternary units. Sedimentology, 43(2): 381-399.

Kindler, P., Strasser, A., Neumann, A.C., Hearty, P.J., 1997. Rapid sea-level changes at the close of the last interglacial (substage 5e) recorded in Bahamian island geology: Comment and Reply. Geology, 25(12): 1147-1149.

Kraal, P., Burton, E.D., Bush, R.T., 2013. Iron monosulfide accumulation and pyrite formation in eutrophic estuarine sediments. Geochimica et Cosmochimica Acta, 122: 75-88.

Land, L.S., 1967. Diagenesis of skeletal carbonates. Journal of Sedimentary Research, 37(3): 914-930.

Lawrence, M.G., Greig, A., Collerson, K.D., Kamber, B.S., 2006. Rare earth element and yttrium variability in South East Queensland waterways. Aquatic Geochemistry, 12(1): 39-72.

Lehmann, M.F., Bernasconi, S.M., Barbieri, A., McKenzie, J.A., 2002. Preservation of organic matter and alteration of its carbon and nitrogen isotope composition during simulated and in situ early sedimentary diagenesis. Geochimica et Cosmochimica Acta, 66(20): 3573-3584.

Li, R., Jones, B., 2014. Evaluation of carbonate diagenesis: A comparative study of minor elements, trace elements, and rare-earth elements (REE+ Y) between Pleistocene corals and matrices from Grand Cayman, British West Indies. Sedimentary geology, 314: 31-46.

Li, R. et al., 2018. Composition and diagenesis of Pleistocene aeolianites at Shidao, Xisha Islands: Implications for palaeoceanography and palaeoclimate during the last glacial period. Palaeogeography, Palaeoclimatology, Palaeoecology, 490: 604-616.

Liu, X.-M., Hardisty, D.S., Lyons, T.W., Swart, P.K., 2019. Evaluating the fidelity of the cerium paleoredox tracer during variable carbonate diagenesis on the Great Bahamas Bank. Geochimica et Cosmochimica Acta, 248: 25-42.

Luo, Y.-R., Byrne, R.H., 2004. Carbonate complexation of yttrium and the rare earth elements in natural waters. Geochimica et Cosmochimica Acta, 68(4): 691-699.

Matthews, R., 1968. Carbonate diagenesis; equilibration of sedimentary mineralogy to the subaerial environment; coral cap of Barbados, West Indies. Journal of Sedimentary Research, 38(4): 1110-1119.

Matthews, R., 1974. A process approach to diagenesis of reefs and reef associated limestones.

Melim, L.A., Swart, P.K., Maliva, R.G., 1995. Meteoric-like fabrics forming in marine waters: Implications for the use of petrography to identify diagenetic environments. Geology, 23(8): 755-758.

Melim, L.A., Swart, P.K., Maliva, R.G., 2001. Meteoric and marine-burial diagenesis in the subsurface of Great Bahama Bank.

Moore, T.S., Murray, R., Kurtz, A., Schrag, D., 2004. Anaerobic methane oxidation and the formation of dolomite. Earth and Planetary Science Letters, 229(1-2): 141-154.

Morse, J.W., 1999. Sulfides in sandy sediments: new insights on the reactions responsible for sedimentary pyrite formation. Aquatic Geochemistry, 5(1): 75-85.

Muecke, G.K., Möller, P., 1988. The not-so-rare earths. Scientific American, 258(1): 72-77.

Muhs, D.R., Budahn, J.R., Prospero, J.M., Carey, S.N., 2007. Geochemical evidence for African dust inputs to soils of western Atlantic islands: Barbados, the Bahamas, and Florida. Journal of Geophysical Research: Earth Surface, 112(F2).

Nozaki, Y., 1997. A fresh look at element distribution in the North Pacific Ocean. EOS Trans., American Geophysical Union, 78: 221.

Nozaki, Y., Zhang, J., 1995. The rare earth elements and yttrium in the coastal/offshore mixing zone of Tokyo Bay waters and the Kuroshio. Biogeochemical processes and ocean flux in the Western Pacific: 171-184.

O'Leary, M.H., 1988. Carbon isotopes in photosynthesis. Bioscience, 38(5): 328-336.

Oehlert, A.M. et al., 2012. The stable carbon isotopic composition of organic material in platform derived sediments: implications for reconstructing the global carbon cycle. Sedimentology, 59(1): 319-335.

Olivier, N., Boyet, M., 2006. Rare earth and trace elements of microbialites in Upper Jurassic coral-and sponge-microbialite reefs. Chemical Geology, 230(1-2): 105-123.

Oze, C., Bird, D.K., Fendorf, S., 2007. Genesis of hexavalent chromium from natural sources in soil and groundwater. Proceedings of the National Academy of Sciences, 104(16): 6544-6549.

Palmer, M., 1985. Rare earth elements in foraminifera tests. Earth and planetary science letters, 73(2-4): 285-298.

Pingitore Jr, N.E., Meitzner, G., Love, K.M., 1995. Identification of sulfate in natural carbonates by X-ray absorption spectroscopy. Geochimica et Cosmochimica Acta, 59(12): 2477-2483.

Pingitore, N., 1976. Vadose and phreatic diagenesis; processes, products and their recognition in corals. Journal of Sedimentary Research, 46(4): 985-1006.

Pingitore, N., 1978. The behavior of Zn 2+ and Mn 2+ during carbonate diagenesis; theory and applications. Journal of Sedimentary Research, 48(3): 799-814.

Pingitore, N.E., 1982. The role of diffusion during carbonate diagenesis. Journal of Sedimentary Research, 52(1): 27-39.

Pourmand, A., Dauphas, N., Ireland, T.J., 2012. A novel extraction chromatography and MC-ICP-MS technique for rapid analysis of REE, Sc and Y: Revising CI-chondrite and Post-Archean Australian Shale (PAAS) abundances. Chemical Geology, 291: 38-54.

Railsback, L.B. et al., 2003. Controls on geochemical expression of subaerial exposure in Ordovician limestones from the Nashville Dome, Tennessee, USA. Journal of Sedimentary Research, 73(5): 790-805.

Railsback, L.B. et al., 2013. Geochemical evidence for meteoric diagenesis and cryptic surfaces of subaerial exposure in Upper Ordovician peritidal carbonates from the Nashville Dome, central Tennessee, USA. Linking Diagenesis to Sequence Stratigraphy: 257-269.

Rankey, E.C., Reeder, S.L., 2011. Holocene oolitic marine sand complexes of the Bahamas. Journal of Sedimentary Research, 81(2): 97-117.

Raven, M.R., Sessions, A.L., Adkins, J.F., Thunell, R.C., 2016. Rapid organic matter sulfurization in sinking particles from the Cariaco Basin water column. Geochimica et Cosmochimica Acta, 190: 175-190.

Reeder, R.J., Nugent, M., Lamble, G.M., Tait, C.D., Morris, D.E., 2000. Uranyl incorporation into calcite and aragonite: XAFS and luminescence studies. Environmental Science & Technology, 34(4): 638-644.

Rickard, D., Morse, J.W., 2005. Acid volatile sulfide (AVS). Marine chemistry, 97(3-4): 141-197.

Rietveld, H., 1969. A profile refinement method for nuclear and magnetic structures. Journal of applied Crystallography, 2(2): 65-71.

Rimstidt, J.D., Balog, A., Webb, J., 1998. Distribution of trace elements between carbonate minerals and aqueous solutions. Geochimica et Cosmochimica Acta, 62(11): 1851-1863.

Romaniello, S.J., Herrmann, A.D., Anbar, A.D., 2013. Uranium concentrations and 238U/235U isotope ratios in modern carbonates from the Bahamas: Assessing a novel paleoredox proxy. Chemical Geology, 362: 305-316.

Romaniello, S.J., Herrmann, A.D., Anbar, A.D., 2016. Syndepositional diagenetic control of molybdenum isotope variations in carbonate sediments from the Bahamas. Chemical Geology, 438: 84-90.

Schrag, D.P., Higgins, J.A., Macdonald, F.A., Johnston, D.T., 2013. Authigenic carbonate and the history of the global carbon cycle. science, 339(6119): 540-543.

Schroeder, J.H., 1969. Experimental dissolution of calcium, magnesium, and strontium from recent biogenic carbonates: a model of diagenesis. Journal of Sedimentary Research, 39(3).

Staudt, W.J., Schoonen, M.A., 1995. Sulfate incorporation into sedimentary carbonates, ACS Symposium Series. Washington, DC: American Chemical Society,[1974]-, pp. 332-347.

Swart, P., 2017. Aramco field guide Eleuthera. Miami.

Swart, P.K., Oehlert, A., Mackenzie, G., Eberli, G.P., Reijmer, J., 2014. The fertilization of the Bahamas by Saharan dust: A trigger for carbonate precipitation? Geology, 42(8): 671-674.

Swart, P.K., Oehlert, A.M., 2018. Revised interpretations of stable C and O patterns in carbonate rocks resulting from meteoric diagenesis. Sedimentary Geology, 364: 14-23.

Swart, P.K., Reijmer, J., Otto, R., 2009. A reevaluation of facies on Great Bahama Bank II: Variations in the δ13C, δ18O and mineralogy of surface sediments. Perspectives in carbonate geology: A tribute to the career of Robert Nathan Ginsburg, 41: 47-59.

Tostevin, R. et al., 2016. Effective use of cerium anomalies as a redox proxy in carbonate-dominated marine settings. Chemical Geology, 438: 146-162.

Van Wagoner, J.C., Mitchum, R., Campion, K., Rahmanian, V., 1990. Siliciclastic sequence stratigraphy in well logs, cores, and outcrops: concepts for high-resolution correlation of time and facies.

Webb, G.E., Kamber, B.S., 2000. Rare earth elements in Holocene reefal microbialites: a new shallow seawater proxy. Geochimica et Cosmochimica Acta, 64(9): 1557-1565.

Webb, G.E., Nothdurft, L.D., Kamber, B.S., Kloprogge, J., ZHAO, J.X., 2009. Rare earth element geochemistry of scleractinian coral skeleton during meteoric diagenesis: a sequence through neomorphism of aragonite to calcite. Sedimentology, 56(5): 1433-1463.

Zhong, S., Mucci, A., 1995. Partitioning of rare earth elements (REEs) between calcite and seawater solutions at 25 C and 1 atm, and high dissolved REE concentrations. Geochimica et Cosmochimica Acta, 59(3): 443-453.

VITA

Evan Magette was born and raised in Baton Rouge, Louisiana. He attended Baton Rouge Magnet High School before moving on to attending Louisiana State University to obtain his bachelor's degree in geology. He plans on finishing his master's degree through the accelerated master's degree program at Louisiana State University in May 2019. Afterwards, he plans on perusing a PhD with a focus on geochemistry.